5-2018

The Synthesis and Characterization of New Triangular Lattice Compounds with Exotic Magnetic Ground States

Ryan Patrick Sinclair
University of Tennessee, rsincla2@vols.utk.edu

To the Graduate Council:

I am submitting herewith a dissertation written by Ryan Patrick Sinclair entitled "The Synthesis and Characterization of New Triangular Lattice Compounds with Exotic Magnetic Ground States." I have examined the final electronic copy of this dissertation for form and content and recommend that it be accepted in partial fulfillment of the requirements for the degree of Doctor of Philosophy, with a major in Physics.

Haidong Zhou, Major Professor

We have read this dissertation and recommend its acceptance:

Christian D. Batista, Jian Liu, David G. Mandrus

Accepted for the Council:

Dixie L. Thompson

Vice Provost and Dean of the Graduate School

(Original signatures are on file with official student records.)

The Synthesis and Characterization of New Triangular Lattice Compounds with Exotic Magnetic Ground States

A Dissertation Presented for the

Doctor of Philosophy

Degree

The University of Tennessee, Knoxville

Ryan Patrick Sinclair

May 2018

This dissertation is dedicated to my wife MaryEllen and my daughter Arabella.

Acknowledgments

First, I would like to thank my advisor Prof. Haidong Zhou for his constant guidance over the entire course of my graduate education. He has helped me develop into a much stronger physicist, one now capable of undertaking scientific endeavors alone. He has also been instrumental in strengthening my professional writing skills which has lead to several publications in various journals of repute.

None of my work would have been possible without several important collaborators. I would first like to thank the local staff and scientists of the National Laboratories where I performed several experiments. In particular, I would like to thank Minseong Lee and Eun San Choi from Maglab, Huibo Cao, Stuart Calder, and Tao Hong from Oak Ridge National Laboratory, and Jeffrey Quilliam from the University of Sherbrooke. Without their help, none of this work would have succeeded.

I would also like to thank Prof. Jian Liu, Prof. David Mandrus, and Prof. Cristian Batista for serving on my doctoral committee.

Abstract

The foundation of experimental condensed matter physics is comprised of two material processes, synthesis and characterization. For most measurements, single crystal samples are preferred as they allow spatially dependent information to be obtained. On the other hand, polycrystalline samples are also critical as they reveal bulk properties of the material and are generally much easier to produce. Material characterization then relies on accurately measuring a material's physical, electrical, and magnetic properties using a variety of different techniques.

In this dissertation, we focus on triangular lattice antiferromagnets (TLAFs) which have been studied because of their great potential to exhibit various intriguing magnetic properties related to strong geometrical frustration. Recent studies of TLAFs mainly explore four central themes: quantum spin liquid (QSL) states, exotic disordered states, the coplanar 120 degree state and the related field induced spin state transitions, and multiferroicity. Accordingly, we have investigated two materials which fall into these categories. The first is the magnetodielectric material $R\mathrm{Cr}(\mathrm{BO}_3)_2$ (R = Y and Ho), and the second is a group of Mo-cluster compounds including the quantum spin liquid candidate $\mathrm{Li}_2\mathrm{In}_{1-x}\mathrm{Sc}_x\mathrm{Mo}_3\mathrm{O}_8$ and the ferromagnets (Mg,Zn)$\mathrm{ScMo}_3\mathrm{O}_8$. Both materials have been investigated using x-ray diffraction, powder neutron diffraction, ac and dc susceptibility, and specific heat capacity measurements as well as other complementary techniques. A discussion of these results as well as potential future experiments are included.

Table of Contents

List of Tables

List of Figures

List of Abbreviations

TLAF ..... Triangular lattice antiferromagnet

QSL ..... Quantum spin liquid

AFM ..... Antiferromagnet/Antiferromagnetic(ally)

NN ..... Nearest neighbor

FM ..... Ferromagnet/Ferromagnetic(ally)

LRO ..... Long-range order

RVB ..... Resonating valence bond

1D ..... One-dimensional

2D ..... Two-dimensional

3D ..... Three-dimensional

NMR ..... Nuclear magnetic resonance

μSR ..... Muon spin rotation

DM ..... Dzyaloshinsky-Moriya

ZFC ..... Zero field cooling

FC ..... Field cooling

ESR ..... Electron spin resonance

INS ..... Inelastic neutron scattering

XRD ..... X-ray diffraction

ENS ..... Elastic neutron scattering

NQR ..... Nuclear quadrupole resonance

BKT ..... Berezinskii-Kosterlitz-Thouless

TLHAF ..... Triangular lattice Heisenberg antiferromagnet

uud ..... up-up-down

NPD ..... Neutron powder diffraction

DFT ..... Density functional theory

PPMS ..... Physical Property Measurement System

PM ..... Paramagnet/Paramagnetic(ally)

MPMS ..... Magnetic Property Measurement System

SQUID ..... Superconducting interference device

CW ..... Curie-Weiss

VSM ..... Vibrating Sample Magnetometer

NHMFL ..... National High Magnetic Field Laboratory

HFIR ..... High Flux Isotope Reactor

ORNL ..... Oak Ridge National Laboratory

CTAX ..... Cold Neutron Triple-Axis Spectrometer

ME ..... Magnetoelectric

NNN ..... Next nearest neighbor

MD ..... Magnetodielectric

PCO ..... Plaquette charge order

BKL ..... Breathing Kagome lattice

Mott-VRH ... Mott's variable range hopping

CMI ..... Cluster Mott insulator

Chapter 1

Introduction

This chapter is intended to give a brief introduction to triangular lattice compounds, primarily focusing on triangular lattice antiferromagnets (TLAFs). I begin with a brief introduction to geometrical frustration, which is strongly related to many of the intriguing magnetic properties of TLAFs, focusing on its influence on the quantum spin liquid (QSL) state. Next, I provide a brief example of the four central themes that are the focus of most TLAF studies: QSL states, exotic disordered states, the coplanar 120 degree state and the related field induced spin state transitions, and multiferroicity. Finally, I present a short explanation as to why the synthesis and characterization of new materials is a necessary driving force behind condensed matter physics.

1.1 Introduction to Frustration and Quantum Spin Liquid States

In physics, a system is frustrated if there exist competing forces which cannot be simultaneously satisfied. Thus, frustrated magnetism implies that a system's localized magnetic moments are interacting via competing exchange interactions that cannot be satisfied at the same time. Such phenomena creates a large degeneracy in the system's ground state.[1] In particular, antiferromagnetic (AFM) interactions can lead to frustration on certain lattices as it is impossible for all nearest neighbor (NN) magnetic moments to

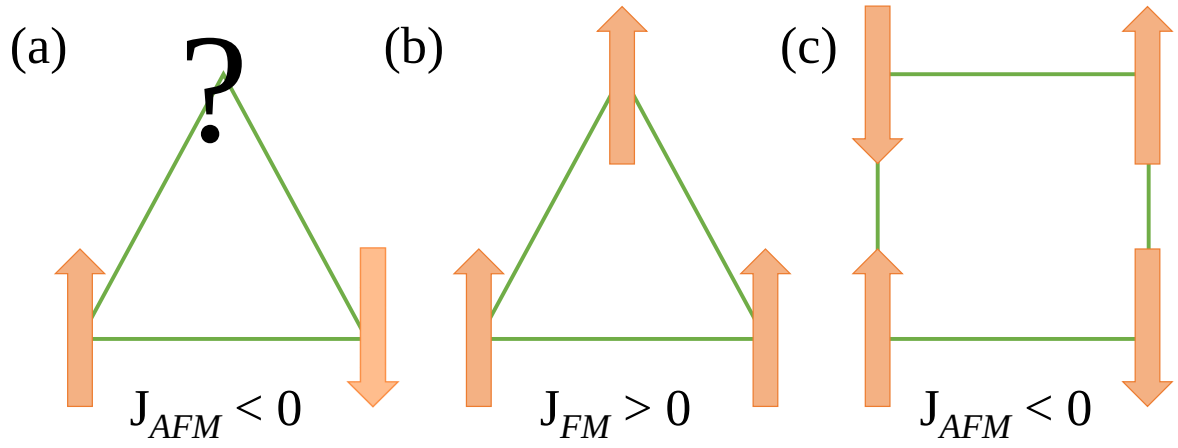

Figure 1.1: Ising models for (a) a triangle with AFM magnetic moments, (b) a triangle with FM magnetic moments, and (c) a square with NN AFM magnetic moments.

align anti-parallel. As illustrated in Fig. 1.1(a), a triangle of AFM interacting Ising spins–spins that must point either up or down–is the simplest example of frustration. Two of the spins pair up and align antiparallel which causes the third spin to be frustrated as the same total energy is achieved with either the up or the down spin configuration. If the triangle is composed of ferromagnetically (FM) interacting Ising spins, the frustration is lifted because there is now a unique ground state as shown in Fig. 1.1(b); moreover, the frustration also disappears if the same AFM Ising spin configuration is applied to a square lattice as shown in Fig. 1.1(c). This simple example highlights two key aspects of frustrated magnetism: many-body interactions and the lattice geometry.

Geometric frustration refers to frustration that specifically arises due to the lattice structure, as opposed to distinct competing interactions, preventing all spins from aligning to form a unique ground state. To study this behavior, one must start with the idea of classical ground state degeneracy which is considered to be a defining characteristic of frustration. In 1950, Wannier demonstrated that a two-dimensional triangular lattice AFM has an enormous number of ground states.[2] The extensive ground-state entropy was calculated as 0.323 k_BN, where k_B is the Boltzmann constant and N is the number of spins. As the temperature is decreased, the spins will fluctuate thermally in a correlated manner. What will happen if we apply this idea to a Kagome lattice AFM where the ground state is known to be a degenerate Kagome spin ice? For such a state, classical fluctuations such as thermal

activation dominate. Excitations of any form will require a minimum energy related to the Ising nature of the spin in order to flip the orientation of the magnetic moment. When the temperature becomes sufficiently low, the system will fall out of equilibrium and freeze into one particular microstate. Consequently, such a system can be thought of as a classical spin liquid, or cooperative paramagnet, which is analogous to an ordinary liquid–a dense, highly correlated state with no static order.[1]

When a frustrated magnet with a magnetic moment comparable to a spin 1/2 system is introduced to quantum spin fluctuations, zero-point motions comparable to the size of the magnetic moment are produced by the quantum mechanical uncertainty principle which persist down to absolute zero temperature. Quantum spin fluctuations can be phase coherent, differentiating them from thermal fluctuations. If the quantum spin fluctuations are strong enough, the result is a superposition state in which the spins are simultaneously pointing in different directions.[1] Such a state is known as a quantum spin liquid (QSL). The first study pertaining to QSLs was conducted by P. W. Anderson in 1987.[3] In this manuscript, Anderson proposed that nearby spins can form pairs of rotationally invariant singlets, or valence bonds, which never develop long-range order (LRO) at any temperature regardless of the local environment. This state was known as a resonating valence bond (RVB). In order to achieve a RVB ground state, different single configurations must produce large-scale resonances which create a sizable energy gain through interference effects. Thus the ground state is a superposition of various valence bonds corresponding to different spin partitions. This idea is illustrated in Fig. 1.2.

Inspired by Anderson, further studies on RVBs revealed the valence bonds can be formed from pairs separated by much larger distances than initially proposed.[4]. In fact, valence bonds formed from spins that are farther apart are less tightly bound and are therefore more easily excited into non-zero spin states. This behavior allows for the possibility of great numbers of unique QSL states. As a result, the need to classify different QSL states arose. For square lattice $S = 1/2$ AFMs, hundreds of QSLs have been classified using the concept of projective symmetry groups,[5] but there remains much more work to be done in this area. Finally, it should be pointed out that most QSL states are expected to possess a definite topological order for both their ground state and their collective excitations, as

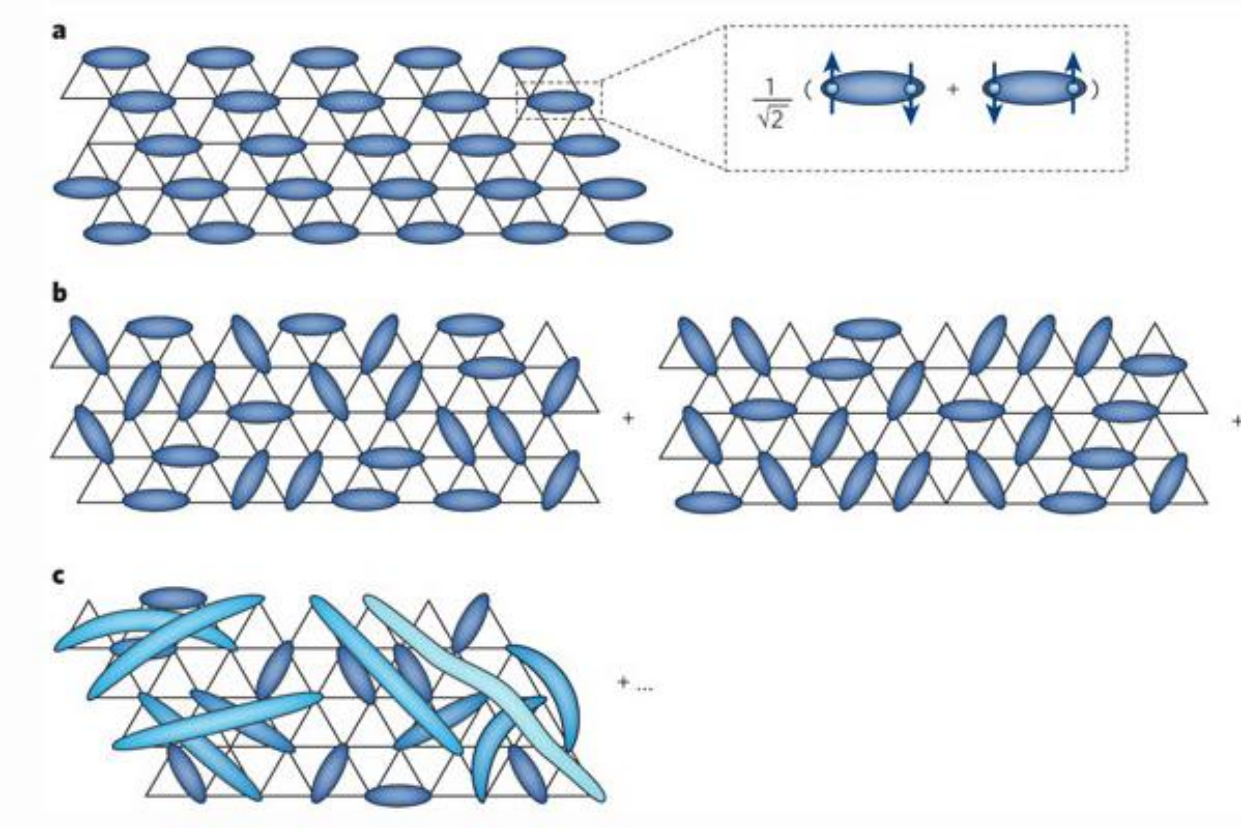

Figure 1.2: a) A ground state configuration of singlet states (valence bonds). b) Ground state made up of a superposition of many configurations of singlets. c) Longer range valence bonds that are more easily excited into non-zero spin states. This figure was taken directly from Ref. 1.

opposed to disordered states. Such behavior is similar to superconductors and quantum spin Hall liquids.[6]

If we want to define a QSL state in terms of excitations, then a QSL is a state with fractional quasi-particle excitations. In classical phases of matter, excitations are composed of elementary excitations that are either magnon-like (charge neutral with $S = 1$) or electron-like (charge $\pm e$ with $S = 1/2$). In contrast, QSL excitations are usually composed of exotic, charge neutral quasi-particles carrying half-integer spins known as spinons. As the excitations are fractional, the spinons can be deconfined–placed far apart with a finite energy cost.[7] Thus, a spinon can be thought of as a fraction of an electron. In one-dimensional (1D) systems, it is well established that spinons occur as domain walls,[8] whereas in two-dimensional (2D) and three-dimensional (3D) systems, a spinon is formed as an unpaired spin which is able to move by locally manipulating the valence bonds.

Experimentally, frustration is measured quantitatively by the frustration index, $f \equiv \theta_{CW}/T_c$.[9] Here, θ_{CW} is the Curie temperature which characterizes the sign and strength of the interaction and T_c is the ordering, or spin freezing, temperature. Frustrated materials have a high frustration index as the paramagnetic region usually extends to temperatures well below the ordering temperature. The Curie temperature associated with the absence of static moments can be probed by magnetic susceptibility and specific heat measurements as well as by nuclear magnetic resonance (NMR) and muon spin rotation (μSR) experiments. Furthermore, magnetic neutron scattering which probes the dynamical structure factor $S(\mathbf{Q}, \omega)$ provides even more detailed information regarding the correlations and excitiations in the system. Combining these techniques yields the information necessary to fully study magnetic frustration.

1.2 Triangular Lattice Compounds

For many years, triangular lattice compounds have been studied because of their great potential to exhibit various intriguing magnetic properties related to strong geometrical frustration.[1, 9, 10] While the QSL state was previously addressed in relation to frustration, geometrical frustration can also lead to many other exotic ground states, such as spin

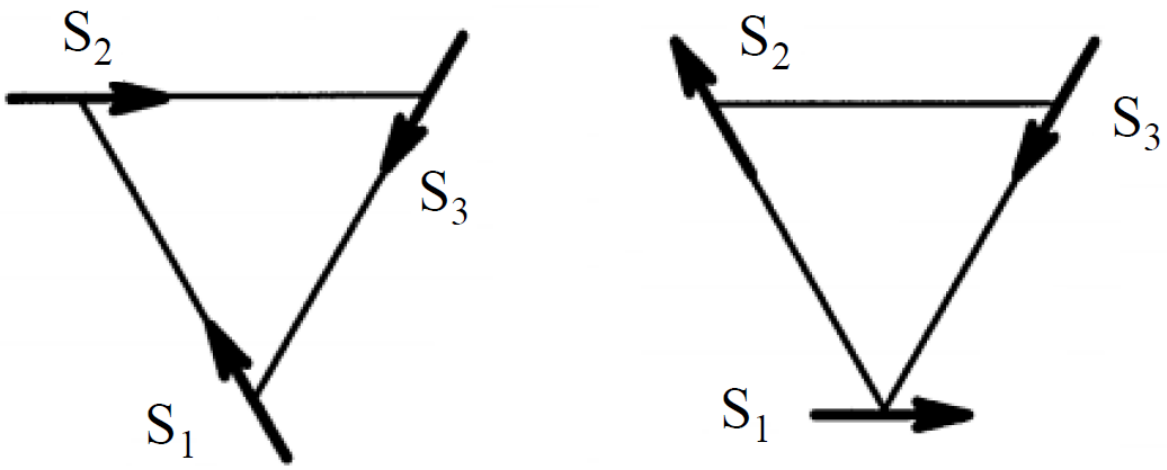

Figure 1.3: Two energetically equivalent ground states for the 2D TLAF unit cell with easy plane anisotropy.

ice and spin glass states.[1] One particularly well-studied structure which is susceptible to geometrical frustration is the 2D triangular lattice antiferromagnet (TLAF).[11, 12, 13] When considering NN interactions, the 2D TLAF is fully frustrated, and it is also relatively simple to model numerically. If a 2D TLAF has moments confined to the 2D plane (easy plane anisotropy), then the ground state is composed of degenerate 120 degree arrangements as shown in Fig. 1.3. Instead, if easy axis anisotropy is introduced, the moments will contain a z-axis component and will form a 120 degree configuration in a plane which includes the c direction. For both types of anisotropy, frustration will produce rich phase diagrams.[10] In particular, the easy axis anisotropy produces a quantum mechanical up-up-down state which can be seen as a magnetization plateau, a feature not associated with purely classical interactions.[10] While 2D TLAFs exhibit many fascinating properties, expanding the field beyond 2D TLAFs has uncovered a veritable treasure trove of interesting physical phenomena. Recently, studies of TLAFs mainly focus on four central themes: QSL states, exotic disordered states, the coplanar 120 degree state and the related field induced spin state transitions, and multiferroicity. One example of each theme is discussed below.

1.2.1 Quantum Spin Liquid States

TLAFs with S =1/2 provide an ideal setting for QSL states, and there are currently several QSL candidates among TLAFs.[3, 14, 15, 16, 17] One promising example is the TLAF $YbMgGaO_4$. This material belongs to the type $Ln^{3+}M^{2+}M'^{3+}O_4$ where Ln is Yb or Lu and M and M' are both late $3d$ transition metals.[18] The Yb or Lu atoms are octahedrally coordinated with the O atoms. Furthermore, the octahedra form a triangular layer while the transition metals form disordered triangular double layers as shown in Fig. 1.4(a). Consequently, these compounds are both geometrically and site-disorder frustrated with two triangular magnetic sublattices.[18] $YbMgGaO_4$ exploits this geometry to separate the planes of magnetic Yb^{3+} atoms using the double layers of nonmagnetic Mg/Ga atoms which leads to negligible interlayer exchange interactions and 2D triangular magnetic layers.

Polycrystalline $YbMgGaO_4$ was synthesized and found to be an effective spin-1/2 system with $R\bar{3}m$ symmetry and perfect, spatially isotropic triangular layers.[19] As a result, inversion centers are located at all Yb^{3+} ions and at the halfway sites between them which excludes any antisymmetric Dzyaloshinsky-Moriya (DM) interactions between the first, second, and third NN spins.[20] The large chemical difference between the magnetic Yb^{3+} Kramer's ions and the nonmagnetic Mg/Ga ions also greatly reduces the number of magnetic defects. Analysis of the magnetic susceptibility suggested an AFM NN exchange interaction which was further corroborated by a negative Curie temperature θ_{CW} = -4.11(2) K; however, the measured zero field cooling (ZFC) and field cooling (FC) susceptibilities as well as the heat capacity showed no features associated with a long-range ferromagnetic (FM) or AFM or a short-range spin glass or spin ice transition down to 60 mK.[19] Below 2 K, the magnetic heat capacity follows a power-law temperature dependence with $\gamma \sim 0.7$, approaching the theoretical value of $\gamma = 2/3$ for U(1) QSLs,[21] and the tiny residual spin entropy further corroborate the existence of a possibly gapless QSL state.[19]

More recent studies on single crystal samples have shed more light upon the system's ground state. The effective spin-1/2 nature of the Yb^{3+} moments at low temperature was confirmed via specific heat and magnetic entropy measurements, and anisotropic spin exchange interactions on the triangular Yb^{3+} lattice were confirmed using electron

spin resonance (ESR) measurements.[22] A possible U(1) QSL regime was discovered via μSR measurements, and a phase diagram based on these measurements combined with the bulk susceptibility was constructed as shown in Fig. 1.4(b).[23] Inelastic neutron scattering (INS) experiments further suggest a possible low temperature spinon-fermi-surface U(1) QSL regime highly correlated with the NN spin interactions and the Mg/Ga disorder.[24, 25, 26, 27] On the other hand, while ultralow-temperature specific heat measurements suggested gapless magnetic excitations, the thermal conductivity revealed no significant magnetic contribution at zero field.[28]

A standard XXZ Hamiltonian[22] modeling $YbMgGaO_4$ reveals two distinct phases illustrated in Fig. 1.4(c): a 120 degree phase with three sublattices and two stripe phases.[29] Adding pseudodipolar terms which tend to align the direction of the spins on a bond either parallel or perpendicular to the bond itself to the XXZ model provides a more robust phase diagram. As shown in Fig. 1.4(d), the system now includes a 120 degree phase, a strip phase, and spin liquid phases; however, this model actually predicts that the system's ground state is not a QSL but rather generates a mimicry of a QSL state in the form of short-range stripe-superposition domains.[30] If the system is modeled instead using the spinon mean-field Hamiltonian for a U(1) QSL, a model consistent with the low temperature specific heat capacity measurements, the ground state is found to be a spinon-fermi-surface U(1) QSL, and the numerical results are consistent with the experimental INS results.[22] Clearly, there is still much work to do in order to identify the exact ground state of this system.

1.2.2 Exotic Disordered States

$NiGa_2S_4$ is an excellent example of a compound which exhibits an exotic disordered ground state. First reported in 2005, $NiGa_2S_4$ contains a stacked triangular lattice of magnetic Ni^{2+} ions with $S = 1$.[31] Polycrystalline samples were initially characterized using powder x-ray diffraction (XRD), magnetic susceptibility, specific heat, and elastic neutron scattering (ENS) measurements which revealed several unique low temperature properties of the system including the existence of an incommensurate short-range order with nanoscale correlations, a complete lack of canonical bulk spin glass freezing, 2D gapless coherent excitations which are sensitive to impurities but not to field, and low-energy states

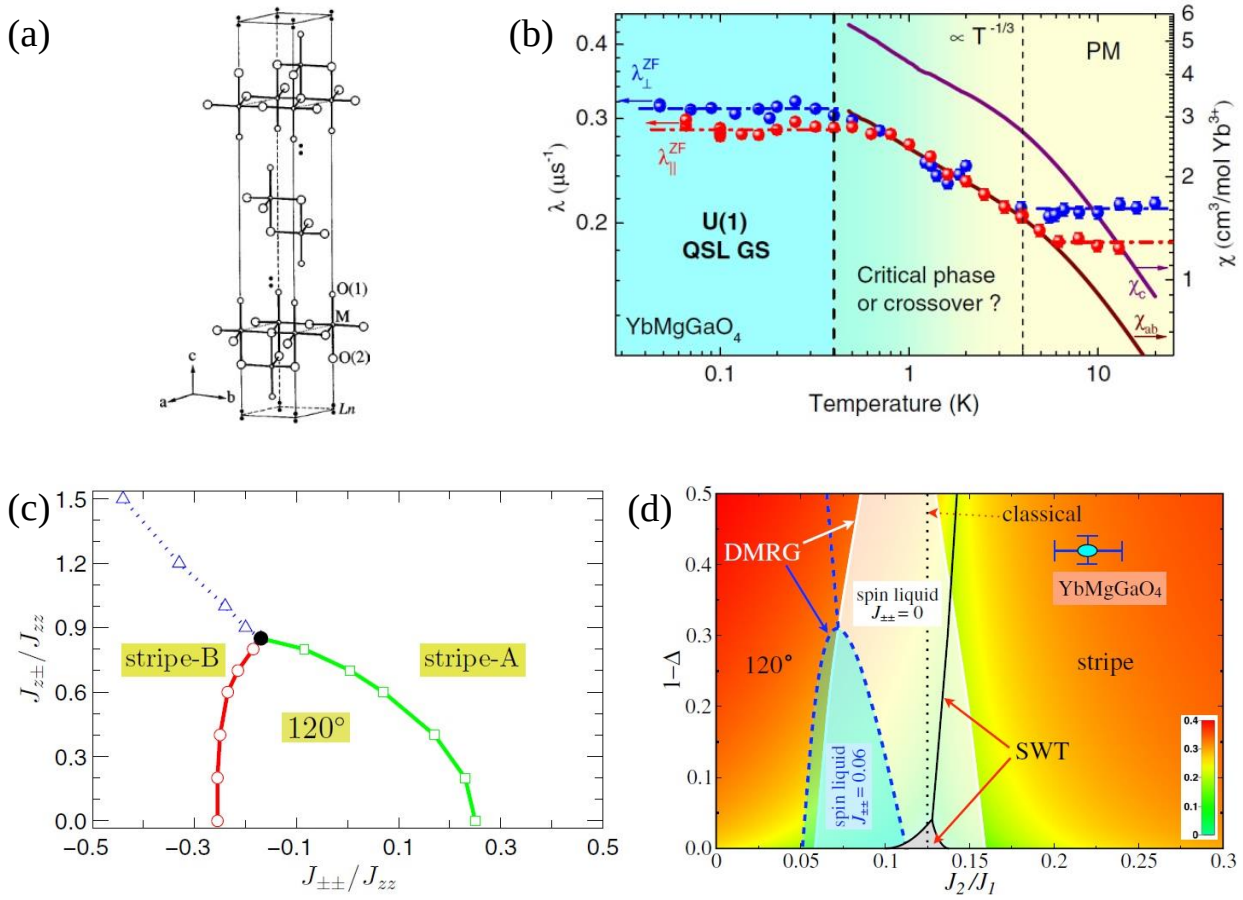

Figure 1.4: a) The crystal structure of the $LnM^{2+}M'^{3+}O_4$ family. This figure was taken directly from Ref. 18. b) A magnetic phase diagram constructed from μSR and bulk susceptibility measurements. This figure was taken directly from Ref. 23. c) A schematic quantum phase diagram constructed from the exact-diagonalization method of an XXZ model Hamiltonian. This figure was taken directly from Ref. 29. d) A phase diagram constructed from an XXZ model modified with pseudodipolar terms. This figure was taken directly from Ref. 30.

that are remarkably degenerate.[31] Single crystals were quickly grown by chemical vapor transport with properties matching those of the polycrystalline samples.[32, 33, 34] The mysterious ground state inspired several more experiments including μSR[35, 36, 37, 38], NMR[38], ESR[39, 40], nuclear quadrupole resonance (NQR)[38], and neutron scattering measurements[41] as well as several doping studies.[32, 42, 43, 44] The results revealed complex low temperature behavior best understood as a viscous spin liquid with slow dynamics, and the origin of this behavior is still being hotly debated.

One of the earliest theories proposed for the ground state of $NiGa_2S_4$ was the spin nematic phase,[45, 46] characterized by spin quadrupole moments with finite amplitudes which are prevented from attaining LRO due to quantum fluctuations. This theory can explain the T^2 behavior at low temperatures seen in Fig. 1.5(b) but not the slowly fluctuating internal field observed in the μSR, NQR, ESR, and neutron diffraction measurements. Another current theory suggests that there is a topological phase transition at low temperatures involving the binding and unbinding of vortices composed of twofold degenerate $S = 1$ spins known as Z_2 vortices.[47, 48, 49] Several experimental results support this theory including the significant slowing down of the spin dynamics at the transition temperature, a peak in the specific heat at a slightly higher temperature than the transition temperature as shown in Fig. 1.5, and the results of the temperature dependence of the ESR linewidth which suggest that the Z_2 vortex binding transition occurs at the transition temperature while the vortices disturb the spin dynamics associated with the 2D critical slowing down above the transition temperature. On the other hand, this topological transition does not account for the finite correlation length at low temperatures in $NiGa_2S_4$ or the spin size effects observed in the doping studies. The phase transition has also been modeled as a Berezinskii-Kosterlitz-Thouless (BKT) transition,[50] which results from the proliferation of vortices and antivortices in a 2D superfluid, and has been analyzed as a product of C_3 symmetry breaking[51], but these models also have their flaws. Even after several years of research, further experiments are necessary in order to fully understand this system.

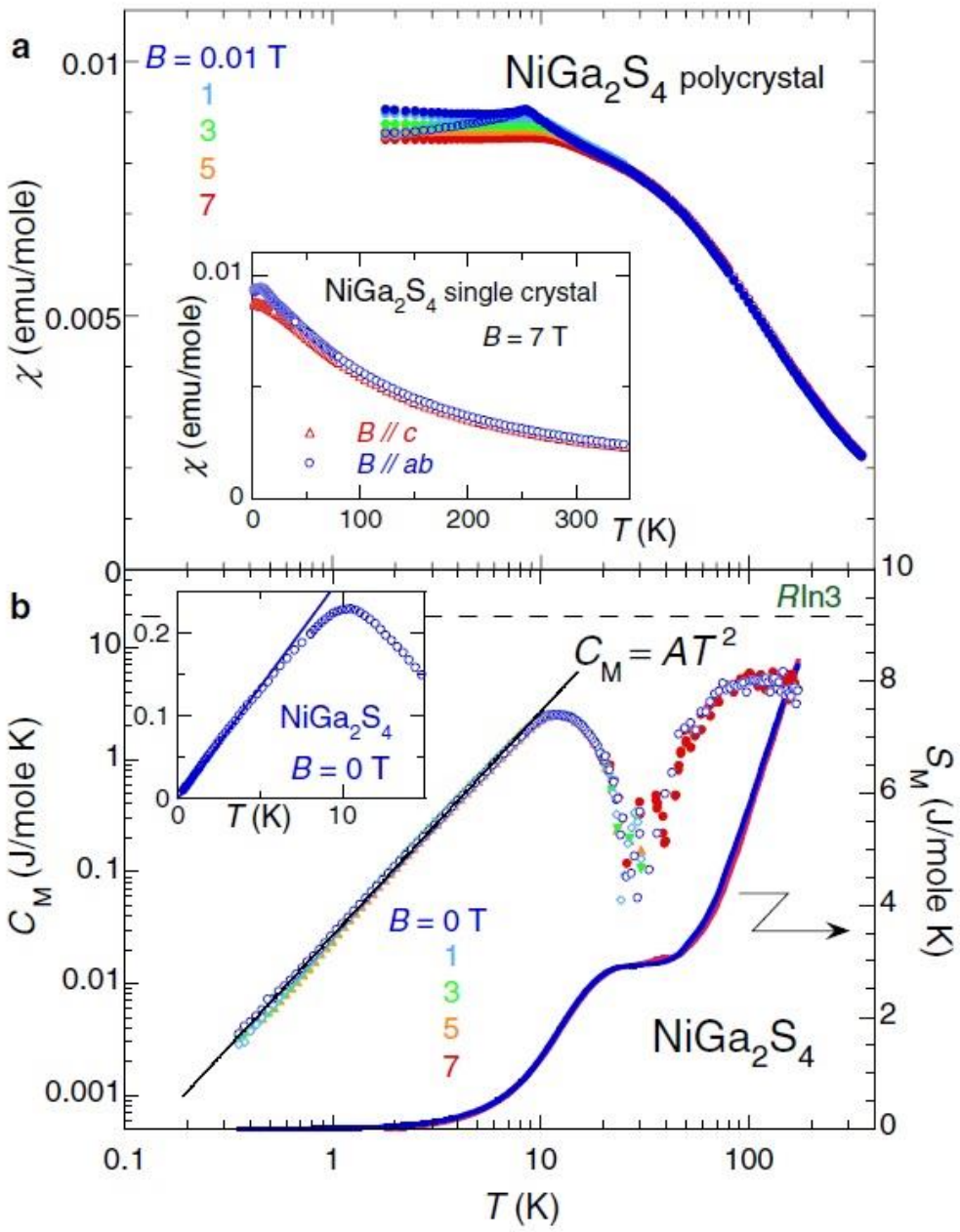

Figure 1.5: a) The field cooled (solid circle) and zero-field cooled (open circle) dc susceptibility of polycrystalline $NiGa_2S_4$ measured under different fields. Inset: For a single crystal sample, the *ab*-plane and *c*-axis components are shown for B = 7 T. b) For polycrystalline samples, the magnetic specific heat under different temperatures, and the entropy measured at 0 T (blue) and 7 T (red). These figures were taken directly from Ref. 34.

1.2.3 Coplanar 120 Degree State and the Related Field Induced Spin State Transitions

While Anderson postulated the RVB state as the ground state of the $S = 1/2$ AFM Heisenberg model,[3] more recent work has shown that the ground state has magnetic LRO with a 120 degree structure.[52, 53, 54, 55] One interesting sample that exhibits a non-collinear 120 degree state is $Ba_3CoSb_2O_9$. $Ba_3CoSb_2O_9$ was first synthesized by Blasse in 1965,[56] and the initial characterization of polycrystalline samples that followed revealed a hexagonal structure with a pseudo 2D triangular lattice formed by the Co^{2+} ions and an AFM transition which occurs near 3.8 K.[57, 58]. Furthermore, powder neutron diffraction measurements revealed that, due to the weak interlayer interactions, the compound adopts a non-collinear 120 degree structure in the *ab*-plane.[58] A few years later, single crystal samples were synthesized, and the initial magnetic susceptibility measurements matched very closely with theoretical calculations made for 2D $S = 1/2$ triangular lattice Heisenberg antiferromagnets (TLHAFs); moreoever, the magnetization also revealed a plateau at one-third of the saturation magnetization M_S, indicative of an up-up-down (*uud*) spin state, as shown in Fig. 1.6(a).[59]

The existence of a stabilized $M_S/3$ state in a system whose symmetry precludes DM effects inspired several more experiments in order to probe the magnetic properties. Single crystal neutron measurements,[60] high-field magnetization and ESR measurements,[61] NMR spectroscopy measurements in zero field and high magnetic fields,[62] and high-resolution sound velocity measurements[63] were all used in an effort to fully explore the intricacies of the system. A magnetic phase diagram is shown in Fig. 1.6(b), and the results for $\mu_0 H \parallel a$ are consistent with 2D isotropic Heisenberg models.[63] Furthermore, several theoretical approaches using a quantum XXZ model and numerical cluster mean-field methods have been very successful modeling this system as a 2D TLHAF;[64, 65, 66, 67, 68] yet, as close to perfect as the system may seem, recent INS experiments have revealed a high-energy excitation continuum which is inconsistent with any current theory and will require a new theoretical framework to explain.[69, 70] Such findings are a strong reminder

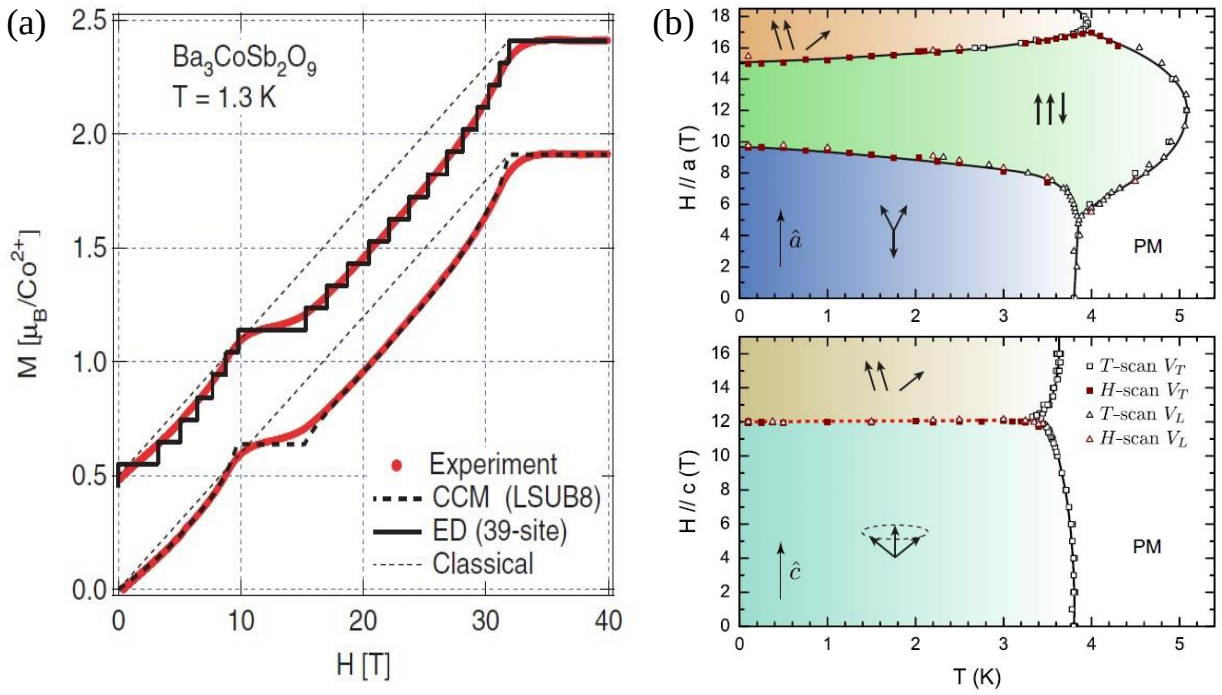

Figure 1.6: a) The magnetization curve corrected for Van Vleck paramagnetism. This figure was taken directly from Ref. 58. b) Magnetic phase diagram for μ_0H $\parallel$ a and μ_0H $\parallel$ c. This figure was taken from Ref. 62.

that theoretical advances rely on the findings of new measurements and new materials in order to advance.

1.2.4 Multiferroicity

In general, a material is considered multiferroic when the magnetism and ferroelectricity coexist, and multiferroics are split into two groups: materials in which the magnetism and ferroelectricity originate from different sources and are largely independent are type-I multiferroics whereas materials in which the magnetism causes the ferroelectricity are type-II multiferroics.[71] $Ba_3MnNb_2O_9$ is a fascinating example of a type-II multiferroic. While $Ba_3MnNb_2O_9$ was first synthesized years ago, it was not recognized as a multiferroic material until recently.[72] At first, $Ba_3MnNb_2O_9$ was synthesized via solid state reactions and found to have trigonal $P\bar{3}m1$ symmetry where the Mn^{2+} and Nb^{5+} ions are mostly ordered; furthermore, the dielectric properties of the system were found to be highly dependent upon the extent of this ordering.[73] In the trigonal system, it was determined that disorder was

introduced into the system via rotational twinning and translational stacking faults.[74] As complex perovskites gained more attention in the following years, $Ba_3MnNb_2O_9$ was revisited in order to further characterize the magnetic and electric properties of the system.

Polycrystalline samples of $Ba_3MnNb_2O_9$ were analyzed using high-field susceptibility, magnetization, and specific heat measurements as well as ESR spectroscopy.[75] This work showed that $Ba_3MnNb_2O_9$ undergoes a paramagnetic to antiferromagnetic transition around 3.2 K, and the Curie-Weiss analysis revealed that the Mn^{2+} ions are in the high spin $S = 5/2$ configuration. Additionally, the ESR spectra determined that short-range AFM correlations begin to develop near 18 K, well above the transition temperature.[75] Further analysis of the specific heat, ac and dc susceptibility, and dc magnetization as well as neutron powder diffraction (NPD) measurements and density functional theory (DFT) calculations revealed three separate magnetic transitions which correspond to a 120 degree Y phase, an *uud* phase, and an oblique phase as shown in Fig. 1.7.[76] Additionally, dielectric constant and polarization measurements revealed that while the material is in the Y phase, it is ferroelectric.[76] Interestingly, no polarization is seen for either the *uud* or the oblique phase which distinguishes $Ba_3MnNb_2O_9$ from other similar perovskites.[77, 78] As the ferroelectricity is concomitant with the magnetic phase, $Ba_3MnNb_2O_9$ is a confirmed multiferroelectric material.

1.3 Synthesis and Characterization

The four examples above clearly demonstrate how experimental and theoretical physics grow hand-in-hand. Without a theoretical framework, experiments have no reference for success, and without tangible results, theories have no way to diagnose their flaws. The two sides feed off one another in order to survive, and in the process both end up thriving.

The search for new materials will always be an important undertaking. Technologies today use the best materials at hand, but that does not mean they are the optimal materials. Corporations are constantly searching for new compounds with exotic magnetic and electric properties. By synthesizing a large variety of materials and characterizing their properties, new paths open for theoretical calculations as well as material engineering which may lead

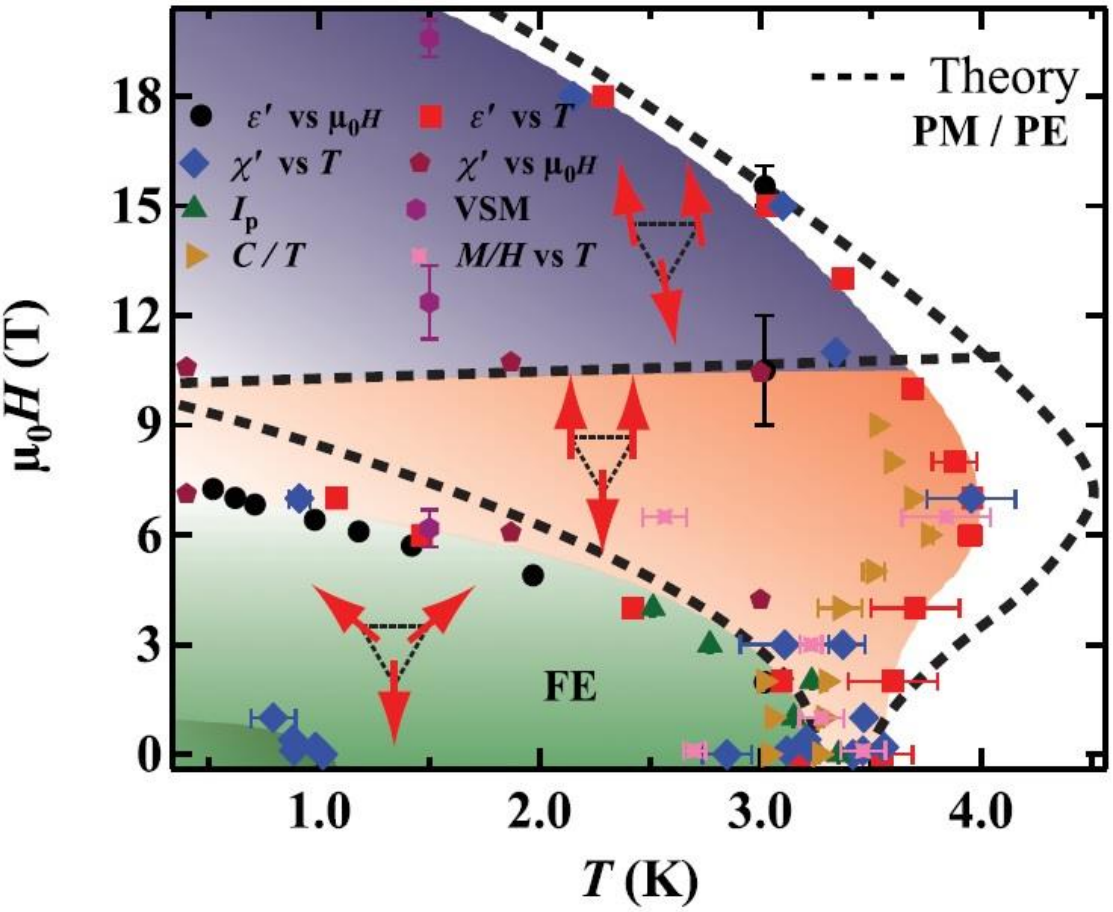

Figure 1.7: The experimental magnetic phase diagram of $Ba_3MnNb_2O_9$. This figure was taken from Ref. 75.

to useful results that can be seen in everyday life such as the semiconductors found in all modern electronics. It is for these reasons that the search for new materials must continue.

In the following chapters of this manuscript, the synthesis and characterization of two families of materials will be presented. First, the layered perovskite $R\mathrm{Cr}(\mathrm{BO}_3)_2$ (R = Y and Ho) is analyzed in hopes of finding a multiferroic material. Second, materials composed of Mo clusters are studied in hopes of finding a QSL state as well as to probe the effects of asymmetry in the Kagome lattice. Hopefully the results of these studies will inspire additional works that provide a more fundamental understanding of these and other exotic ground states.

Chapter 2

Experimental Methods

This chapter provides a brief introduction to most of the research techniques used for sample synthesis and characterization. This will include details on XRD, ac and dc susceptibility and magnetization, specific heat, resistivity, μSR, and neutron diffraction measurements which were used to examine the structural, magnetic, and transport properties of the materials. Each of these complementary techniques was crucial in characterizing the materials studied in this dissertation.

2.1 Sample Synthesis

Polycrystalline samples of $R\mathrm{Cr}(\mathrm{BO}_3)_2$ (R = Ho and Y) were synthesized by solid state reactions. The stoichiometric mixture of $\mathrm{Ho}_2\mathrm{O}_3/\mathrm{Y}_2\mathrm{O}_3$, $\mathrm{Cr}_2\mathrm{O}_3$, and $\mathrm{B}_2\mathrm{O}_3$ were ground together and pressed into 6-mm-diameter 60-mm rods under 400 atm hydrostatic pressure to form rods of $R\mathrm{Cr}(\mathrm{B}_{1.15}\mathrm{O}_3)_2$ and then calcined in Argon at 1100° C three times: once for 12 hours and twice for 36 hours each, adding an extra 10% of $\mathrm{Cr}_2\mathrm{O}_3$ by weight before each 36 hour annealing.

Similarly, polycrystalline samples of $\mathrm{Li}_2\mathrm{In}_{1-x}\mathrm{Sc}_x\mathrm{Mo}_3\mathrm{O}_8$ (x = 0.2, 0.4, 0.6, 0.8, and 1.0) and (Mg,Zn)$\mathrm{ScMo}_3\mathrm{O}_8$ were synthesized by solid state reactions. The stoichiometric mixture of $\mathrm{Li}_2\mathrm{MoO}_4/\mathrm{MgO}/\mathrm{ZnO}$, Mo, MoO_3, and $\mathrm{In}_2\mathrm{O}_3/\mathrm{Sc}_2\mathrm{O}_3$ were ground together and pressed into 6-mm-diameter, 60-mm rods under 400 atm hydrostatic pressure to form rods of $\mathrm{Li}_2\mathrm{In}_{1-x}\mathrm{Sc}_x\mathrm{Mo}_3\mathrm{O}_8$, $\mathrm{Zn}_{1.25}\mathrm{ScMo}_3\mathrm{O}_8$, or $\mathrm{Mg}_{1.35}\mathrm{ScMo}_3\mathrm{O}_8$. The rods were placed in alumina

crucibles before being sealed in silica tubes at a pressure of 10^{-4} mbar. Finally, the samples were annealed in a box furnace at 850° C for 48 hours for the Li samples and 1000° C and 1150° C for 48 hours and 24 hours, respectively, for the Mg/Zn samples..

While polycrystalline samples are crucial for research–and have lead to several publications for our group[79, 80, 81, 82, 83, 84, 85]–as they reveal bulk properties and are generally much easier to produce, single crystal samples are also needed in order to obtain spatially dependent information. While not discussed in this dissertation, several other samples were grown as single crystals by the traveling-solvent floating-zone technique, such as the $Fe_{1-x}Co_xV_2O_4$ family, which were subsequently used for many successful experiments.[86, 87, 88, 89, 90]

2.2 X-ray Diffraction and Structural Refinements

Powder x-ray diffraction is an important technique for gathering bulk structural information about a sample. In particular, powder XRD measurements were used to determine the quality of samples, to check for the presence of impurities, and to determine lattice constants, atomic positions, and bond lengths for the samples presented in this dissertation. Like all powder diffraction, powder XRD spectra are determined from Bragg's law which states $2dsin\theta = n\lambda$, where d is the interatomic distance, θ is the scattering angle, n is a positive integer, and λ is the wavelength of the incident wave as shown in Fig. 2.1. X-rays interact with the valence electron cloud of the atoms, so the scattering power of an atom is dependent on its number of electrons; furthermore, the intensity of XRD has a strong $sin\theta/\lambda$ dependence, so the data quality may decline at high momentum values. Even so, XRD is a valuable tool because it is relatively non-destructive, affordable, and quick.

XRD measurements were obtained from small pieces of polycrystalline sample which were ground into a fine powder. The resulting powder XRD patterns were recorded at room temperature with a HUBER Imaging Plate Guinier Camera 670 with Ge monochromatized Cu $K_{\alpha 1}$ radiation (1.54059 Å). Measurements were taken at room temperature between 4 $\leq 2\theta \leq 100$ ° with $\Delta 2\theta = 0.05°$. The diffraction patterns were analyzed using the Rietveld refinement software package $FullProfSuite$ with typical refinements for all samples having

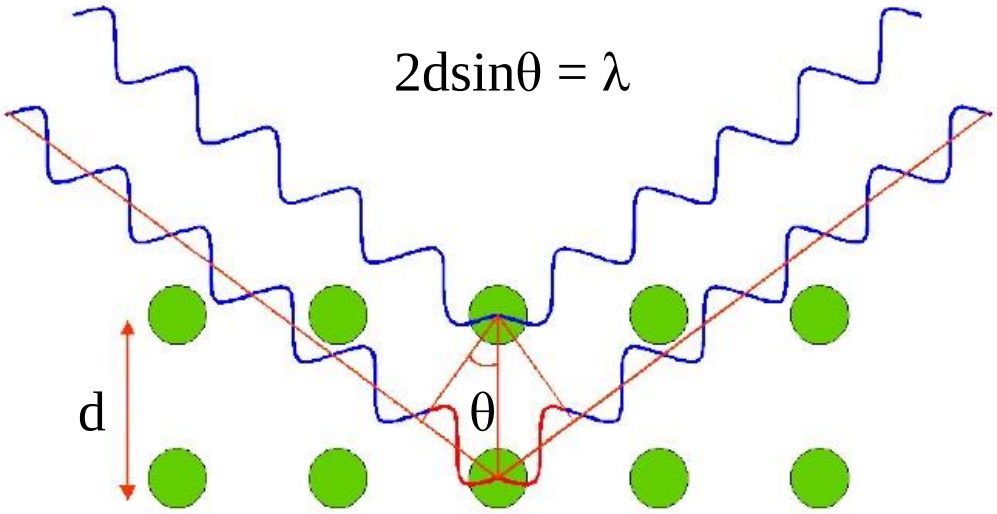

Figure 2.1: A schematic diagram of Bragg diffraction.

$\chi^2 \approx 1 \sim 2$.[91] Peak shapes were modeled using a pseudo-Voigt function convoluted with an axial divergence asymmetry function, and the backgrounds were obtained through a linear interpolation of manually chosen background points with refinable heights.

2.3 Specific Heat

In general, the specific heat measures the change in the average kinetic energy of the particles as heat is added to the system. For this dissertation, we have specifically measured the isobaric specific heat capacity $C_P = (dQ/dT)$, and the measurements in this dissertation were used to determine magnetic transition temperatures and to help classify the type of magnetic transitions that occurred. As the system cools to absolute zero, a purely classical and magnetically isolated system would see C_P also drop to zero as there would be no energy left for the transport particles to interact; moreover, there is a low temperature maximum originating from thermal excitations between two states around k_bT known as the Shottky anomaly.[92] In reality, degrees of freedom can still be present at absolute zero including magnetic degrees of freedom like those in a QSL. In this case, the specific heat could be

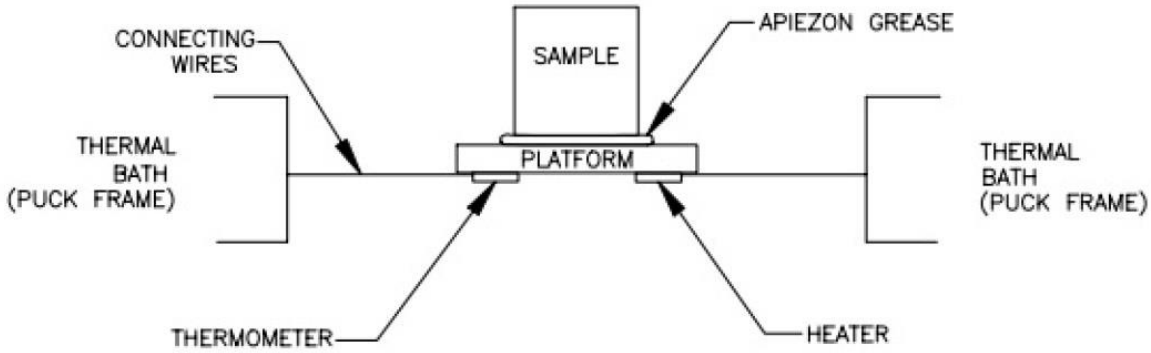

Figure 2.2: A schematic of the setup of the laboratory specific heat measurements.

propagated by the spin flips associated with the degenerate ground states. Maintaining these degrees of freedom leads to various other low temperature behaviors.

The specific heat measurements were performed on a Quantum Design Physical Property Measurement System (PPMS). In this system, the sample is mounted on a thermally conducting platform using apiezon grease to provide a thermal contact. The platform is attached to a heater and a thermometer; additionally, the platform is connected to a thermal bath which allows both the sample and the platform to achieve thermal equilibrium during measurements. This setup is shown in Fig. 2.2. In order to obtain an accurate measurement of the specific heat, the puck and grease are measured separately to determine the addenda specific heat which is then subtracted from the sample measurement. Temperatures as high as 350 K can be achieved using the heater, and a dilute refrigeration insert can achieve temperatures as low as 50 mK.

2.4 dc Susceptibility and Magnetization

Bulk magnetization $\vec{M}$ is one of the most elementary measurements of magnetic properties. By measuring the magnetic flux density $\vec{B}$ as a function of the external magnetic field $\mu_0\vec{H}$, magnetization can be calculated as $\vec{B} = \mu_0(\vec{H} + \vec{M})$. Similarly, the magnetic susceptibility χ which measures the change in magnetization with an external magnetic field can be calculated as $\vec{M} = \chi\vec{H}$ or $\vec{B} = \mu_0(1+\chi)\vec{H}$. In this dissertation, dc susceptibility

measurements were used to determine transition temperatures and to differentiate between FM and AFM transitions by applying various magnetic fields as well as to make magnetic phase diagrams. Magnetization measurements were used to determine saturated magnetic moments and transition field strengths as well as to probe the nature of the dominant FM or AFM interactions.

Paramagnetic (PM) materials will show a positive susceptibility that increases linearly with decreasing temperature as the unpaired electrons will align with the external magnetic field. On the other hand, diamagnetic materials will show a negative susceptibility as the electron pairs will rearrange in the presence of an external magnetic field which will create magnetic repulsion. This effect is generally weak and is overcome by other types of magnetic orderings. For example, ferromagnetic materials have the ability to easily align their magnetic domains with the external magnetic field and therefore will show a large positive susceptibility. Complex magnetic behavior is observed near the PM-FM transition temperature. Antiferromagnetic materials will show a smaller positive susceptibility which is related to the external magnetic field's ability to excite spins out of the magnetic ground state. The AFM-PM transition is generally observed as a peak followed by a reduction in the susceptibility upon decreasing temperatures.

The susceptibility in the PM region can be modeled as

$$\chi = \frac{C}{T - \theta_{CW}}, \tag{2.1}$$

where C is the Curie constant and θ_{CW} is the Curie temperature in Kelvin. Clearly, at $T = T_C$ a singularity appears. Furthermore, T_C will be zero for a purely PM ordering, positive for a FM ordering, and negative for an AFM ordering.

All dc susceptibility, χ_{dc}, and isothermal magnetization measurements were performed using a Magnetic Property Measurement System (MPMS) with a superconducting interference device (SQUID) magnetometer capable of measuring temperatures between 2-350 K and magnetic fields ranging from -6.5 T to 6.5 T.

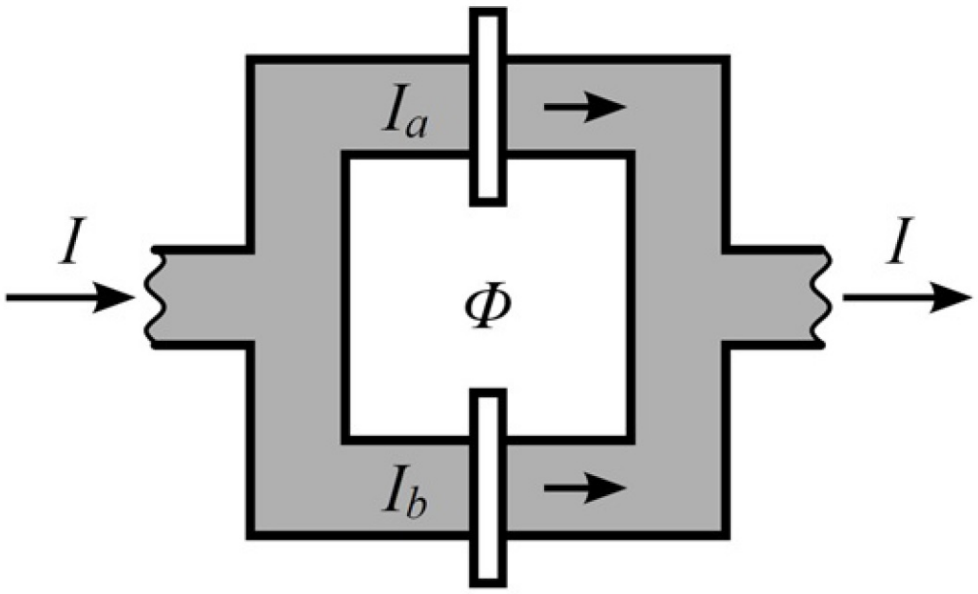

Figure 2.3: A schematic diagram of the SQUID magnetometer.

Magnetic dc susceptibility (χ_{dc}) measurements were made using a Magnetic Properties Measurement System (MPMS) with a superconducting interference device (SQUID) magnetometer. Measurements were made after cooling in zero field and in a measuring field of μ_0H = 0.1T over the temperature range between 2 K and 300K. The Curie temperature (θ_{CW}) was obtained by a Curie-Weiss (CW) fit of the inverse susceptibility. Isothermal magnetization M($\mu_0\vec{H}$) measurements were made using a Quantum Design Vibrating Sample Magnetometer (VSM) at 2 K with magnetic fields between -6.5 $\leq \mu_0\vec{H} \leq$ 6.5 T. For this setup, the sample is suspended in a coil of superconducting loops which contain two similar Josephson junctions as shown in Fig. 2.3. In the presence of a magnetic flux Φ, an electromotive force creates unequal currents across each junction. Thus, by varying the temperature while a constant field is maintained, Φ can be measured and used to calculate the temperature dependence of χ_{dc}. Similarly, by varying the magnetic field strength while maintaining a constant temperature, the bulk magnetization can be calculated.

2.5 ac Susceptibility

An important tool for characterizing magnetic properties, ac susceptibility χ_{ac} measurements introduce a small magnetic field created by an alternating current which is superimposed on the dc field. This causes the sample's magnetic moment to be time-dependent as opposed to the static moment measured by χ_{dc}. χ_{ac} measures the dM/dH of $\vec{M}(\mu_0\vec{H})$ curve and is therefore very sensitive to small changes in magnetization. Additionally, χ_{ac} measurements provide information about the magnetization dynamics. In this dissertation, χ_{ac} measurements were used to probe magnetic transition temperatures and critical field values as well as to determine any frequency dependence associated with a sample's magnetic transition.

The χ_{ac} measurements were performed at the National High Magnetic Field Laboratory (NHMFL) and were obtained using an ac-dc current calibrator (Valhalla Scientific, model 2700) and three lock-in amplifiers (Stanford Research, SR 830).[93] The phases of the lock-in amplifiers are set to measure each harmonic's signal, which is shifted from the oscillating magnetic field according to

$$E = A\{\chi_0^t h_0 \cos\omega t + \chi_1^t h_0^2 \sin 2\omega t - 3/4\chi_2^t h_0^3 \cos 3\omega t - ...\}, \tag{2.2}$$

where χ_0^t, $\chi_1^t h_0$, and $3/4\chi_2^t h_0^2$ are the first harmonic, second harmonic, and third harmonic components of χ_{ac}, respectively. The lock-in amplifiers are also set to read the linear component (first harmonic response) and the nonlinear components (second and third harmonic responses) with respect to the oscillating ac field frequency. The root mean square amplitude of the ac excitation field (h_0) varies from 0.43 to 4.3 Oe with the frequency (f) ranging from 40 to 1000 Hz. The applied external dc magnetic field ($\mu_0 H_{dc}$) was varied from 0 to 1000 Oe. The data was taken while warming up the sample from the base temperature with a rate of 7.6 mK/min with the zero-field-cooling process.

2.6 Resistivity

As magnetism stems directly from the order of electron spins, it is natural that studying other electronic properties would provide additional insight into the magnetic ordering. One property which is particularly important is electron mobility. Electron mobility distinguishes between metals, insulators, semiconductors, and semimetals and can be analyzed in bulk via resistivity, ρ, measurements. For free electrons in an electric field, the force, $\vec{F}$, is related to velocity, $\vec{v}$, and wavevector, $\vec{k}$, by $\vec{F} = m\frac{d\vec{v}}{dt} = \hbar\frac{d\vec{k}}{dt}$, and in a constant electric field $\vec{E}$ yields $\vec{j} = nq\vec{v} = \vec{E}/\rho = ne^2\tau\vec{E}/m$, where $\vec{j}$ is the electron current density, n is electron density, and τ is the collision time. Thus, ρ is defined as $m/ne^2\tau$.

When related to materials, the mobility of the electrons is determined by the electronic band structure. If we begin from the free electron picture, the electrons form Bloch waves of the form $\psi_k(\vec{r}) = \exp(i\vec{k}\cdot\vec{r})$. For a 1D periodic lattice, the Bragg condition $(\vec{k}+\vec{G})^2 = k^2$ indicates that diffraction will occur at $k = \pm\frac{1}{2}G = \pm n\pi/a$ where n is an integer and a is the lattice constant. At these points, a superposition of waves traveling in both directions creates a standing wave of $\psi(\pm) = \exp(i\pi x/a) \pm \exp(-i\pi x/a)$. Analyzing the location of the electrons for each standing wave using the probability given by $p(\pm) = |\psi(\pm)|^2$ yields $p(+) \propto \cos^2(\pi x/a)$ and $p(-) \propto \sin^2(\pi x/a)$. This framework implies that $\psi(+)$ weights electrons located on the atomic position while $\psi(-)$ weights electrons between the atomic positions. This results in an energy gap as a lower energy from $\psi(+)$ is produced due to the attractive nature of the nucleus/electron pair. This energy gap is not explained by the free model which predicts a continuum of allowable electron energies and, instead, indicates that the system has particular energy bands that the electrons are allowed to populate.

Materials where the Fermi energy, the energy of the outermost filled level in the ground state of the system, lies within an energy gap creates a filled energy band of electrons and leaves the lower electron band empty. Thus, applying an electric field will not mobilize the electrons unless they gain enough energy to clear the energy gap. For a partially filled band, particularly near half filling, the electrons are mobilized by an external electric field as there is no band gap constraining them. For materials with a nearly full band or materials that thermally excite electrons from a full band which partially fill the next are semiconductors.

Materials that have a mostly full outer band and a partially full subsequent band at zero temperature compose the semimetals. The complex band structures seen in real materials is a product of the complex nature of the system's crystal symmetry.

Resistivity measurements were performed using a Quantum Deisign Physical Properties Measurement System. Each maeterial's ρ was measured using the four-wire resistance method, where two wires measure the voltage difference across a sample and two separate wires provide the current across the sample. Combining this with Ohm's Law of $V = IR$, resistance (R) can easily be calculated. The relation of $\rho = R\frac{A}{l}$, where A is the cross-sectional area and l is the length, is then used to calculate the resistivity. To assist in the accuracy of this relationship, samples were pressed into pellets and cut using a rotating diamond saw into rectangular plates. The distance between the voltage leads on the sample was used to record the length, and the cross-sectional area was measured with calipers.

2.7 μSR

In general, magnetic resonance techniques utilize spin probes such as nuclei, electrons, and muons to investigate atomic scale magnetic properties. In this dissertation, μSR measurements were used to detect the presence of weak quasistatic magnetism in order to study possible disordered spin freezing. Two different methods were used. In time-differential μSR, positive muons (μ^+) are embedded into the sample such that they may interact with any local magnetic field at that site. The μ^+ then decay according to $\mu^+ \rightarrow e^+ + \nu_e + \vec{\nu}_\mu$ with the direction of the decay e^+ correlated to the spin orientation of the μ^+ at the time of the decay. Then, the time evolution of the muon spin polarization, $P(t)$, can be extracted from the asymmetry of the emitted positron's angular distribution. On the other hand, longitudinal-field μSR measures the decoupling of the relaxation rate of the μ^+ as a function of longitudinal field as the spin polarization decouples from a static field distribution when a sufficiently large magnetic field is applied parallel to the initial muon spin direction.

The μSR measurements were done at the quasi-continuous source at the Centre for Molecular and Materials Science of TRIUMF in Vancouver, Canada. Ultra-low temperature measurements in the range from 25 mK up to 3 K were performed at the M15 facility

equipped with a dilutions fridge while higher temperature measurements in the range of 1.8 K to 50 K were carried out at the M20 facility equipped with a variable temperature insert. For each sample, 0.5g of powder was spread on a copper ring holder and secured with aluminum foil. The samples were measured in both zero and longitudinal-field geometries for a range of temperatures. For each sample, a set of spectra at the same field and temperature was obtained at both the M15 and M20 facilities for comparison in order to account for any differences in the initial experimental asymmetry and background losses between the measurements at the two facilities.

2.8 Neutron Diffraction

One incredibly powerful material characterization tool is neutron diffraction. While x-rays interact with the electron cloud, neutrons scatter directly off the nucleus making them more effective at determining atomic positions, occupancy, and Debye-Waller factors. Additionally, neutrons possess a magnetic moment which allows them to interact with unpaired spins in magnetic materials and scatter accordingly. As a result, the magnetic structure of a material can be probed with this technique. Another advantage of neutrons over x-rays is that the scattering cross section can differ greatly for atomic isotopes, allowing one to engineer isotopic analogues to emphasize particular elements' contributions. This technique was used to minimize the neutron absorption by Boron in the $R\mathrm{Cr}(\mathrm{BO}_3)_2$ family.

For neutron studies, it is often more useful to model the experiment in terms of the momentum $\vec{(}k)$ where $\vec{k} = 2\pi m\vec{v}/h$. Here, m is the neutron mass, $\vec{v}$ the velocity, and h is Planck's constant. We can then define the scattering vector $\vec{Q}$ of a collision as $h\vec{Q}/2\pi = h(\vec{k} - \vec{k'})/2pi$. Elastic scattering occurs when there is no energy transfer which implies $|\vec{k}| = |\vec{k'}|$ and thus $|\vec{Q}| = |4\pi sin(\theta/\lambda)|$. If we consider inelastic scattering where energy transfer is possible, the calculations are much more complex. By making use of the Born approximation, Van Hove was able to model the scattering intensity as

$$I(\vec{Q}.E) = \frac{1}{h}\frac{k'}{k}\sum_{i,j} b_i b_j \int_{-\infty}^{\infty} \left\langle e^{-i\vec{Q}\cdot\vec{r_i}(0)} e^{-i\vec{Q}\cdot\vec{r_j}(t)} \right\rangle e^{i-(E/\hbar)t} dt, \tag{2.3}$$

where b is the scattering length of the nuclei, i and j are position labels such that nucleus j is at r_j at time t, and the angled brackets indicate a thermodynamic average over all possible configurations of the sample. In general, the nuclear spin is decoupled from the position of the nucleus, so Eq. 2.3 can be generalized as

$$I(\vec{Q}.E) = \sum_{i,j} \langle b_i b_j \rangle A_{ij} = \sum_{i,j} \langle b \rangle^2 A_{ij} + \sum_i \left(\langle b^2 \rangle - \langle b \rangle^2 \right) A_{ii}, \tag{2.4}$$

where A_{ij} represents the integral in 2.3. In this form, the first term represents the coherent scattering, resulting from neutrons scattering off of separate nuclei, and the second term represents the incoherent scattering, resulting from non-interfering scattered neutrons. Coherent scattering provides information about the atomic structure for elastic scattering and measures collective phenomena such as phonons and spin waves for inelastic scattering whereas incoherent scattering provides information about excitations of the nuclei or unpaired spins for elastic scattering and measures individual phenomena like atomic diffusion for inelastic scattering.

For unpolarized neutrons, the spin-only magnetic scattering cross section is defined as:

$$\frac{d^2\sigma}{d\Omega d\omega} = (\gamma r_0) \frac{2k'}{k} F^2 \left(\vec{Q} \right) e^{-2W(\vec{Q})} \sum_{\alpha \cdot \beta} \left(\delta_{\alpha\beta} - \frac{Q_\alpha Q_\beta}{Q^2} \right) S^{\alpha\beta} \left(\vec{Q}, \omega \right), \tag{2.5}$$

where γ = -1.91 is the gyromagnetic ratio of the neutron moment, r_0^2 is the nuclear cross section, $F(\vec{Q})$ is the magnetic form factor that usually falls off with increasing $\left|\vec{Q}\right|$, $e^{-2W(\vec{Q})}$ is the Debye-Waller factor, $\left(\delta\alpha_{13} - \frac{Q_\alpha Q_B}{Q^2} \right)$ is the polarization factor, and $S^{\alpha\beta}\left(\vec{Q}, \omega\right)$ is the magnetic scattering function. Note that the polarization factor indicates that neutrons can only couple to the magnetic moments that are perpendicular to $\vec{Q}$. This allows the direction of the magnetic moments to be unambiguously determined. Furthermore, the term $S^{\alpha\beta}(\mathbf{Q}, \omega)$ in the integral representation is given by:

$$S^{\alpha\beta}(\mathbf{Q}, \omega) = \frac{1}{2\pi\hbar} \sum_{j,j'} \int_{-\infty}^{\infty} e^{i\mathbf{Q}\left(\mathbf{R_i} - \mathbf{R'_j}\right)} \left\langle \widehat{S}_j^\alpha (0) \, \widehat{S}_j^\beta (t) \right\rangle e^{-i\omega t} dt. \tag{2.6}$$

where $\left\langle \widehat{S}_j^{\alpha}(0)\, \widehat{S}_j^{\beta}(t) \right\rangle$ describes the thermal average of the time-dependent spin operators, and $\mathbf{R_j}$ is the coordination of the magnetic moment at site j. Therefore, a neutron diffraction experiment measures the Fourier transform of the pair correlation function in space and time.

Lastly, the energy transfer $\hbar\omega$ in the INS experiments can be either positive or negative. Known as the principle of detailed balance, there is a scattering law of $S(\mathbf{Q},\omega)$ which, according to Boltzmann statistics, upon time reversal states that:

$$S(-\mathbf{Q},-\omega) = e^{-\frac{\hbar\omega}{k_B T}} S(\mathbf{Q},\omega). \tag{2.7}$$

This principle unambiguously relates the neutron energy-gain and energy-loss processes to each other.

2.8.1 Neutron Powder Diffraction

Neutron powder diffraction is a technique very similar to XRD except it uses neutrons rather than x-rays to scatter off of the material. In particular, NPD measurements were used to determine the lattice constants, atomic positions, magnetic structures, and magnetic moments of the samples presented in this dissertation. NPD data presented here was taken at the HB-2A powder diffractometer at the High Flux Isotope Reactor (HFIR) at Oak Ridge National Laboratory (ORNL). Powder diffraction data collected on this instrument are ideally suited for the Rietveld method.

The HB-2A powder diffractometer is used to conduct crystallographic and magnetic structural studies of powder and ceramic samples as a function of intensive conditions (such as temperature, pressure, and magnetic field). This instrument makes use of Debye-Scherrer geometry. HB-2A has a range of $2^\circ < 2\theta < 155^\circ$ covered by 44 ^{3}He detectors, and each detector is separated by $\sim 3^\circ 2\theta$. Consequently, the detector bank is moved to scan the desired 2θ. The neutrons are reflected off of a germanium wafer-stack monochromator to provide wavelengths of 1.54 and 2.41 Å. Collimation is provided by a 12' pre-sample collimator, a removable 21' post-sample collimator, and 12' collimators for each detector tube. Samples are loaded into aluminum or vanadium cans and can be mounted inside of a variety of sample environments. Due to the low background of HB-2A, measurements can be performed in

cryofurnaces (4-800 K), ^{3}He cryostats ($>$ 300 mK), dilute refrigeration cryostats ($>$ 30 mK), or furnaces ($<$ 1800 K). In addition, magnetic fields up to 7 T can be applied as well as high pressure cells, including diamond anvils.

Similar to the XRD data, NPD data can be refined using the Rietveld method and the $FullProfSuite$ software package. Due to powder averaging, Bragg reflections are often convoluted, causing multiple reflections to be located at the same position in 2θ. As a result, is is often not possible to isolate individual peaks in order to integrate them individually. Instead, one must also account for the geometry of the peaks which is determined by the configuration and geometry of the scattering instrument. For data collected at HB-2A, the peak shape is determined by a Thompson-Cox-Hastings pseudo-Voigt convoluted with an axial divergence asymmetry function[94] modeled with Gaussian and Lorentzian halfwidth components (H_G and H_L, respectively) of

$$H_G^2 = (U + D_{ST}^2)\tan^2\theta + V\tan\theta + W + \frac{I_G}{\cos^2\theta}, \tag{2.8}$$

$$H_L = X\tan\theta + \frac{[Y + F(S_Z)]}{\cos\theta}, \tag{2.9}$$

where U, V, and W are halfwidth parameters, D_{ST} is a strain parameter, I_G is an isotropic size effect, X is the Lorentzian isotropic strain parameter, Y is the Lorentzian isotropic size parameter, and $F(S_Z)$ is an isotropic size parameter.

In order to determine the magnetic propagation vector, $FullProfSuite$ includes the tool k-search. Reasonable candidates found via k-search were then input into SARAh-Representational Analysis to calculate magnetic structures allowed by the crystalline space group and the propagation vector. SARAh-Refine then allows for the selection of the irreducible basis of the magnetic symmetry.[95] A refineable magnetic phase is produced by the corresponding basis vectors of the magnetic structure. After the crystallographic structure parameters and all of the shape parameters have been established from a NPD pattern taken above the magnetic transition temperature, refinement of the magnetic phase is performed using a NPD pattern taken below the magnetic transition. The magnetic phase will gain a form factor of

$$F_h^2 = |\boldsymbol{F}_\perp(\boldsymbol{h})|^2 - (\boldsymbol{e} \cdot \boldsymbol{F_m}(\boldsymbol{h}))^2, \tag{2.10}$$

where $\boldsymbol{F_m}(\boldsymbol{h})$ is the magnetic structure factor and $\boldsymbol{e}$ is the unit vector along $\boldsymbol{h}$. By fixing the refined parameters from the crystalline structure, the magnetic structure can be refined by determining the coefficient for each of the magnetic basis vectors. Along with other experimental results and theoretical models, the refined magnetic structure is taken into consideration in order to determine the magnetic ground state of the sample.

2.8.2 Inelastic Neutron Scattering

Inelastic neutron scattering provides information about the energy dispersion of a material by measuring the magnetic scattering function S($\vec{Q}$,ω) with a certain energy transfer ($\hbar\omega$) and momentum transfer ($\vec{Q}$). The dispersion relation probes both the structural and magnetic properties of the material via phonons and magnons/spinons, respectively. In general, INS data is collected either using time of flight measurements or triple-axis spectrometers. Experimental INS results are instrumental in testing the limitations of theoretical models and offer a unique perspective into the spin dynamics of a system.

Inelastic neutron scattering measurements used in this dissertation were performed on a 5g polycrystalline sample of $YCr(BO_3)_2$ at the Cold Neutron Triple-Axis Spectrometer (CTAX) at HFIR in ORNL. Measurements were made using a fixed final energy of E_F = 5.0 meV in order to investigate a reasonable range of energy transfers and characterize the overall spectrum. A traditional triple-axis spectrometer, CTAX allows for variable incident energy and sample-analyzer distances, and the background levels are minimized by the Cold Guide 4 bender and guide hall shielding.

In order to simulate the spin wave spectrum generated by the INS data, we utilized the Matlab library SpinW.[96] SpinW uses classical Monte Carlo simulations as well as linear spin wave theory in order to solve a given spin Hamiltonian. The results were used to further corroborate the proposed magnetic structure as well as to investigate the NN and NNN exchange interactions.

Chapter 3

Magnetodielectric Triangular Lattice Antiferromagnets $R\mathrm{Cr(BO_3)_2}$ (R = Y and Ho)

Triangular lattice compounds have been widely studied for years due to their potential to exhibit exotic magnetic properties. One of the most sought after properties in these materials is multiferroicitiy. In this chapter, the synthesis and characterization of $R\mathrm{Cr(BO_3)_2}$ (R = Y and Ho) is presented. Both materials show distinct magnetodielectric behaviors, and replacing the non-magnetic Y^{3+} ion with the magnetic Ho^{3+} ion leads to interesting differences in their magnetic properties. The results of this chapter have been published in Ref. 115.

3.1 Introduction

While triangular lattices are a vast playground for interesting physics, another group of materials that commonly exhibit noteworthy properties is materials with layered structures. When a layered material has more than one magnetically active ion, the exchange interactions between the different magnetic ions on different layers possibly induce strong magnetoelectric (ME) behaviors. One well-studied system where the layered structure has a large effect is the magnetoelectric perovskites.[97, 98, 99] In particular, $SrNdFeO_4$[100, 101] and

$NdCrTiO_5$[102, 103, 104] are both layered perovskites with two different active magnetic ions on adjacent layers, and they both exhibit ME behaviors dependent upon the magnetic orderings or spin flop transitions. Therefore, from a materials engineering perspective, a compound with a magnetic triangular lattice, two different magnetic ions, and a layered structure may lead to strong ME or multiferroic properties.

With this in mind, we chose the system $R\mathrm{Cr}(\mathrm{BO}_3)_2$ (R = Y and Ho) to investigate. Individually, each of the orthoborates that compose the layered structure has interesting properties. For example, while YBO_3 contains no magnetically active ions, it has a high ultraviolet transparency and an astonishing optical damage threshold which makes it a practical material for industry purposes, especially when the Y-site is doped with Eu.[105, 106, 107, 108, 109, 110, 111] Additionally, while there have been a few hypothesized structures,[112, 113] more recent studies have shown that the crystal structure of YBO_3 is best described by the hexagonal $P6_3/m$ space group.[114] On the other hand, $CrBO_3$ contains magnetically active $S = 3/2$ Cr^{3+} ions. Initially, $CrBO_3$ was shown to possess rhombohedral $R\bar{3}c$ symmetry;[115] futhermore, dc susceptibility measurements revealed an AFM transition near 15 K where it was thought the spins align antiparallel along the c axis, and the Curie-Weiss analysis indicated an effective magnetic moment of 3.73 μ_B.[116] Further experiments revealed that $CrBO_3$ exhibits not only uniaxial but also hexagonal anisotropy.[117] Moreover, thorough magnetic measurements revealed that the effective moment is closer to 2.95 μ_B and that the magnetic structure is not as simple as first hypothesized.[118] Finally, initial measurements of $HoBO_3$ revealed a hexagonal structure modeled by the $P\bar{6}c2$ space group, an effective moment of 10.61 μ_B, and a negative Curie temperature of -4.2 K.[119] More recent experiments contradicted the initial crystal structure, positing instead that the system is best described by the monoclinic space group $C2/c$; moreoever, while Curie-Weiss analysis revealed an effective moment closer to 9.73 μ_B and a Curie temperature of -14 K, isothermal magnetization and specific heat measurements imply that the ground state of $HoBO_3$ is non-magnetic.[120]

Previous studies of $\mathrm{YCr}(\mathrm{BO}_3)_2$ and $\mathrm{HoCr}(\mathrm{BO}_3)_2$ have shown that they both crystallize in the rhombohedral space group $R\bar{3}$ and have dolomite-type structures with a small amount of anti-site disorder between the Y/Ho and Cr sites.[121] As shown in Fig. 3.1(a), both

Table 3.1: Magnetic moments for $YCr(BO_3)_2$ at $T = 1.5$ K determined from refined neutron diffraction measurements for (a) $\mu_0 H = 0$ T and (b) $\mu_0 H = 5.0$ T. This table can be found in Ref. 115.

$YCr(BO_3)_2$	Atom	x	y	z	Mx	My	Mz	M
(a)	Cr1	0	0	0	2.11(17)	2.11(17)	1.29(5)	2.47(24)
$T = 1.5$ K	Cr2	2/3	1/3	1/3	-2.11(17)	-2.11(17)	-1.29(5)	2.47(24)
$\mu_0 H = 0$ T	Cr3	1/3	2/3	2/3	-2.11(17)	-2.11(17)	-1.29(5)	2.47(24)
(b)	Cr1	0	0	0	2.41(17)	2.41(17)	2.06(15)	3.17(28)
$T = 1.5$ K	Cr2	2/3	1/3	1/3	2.41(15)	2.41(15)	2.06(15)	3.17(28)
$\mu_0 H = 5.0$ T	Cr3	1/3	2/3	2/3	2.41(15)	2.41(15)	2.06(15)	3.17(28)

the Y/Ho and Cr ions occupy octahedral sites which form a three dimensional network by sharing corner-oxygen ions. The BO_3 triangles also share the octahedra's oxygen atoms. Moreover, both the Y^{3+}/Ho^{3+} and the Cr^{3+} ions form a triangular lattice in the *ab*-plane as shown in Fig. 3.1(b). The intraplanar distance between the Ho/Cr ions is 4.76 Å, and the interplanar distance between the Ho/Cr ions is 5.86 Å. $YCr(BO_3)_2$ and $HoCr(BO_3)_2$ both also show magnetic transitions around $T_N \sim 8$ K. [121] Therefore, with two magnetic ions, $HoCr(BO_3)_2$ meets the requirements listed above and is a strong candidate for multiferroic behavior. Another advantage here is that by replacing the Ho^{3+} ions with non-magnetic Y^{3+} ions while retaining the same structure, a comparison between the Y-compound with one magnetic ion and the Ho-compound with two magnetic ions is established which will help us to better understand how exactly the extra magnetic ion affects the system.

Before now, no detailed studies on the magnetic and electric properties of this interesting system have been performed. Thus, with fresh motivation, we studied the $RCr(BO_3)_2$ ($R =$ Y and Ho) system with various experimental techniques including ac and dc susceptibility, dc magnetization, specific heat, elastic and inelastic neutron scattering, and dielectric constant measurements in order to characterize the magnetic ground states and investigate possible multiferroic properties of the system.[122]

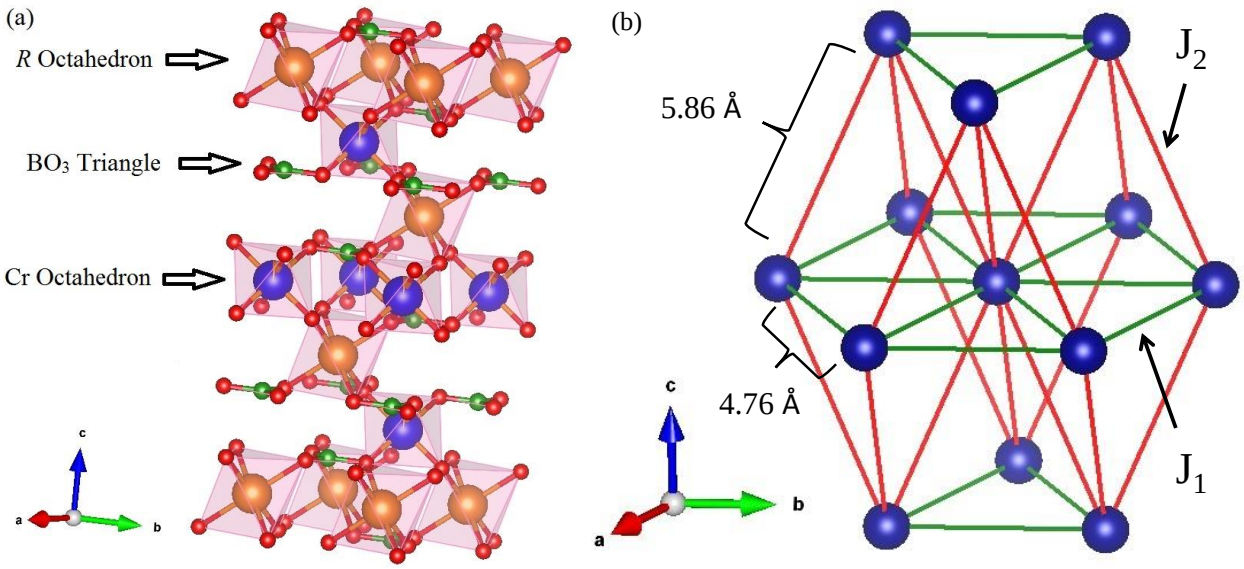

Figure 3.1: (a) The dolomite-type crystal structure of $R\mathrm{Cr}(\mathrm{BO}_3)_2$. The orange/blue R/Cr octahedra form a triangular lattice in the ab plane as shown in (b). Only the Cr ions are plotted here. The intralayer and interlayer exchange interactions are labeled as J_1 and J_2, respectively. This figure can be found in Ref. 115.

3.2 Synthesis and Characterization

3.2.1 $\mathrm{YCr}(\mathrm{BO}_3)_2$

First, polycrystalline samples of $\mathrm{YCr}(\mathrm{BO}_3)_2$ were synthesized as described in Ch. 2.1. In order to begin to probe the elementary magnetic properties of the system, dc susceptibility and isothermal magnetization measurements were performed on polycrystalline samples of $\mathrm{YCr}(\mathrm{BO}_3)_2$. In Fig. 3.2(a), we show the temperature dependence of the dc magnetic susceptibility measured between $\mu_0\mathrm{H} = 0.1$ and 3.0 T. At $\mu_0\mathrm{H} = 0.1$ T, there is a sharp peak at $T_N = 8$ K representing a magnetic transition. As the applied field is increased, T_N decreases and the peak begins to broaden. This temperature dependence of T_N suggests that the transition is antiferromagnetic in nature. At $\mu_0\mathrm{H} = 3.0$ T, T_N is no longer visible down to 2 K. The Curie-Weiss analysis of the $1/\chi$ data above 100 K shown in Fig. 3.2(b) yields an effective magnetic moment of $\mu_{eff} = 3.85\ \mu_B$ and a Curie temperature of $\theta_{CW} =$ -1.86 K which are in good agreement with the previously reported values.[121] While μ_{eff} matches closely with what one would expect for $S = 3/2$ Cr^{3+} ions, the dc magnetization measured at 2 K saturates around 2 μ_B, much smaller than the spin-only value of 3.87 μ_B

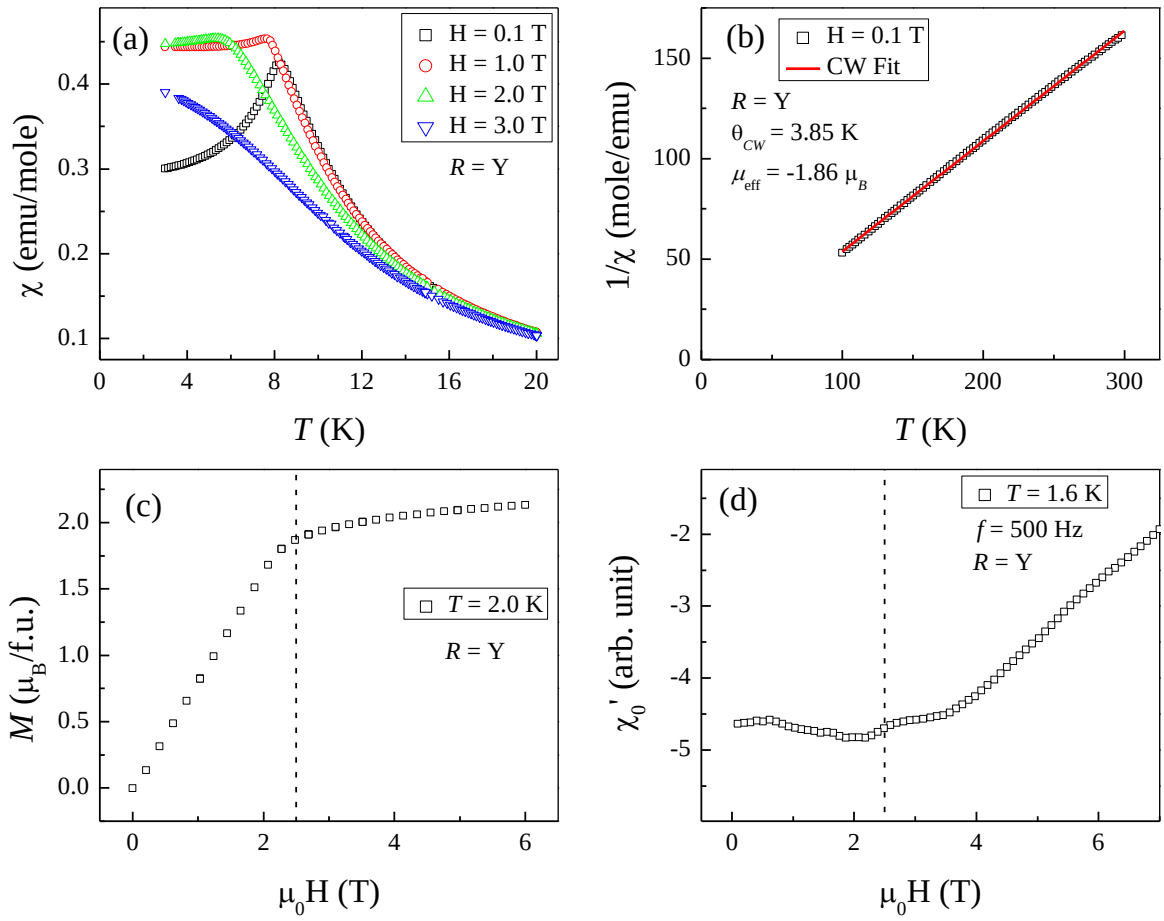

Figure 3.2: For $YCr(BO_3)_2$, (a) the temperature dependence of the dc susceptibility, (b) the Curie-Weiss analysis of the inverse dc susceptibility, (c) the magnetization curve, and (d) the field dependence of the ac susceptibility.

(Fig. 3.2(c)). There is also a notable slope change in the magnetization data measured at 2 K around $\mu_0 H = 2.5$ T.

Currently, it seems that this decreased magnetic moment is likely affected by the R/Cr anti-site disorder which has been characterized by Doi et al.[121] We estimate the anti-site disorder in our sample to be ∼3% from our elastic neutron scattering Rietveld refinements (as discussed below). In order to investigate this magnetic transition further, ac susceptibility measurements were utilized. While no frequency dependency was observed, a kink around $\mu_0 H = 2.5$ T can be seen in Fig. 3.2(d) suggesting a possible phase transition near this critical value, H_C.

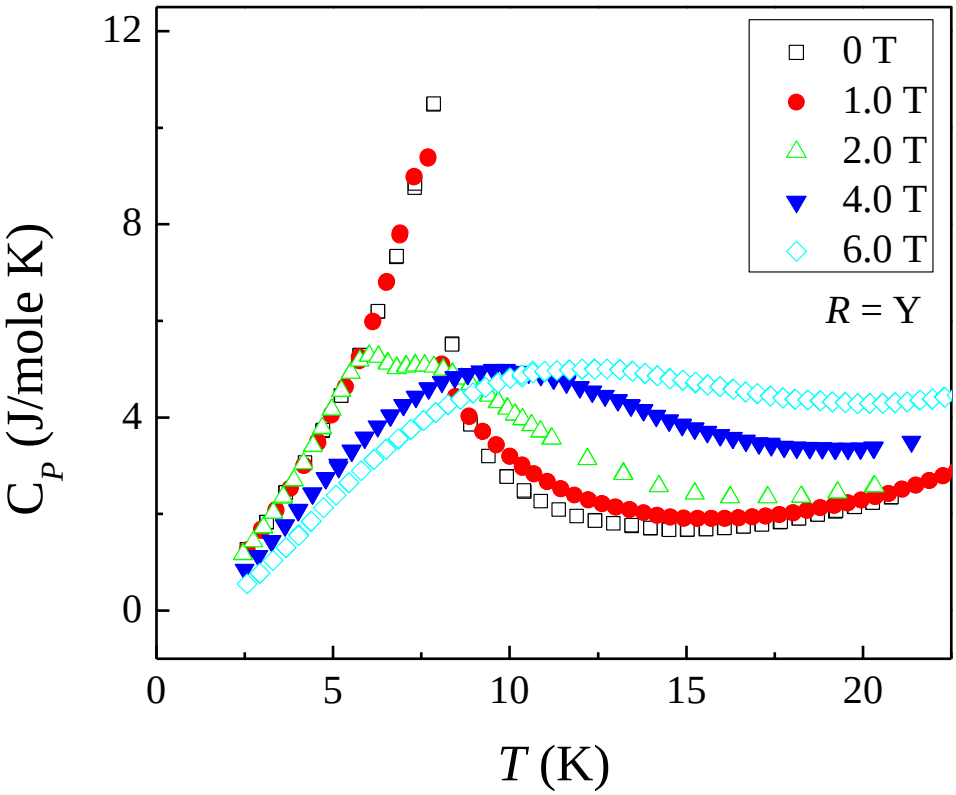

Figure 3.3: The zero-field cooled specific heat measured at various magnetic fields for $YCr(BO_3)_2$.

The temperature dependence of the zero-field cooled specific heat measurements is plotted in Fig. 3.3 for various magnetic fields. The data shows sharp λ-type anomalies at the same temperatures that the dc susceptibility measurements showed cusps at $T_N = 8$ K up to 1.0 T, indicative of an AFM transition as explained in Ch. 2.4. At fields of 2.0 T and higher, the sharp feature noticeably broadens. These results provides further evidence that this material undergoes an AFM transition at T_N unless a critical field H_C is applied.

After the preliminary magnetic measurements have provided some details into the nature of the magnetic transition in $YCr(BO_3)_2$, a NPD experiment was designed in order to characterize the magnetic ground state. The NPD pattern was first measured at room temperature for $YCr(BO_3)_2$ with a wavelength of 1.5405 Å in order to study the lattice information as shown in Fig. 3.4. The refinements yielded lattice parameters $a = 4.76422(6)$ Å and $c = 15.51574(28)$ Å and showed approximately 3% site disorder between the Y and Cr sites. Polycrystalline samples were also measured above ($T \sim 20$ K) and below ($T \sim 2$ K)

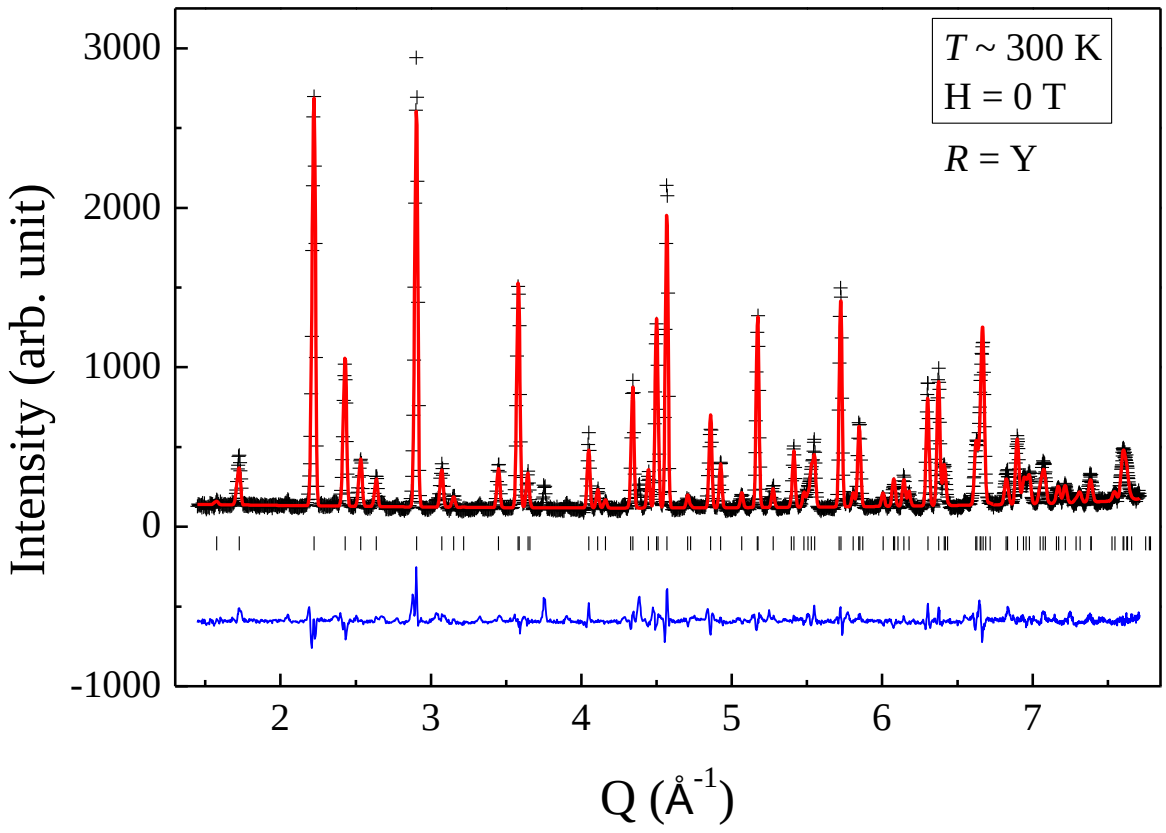

Figure 3.4: The elastic neutron diffraction patterns (crosses) for polycrystalline $YCr(BO_3)_2$ at room temperature and zero field using a wavelength of 1.5405 Å. The solid curves are the best fits from the Rietveld refinements using *FullProf Suite*. The vertical marks indicate the position of Bragg reflections, and the bottom curves show the difference between the observed and calculated intensities.

T_N as well as with applied fields up to μ_0H = 5.0 T at T = 1.5 K using a longer wavelength of 2.413 Å in order to study the magnetic structure information. The diffraction patterns and refinements can be seen in Fig. 3.5(a-c), and the results of the refinement are presented in Table 3.1.

For $YCr(BO_3)_2$ which contains only a single magnetic ion (Cr^{3+}), the NPD pattern clearly shows extra Bragg peaks at 2 K under zero field (Fig. 3.5(b)). These lattice forbidden reflections strongly suggest an AFM spin structure, and they can be described by a propagation vector $\vec{k}$ = (0, 0, 3/2). The magnetic structure resulting from the diffraction pattern refinement is shown in Fig. 3.6(c). The Cr^{3+} spins form a ferromagnetic configuration

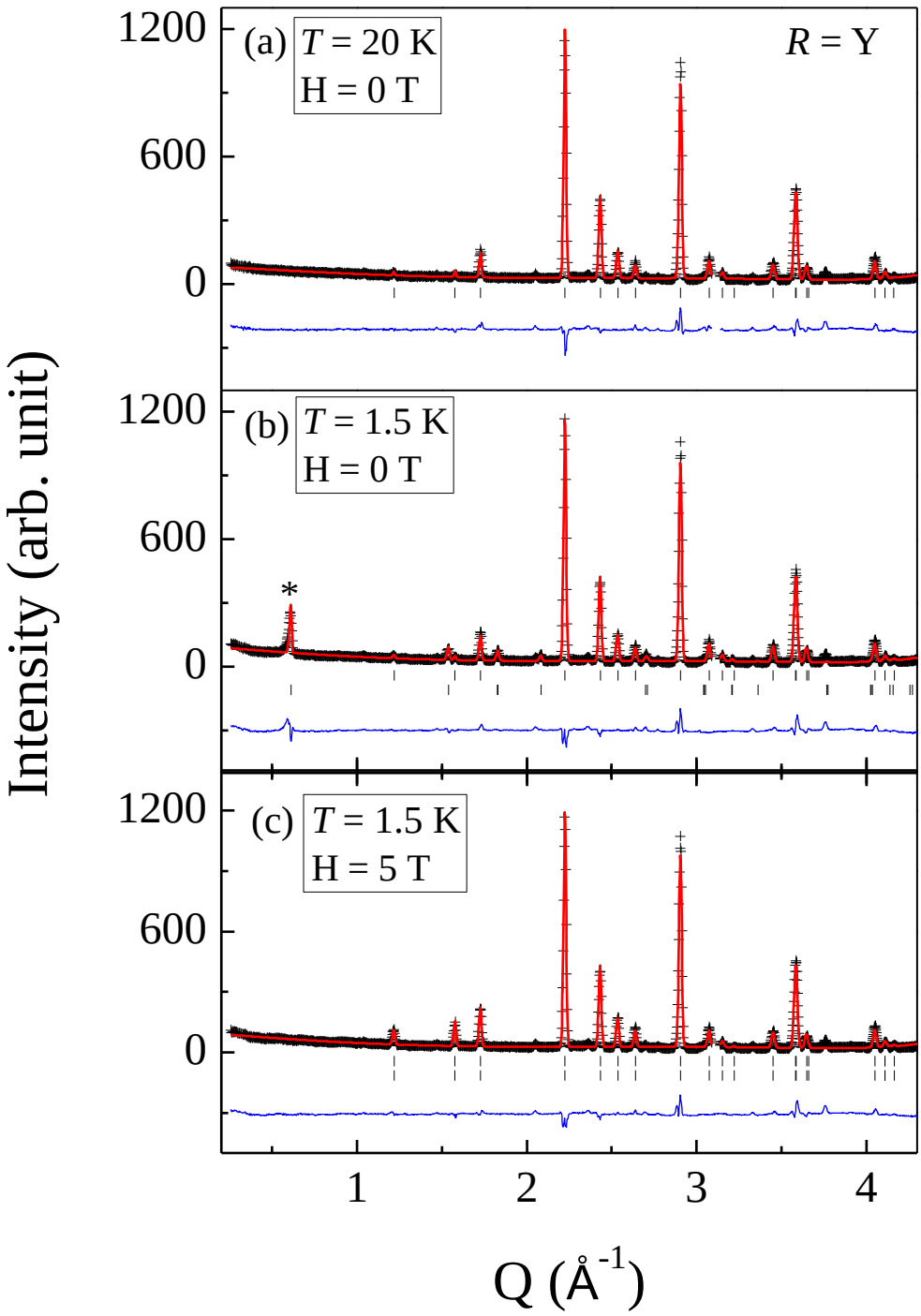

Figure 3.5: The neutron diffraction patterns for polycrystalline $YCr(BO_3)_2$ (crosses) at (a) $T = 20$ K and $\mu_0 H = 0$ T, (b) $T = 1.5$ K and $\mu_0 H = 0$ T, and (c) $T = 1.5$ K and $\mu_0 H = 5.0$ T using a neutron wavelength of 2.413 Å. The solid curves are the best fits from the Rietveld refinements using *FullProf Suite*. The vertical marks indicate the position of Bragg reflections, and the bottom curves show the difference between the observed and calculated intensities. The * in (b) marks the location of the (0, 0, 3/2) reflection. This figure can be found in Ref. 115.

in the *ab*-plane but tilt away from the *ab*-plane with a canting angle of 31.5°. Between the layers, the Cr^{3+} planes align antiferromagnetically.

The intensity of the (0, 0, 3/2) magnetic Bragg reflection was investigated as a function of both temperature and magnetic field as shown in Fig. 3.6(a-b). It not only disappears above T_N but also is suppressed by a critical magnetic field H_C = 2.5 T which agrees with our previous dc and ac susceptibility measurements. The NPD pattern measured at 2 K under $\mu_0 H$ = 5.0 T (Fig. 3.5(c)), larger than H_C, confirms that the material now adopts a FM ground state which is supported by the observed magnetic Bragg peaks which are at the same positions as the lattice Bragg peaks. This suggests a new propagation vector, $\vec{k}_{FM}$ = (0 0 0). As shown in Fig. 3.6(d), the refinement of the 5.0 T NPD pattern shows that in this FM state, the Cr^{3+} spins are aligned in the *ab*-plane with a canting angle of 40.6° away from the *ab*-plane. Therefore, a magnetic field above H_C flips the AFM arrangements of spins between the layers along the *c*-axis and aligns them ferromagnetically. The total magnetic moment for both the AFM and FM ground states is $\mu_{Cr} \sim 2.5\ \mu_B$ which is a bit smaller than the theoretical value for Cr^{3+} ions as well as the effective magnetic moment derived from our $1/\chi$ data.

After confirming the transition temperature and critical field value as well as defining the magnetic ground state through NPD measurements, INS measurements on polycrystalline samples were used to study the exchange interactions in the system. The critical field value near 2.5 T indicates a possible anisotropy gap near 0.5 meV at zero field which can be measured directly via INS measurements using cold neutrons. Figure 3.7 shows the inelastic neutron scattering profiles measured at 20 K and 1.5 K with various momentum transfers ($\vec{Q}$) ranging from 0.5 $Å^{-1}$ to 1.5 $Å^{-1}$. At each $\vec{Q}$, a peak in the intensity with the energy transfer (E) between 1-2 meV is clearly observed at 1.5 K which should represent the spin wave excitation in the magnetic ordered state. This feature disappears in the 20 K measurements suggesting that the observed peak is from the magnetic origin.

The spin wave excitation was analyzed to produce a spin wave spectrum within a limited E−Q space as shown in Fig. 3.8(a). The first branch of the spectrum is visible in our region of interest. The feature fattens out around $\vec{Q}$ = 0.8 $Å^{-1}$ and peaks near 1.5 meV. From the location of the magnetic peaks in Fig. 3(b), we expect the first zone boundary of the

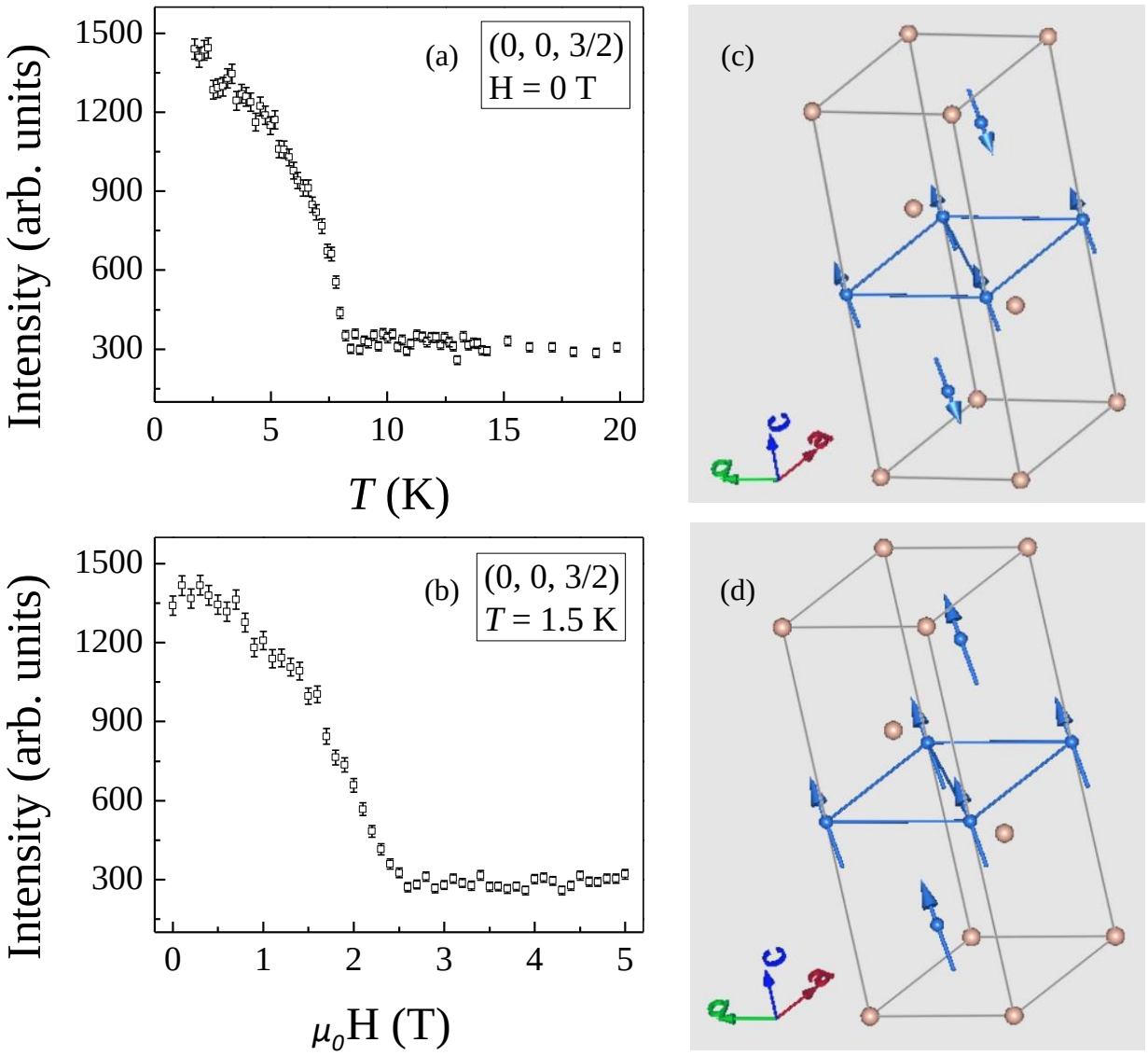

Figure 3.6: For $YCr(BO_3)_2$, (a) the temperature dependence and (b) the field dependence of the (0,0,3/2) magnetic Bragg reflection, and the magnetic ground state at (c) $\mu_0 H = 0$ T and (d) $\mu_0 H = 5.0$ T. This figure can be found in Ref. 115.

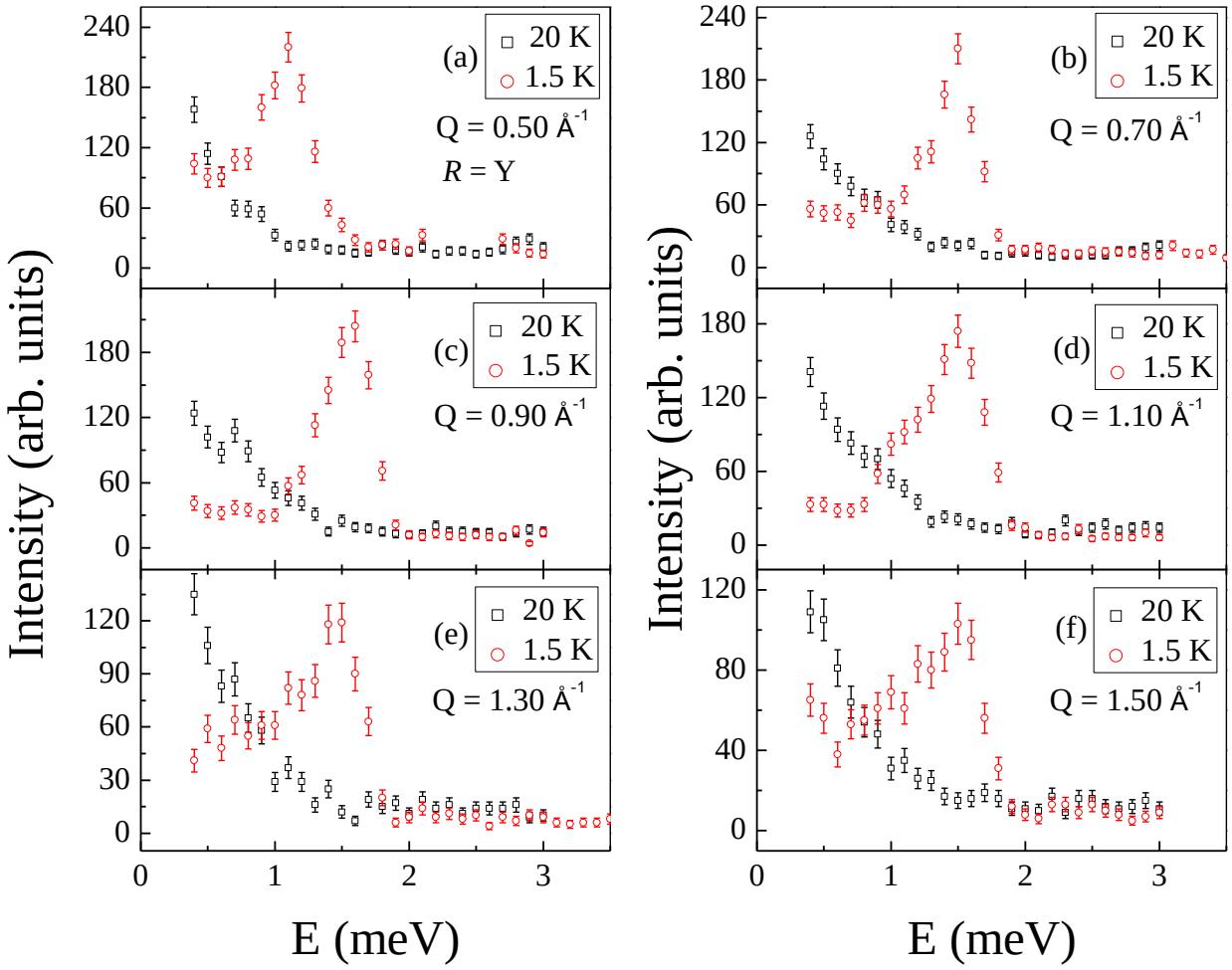

Figure 3.7: Inelastic neutron scattering profile above (black squares) and below (red circles) the transition temperature with $E_F = 5.0$ meV centered at (a) Q = 0.50 Å^{-1}, (b) Q = 0.70 Å^{-1}, (c) Q = 0.90 Å^{-1}, (d) Q = 1.10 Å^{-1}, (e) Q = 1.30 Å^{-1}, and (f) Q = 1.50 Å^{-1}. Note that a spurion centered around 2.3 meV has been removed from (a). This figure can be found in Ref. 115.

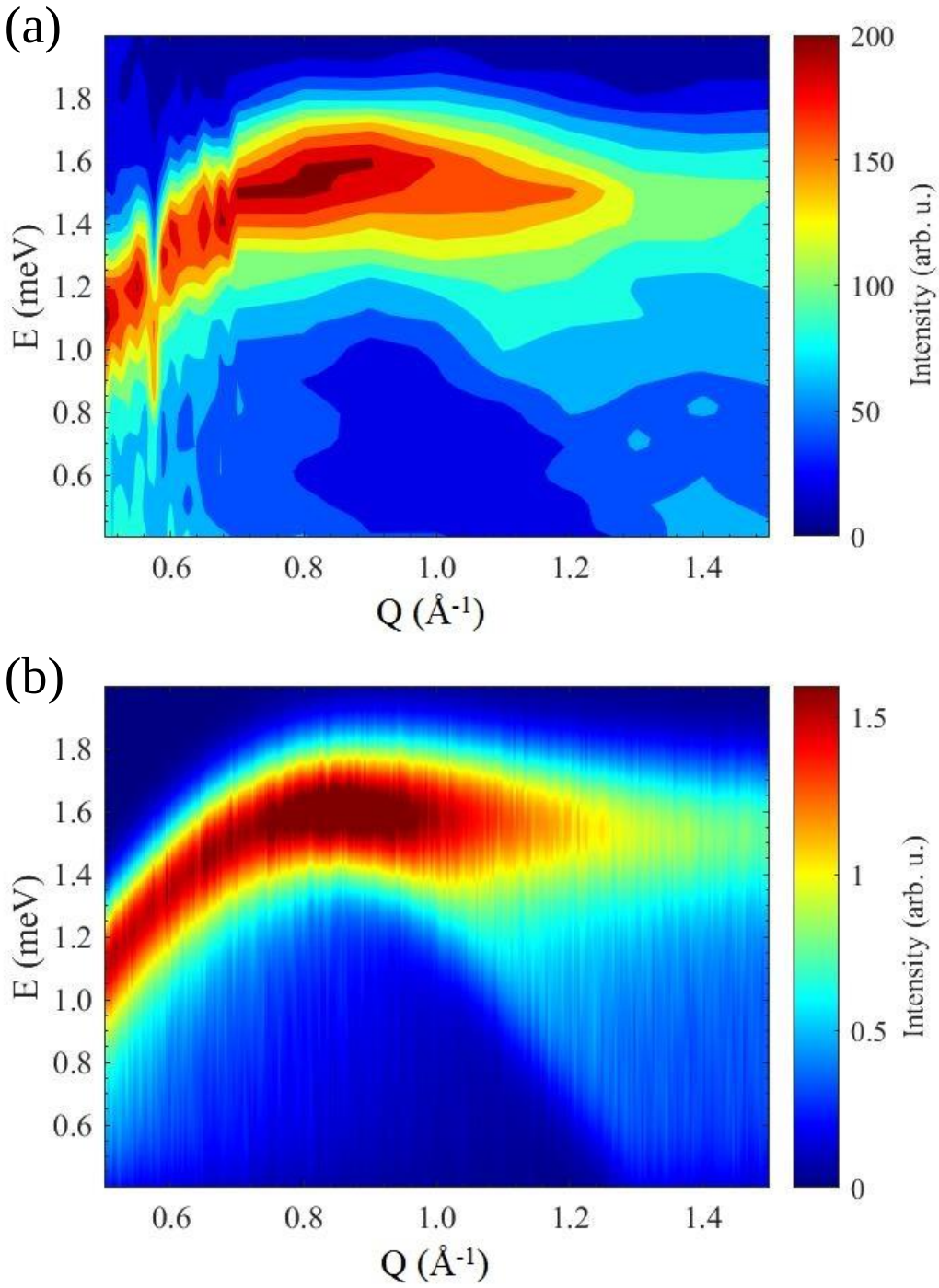

Figure 3.8: The (a) measured and (b) calculated powder-averaged spin wave dispersion for $YCr(BO_3)_2$ measured at $T = 1.5$ K. This figure can be found in Ref. 115.

spectrum to be centered near $\vec{Q} = 0.60$ Å^{-1} and the second zone boundary to be centered near $\vec{Q} = 1.53$ Å^{-1}. Unfortunately, no anisotropy gap was observed in the available data, but the spectrum can still be modeled in order to estimate the magnetic exchange interactions in the system.

In order to simulate this spin wave spectrum, we used the Matlab library *SpinW* to model the system.[123] *SpinW* uses classical Monte Carlo simulations as well as linear spin wave theory in order to solve the spin Hamiltonian:

$$H = \sum_{i,j} S_i J_{ij} S_j + \sum_i S_i A_i S_i + B \sum_i g_i S_i \tag{3.1}$$

where S_i are spin vector operators and J_{ij} are 3x3 matrices which describe pair coupling between spins, A_{ij} are 3x3 anisotropy matrices, B is the external magnetic field, and g_i is the g-tensor.

For our model, the Hamiltonian is greatly simplified as the powder sample averages out all anisotropy effects and as the sample was measured under zero field. Therefore, the spin Hamiltonian is left with the following terms:

$$H = \sum_{i,j} S_i J_{ij} S_j \tag{3.2}$$

Our *SpinW* models included the nearest neighbor intralayer interaction J_1 as well as the next nearest neighbor (NNN) interlayer interaction J_2. The values for J_1 and J_2 were determined empirically by comparing the simulated spin wave spectrum against the experimental data. J_1 = -0.12 meV determines the general size and location of the feature, and J_2 = 0.014 meV determines the slope of the branch. Specifically, J_2 changed the initial energy value where the branch begins at $\vec{Q} = 0.50$ Å^{-1} and the maximum energy value of the branch achieved near $\vec{Q} = 0.90$ Å^{-1}. Several values of J_1 and J_2 were tested in order to closely match the experimental results.

The final result is shown in Fig. 3.8(b). The simulation was constructed using a finite energy resolution consistent with the elastic line for $E_F = 5.0$ meV of dE = 0.3 meV . Similar to the measured data, the simulation shows one branch which begins near 1.0-1.2 meV at $\vec{Q} = 0.50$ Å^{-1}, fattens around $\vec{Q} = 0.80$ Å^{-1}, and fades into the second zone boundary.

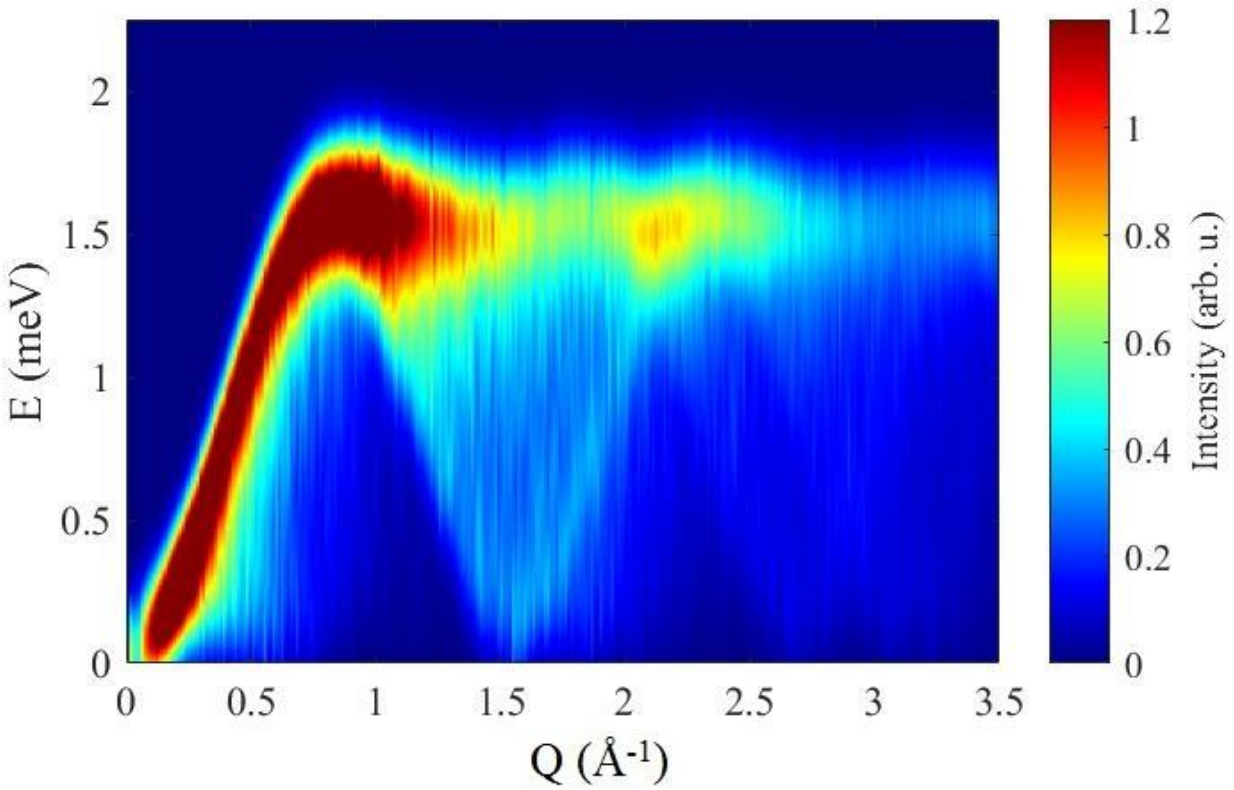

Figure 3.9: The calculated powder-averaged spin wave dispersion for $YCr(BO_3)_2$ measured at $T = 1.5$ K in an expanded E$-Q$ space.

Moreover, both the measured and the calculated data show very little intensity below 1.0 meV of transferred energy. Although we expected to find a spin gap with a magnitude close to 0.5 meV, both the measured data and the simulation appear to be gapless. Our simulation provides a good overall agreement with the experimental data which reasonably suggests that the intralayer interaction is at least one order of magnitude stronger than the interlayer interaction in $YCr(BO_3)_2$.

As our *SpinW* simulation matches our experimental results quite closely, the E$-Q$ range was expanded in order to further investigate the system. Figure 3.9 shows the calculated spin wave spectrum from 0 meV $\leq$ E $\leq$ 2.25 meV and 0 Å^{-1} $\leq \vec{Q} \leq$ 3.5 Å^{-1}. Again, the system appears to be gapless according to our simulation. Moreover, the second zone boundary is now clearly visible, and the location of the branches matches the refinement of the magnetic structure shown in Fig. 3.5(b) nicely. This model provides additional evidence

that our proposed magnetic ground state accurately describes the system; however, more INS experiments are necessary in order to develop this theory.

Finally, with a good grasp of the magnetic ground state in hand, electric polarization and dielectric constant measurements were used to investigate potential magnetoelectric phenomena. The capacitance was measured on thin-plate polycrystalline samples with an Andeen-Hagerling AH-2700A commercial capacitance bridge using a frequency of 20 kHz which was analyzed to obtain the dielectric constant data by approximating the sample as an infinite parallel capacitor. The pyroelectric current was measured using a Keithley 6517A electrometer during warming after the sample was cooled in an electric field from above T_N.

Fig. 3.10(a) shows the magnetic field dependence of ϵ for $YCr(BO_3)_2$. Below $T = 1.5$ K, the data shows a sharp peak around $\mu_0 H = 3.0$ T as well as a clear minimum near $\mu_0 H = 1.5$ T. Above $T = 1.5$ K, only the sharp peak near $\mu_0 H = 3.0$ T remains visible. Above T_N, this behavior disappears. Fig. 3.10(a) shows the temperature dependence of the dielectric constant, ϵ, for $YCr(BO_3)_2$. At zero field, ϵ shows a cusp near 8 K. While this feature broadens consistently with the strength of the applied field, the amplitude and transition temperature are more complicated. The amplitude increases with increasing applied field up to the critical field $\mu_0 H = 3.0$ T at which point it begins to decrease as the applied fields get even larger. On the other hand, the transition temperature decreases with increasing applied field up to $\mu_0 H = 3.0$ T and then increases with larger applied fields.

While $YCr(BO_3)_2$ was studied via pyroelectric current measurements at different magnetic fields, no electric polarization was observed for bulk polycrystalline samples around the transition temperatures. It is possible that a single crystal sample could produce an anisotropic polarization which is hidden by the powder averaging of the results or that the system is already ordered in an antiferroelectric state. Further experiments including Polarization vs. Electric field hysteresis measurements on single crystal samples may be necessary to elucidate the matter.

3.2.2 $HoCr(BO_3)_2$

Now that the compound containing one magnetic ion has been adequately studied, it is time to introduce a second magnetic ion and observe the effects. Polycrystalline samples

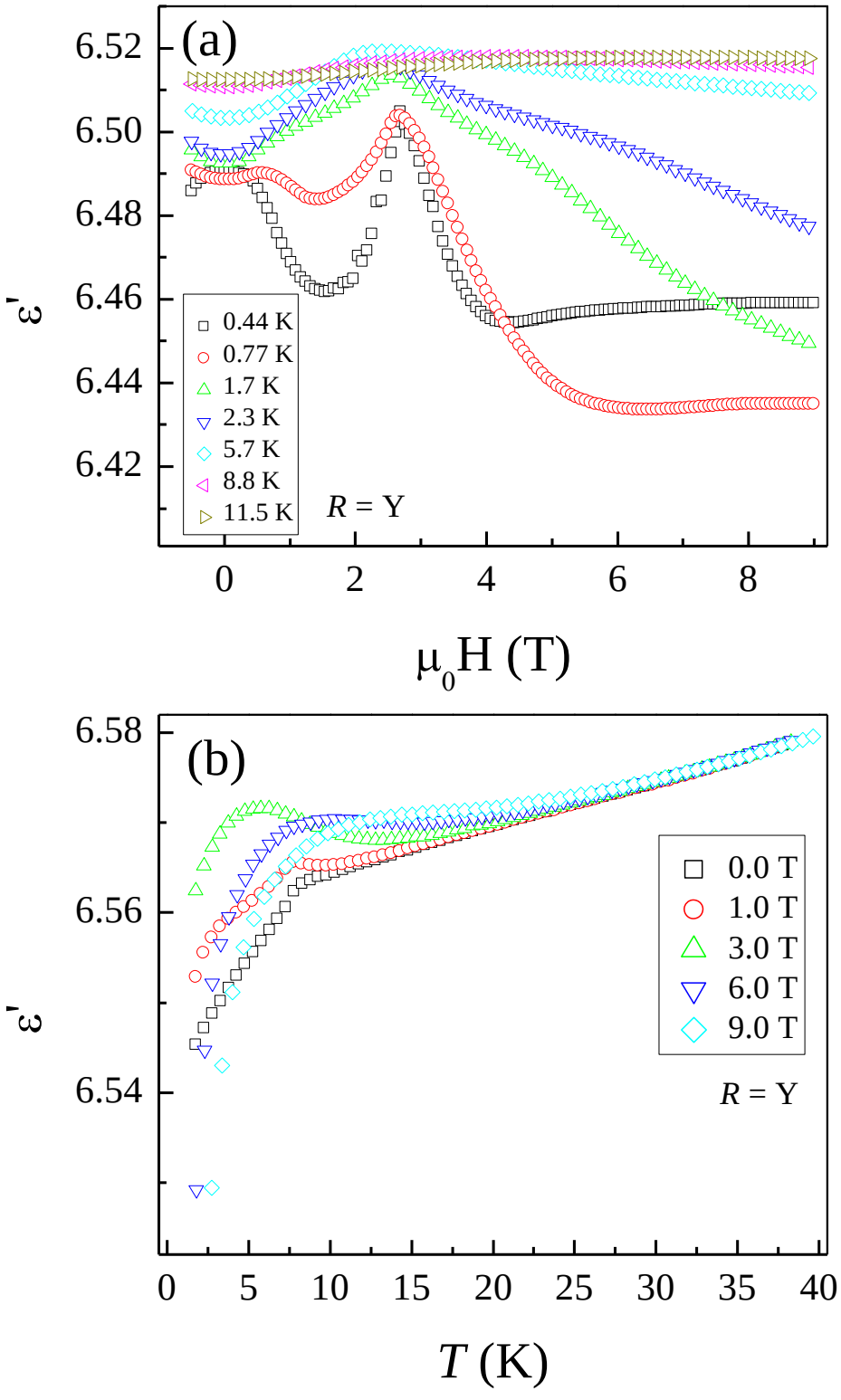

Figure 3.10: For $YCr(BO_3)_2$, (a) the field dependence of the dielectric constant measured at 20 kHz at varying temperatures, and (b) the temperature dependence of the dielectric constant measured at 20 kHz under applied fields. This figure can be found in Ref. 115.

Table 3.2: Magnetic moments for $HoCr(BO_3)_2$ at T = 1.5 K determined from refined neutron diffraction measurements for (a) μ_0H = 0 T and (b) μ_0H = 4.0 T.

$HoCr(BO_3)_2$	Atom	x	y	z	Mx	My	Mz	M
(a) T = 1.5 K μ_0H = 0 T	Cr1	0	0	0	2.44(9)	2.44(9)	1.87(4)	3.07(13)
	Cr2	2/3	1/3	1/3	-2.44(9)	-2.44(9)	-1.87(4)	3.07(13)
	Cr3	1/3	2/3	2/3	-2.44(9)	-2.44(9)	-1.87(4)	3.07(13)
	Ho1	0	0	1/2	0.0	0.0	0.0	0.0
	Ho2	2/3	1/3	5/6	0.0	0.0	0.0	0.0
	Ho3	1/3	2/3	1/6	0.0	0.0	0.0	0.0
(b) T = 1.5 K μ_0H = 4.0 T	Cr1	0	0	0	1.19(11)	1.19(11)	3.25(31)	3.46(35)
	Cr2	2/3	1/3	1/3	1.19(11)	1.19(11)	3.25(31)	3.46(35)
	Cr3	1/3	2/3	2/3	1.19(11)	1.19(11)	3.25(31)	3.46(35)
	Ho1	0	0	1/2	1.10(8)	1.10(8)	6.80(25)	6.89(27)
	Ho2	2/3	1/3	5/6	1.10(8)	1.10(8)	6.80(25)	6.89(27)
	Ho3	1/3	2/3	1/6	1.10(8)	1.10(8)	6.80(25)	6.89(27)

of $HoCr(BO_3)_2$ were synthesized as described in Ch. 2.1. Again, the elementary magnetic properties of the system were probed using dc susceptibility and isothermal magnetization measurements on polycrystalline samples of $HoCr(BO_3)_2$. In Fig. 3.11(a) the temperature dependence of the dc magnetic susceptibility measured between μ_0H = 0.1 and 3.0 T also shows an AFM transition at T_N = 9 K which decreases with applied field and vanishes at μ_0H = 3.0 T. The Curie-Weiss analysis of the $1/\chi$ data above 100 K shown in Fig. 3.11(b) resulted in an effective magnetic moment of μ_{eff} = 10.99 μ_B and a Curie temperature of θ_{CW} = -15.1 K which are again in good agreement with the previously reported values.[121] The dc magnetization measured at 2 K shown in Fig. 3.11(c) saturates around 9 μ_B, and there is a slope change which appears around μ_0H = 2.0 T.

In order to investigate this magnetic transition further. ac susceptibility measurements were utilized. While no frequency dependency was observed, the field dependence of the ac susceptibility measured at 0.3 K shown in Fig. 3.11(d) also reveals a clear feature near μ_0H = 2.0 T. We again propose that these results indicate a critical field around μ_0H = 2.0 T for the system.

The temperature dependence of the zero-field cooled specific heat measurements is plotted in Fig. 3.12. The data shows a sharp λ-type anomaly at the same temperature that the dc susceptibility measurements showed cusps at T_N = 9 K. This provides further evidence that

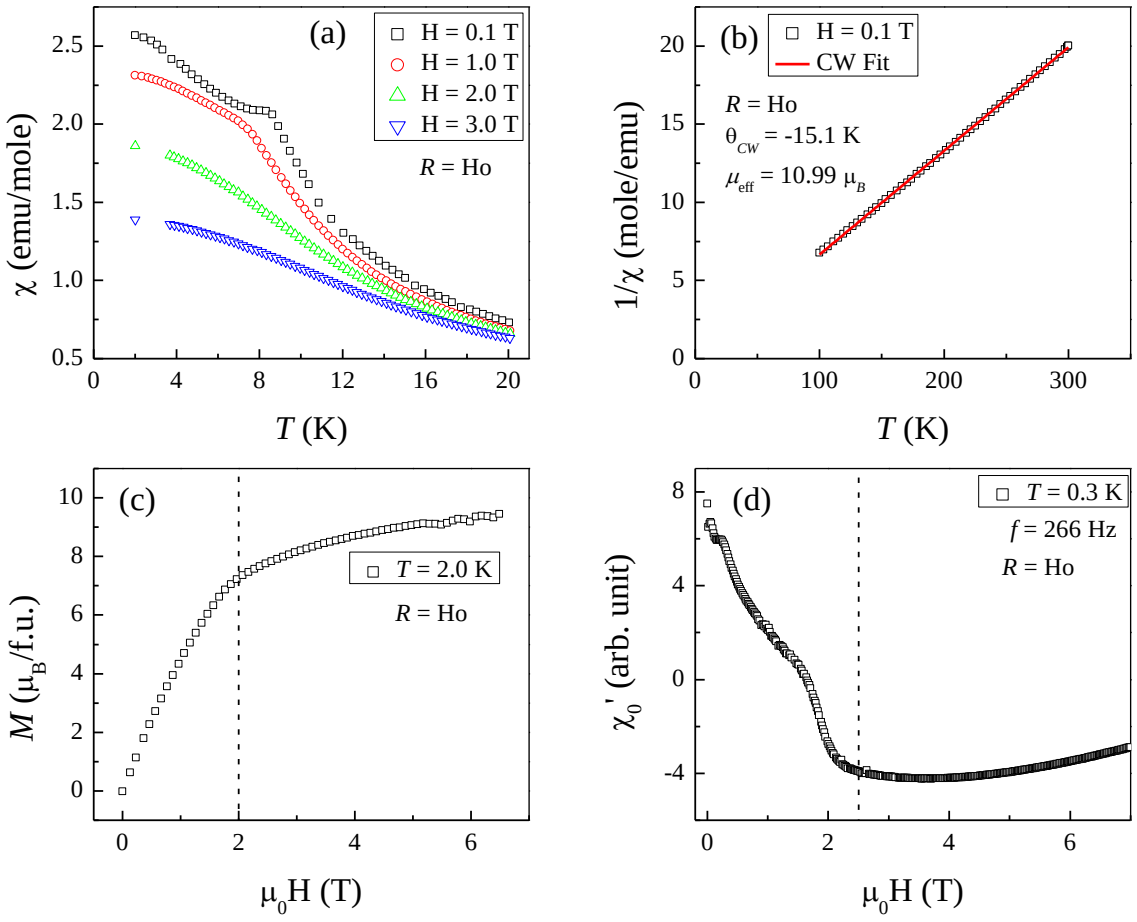

Figure 3.11: For $HoCr(BO_3)_2$, (a) the temperature dependence of the dc susceptibility, (b) the Curie-Weiss analysis of the inverse dc susceptibility, (c) the magnetization curve, and (d) the field dependence of the ac susceptibility.

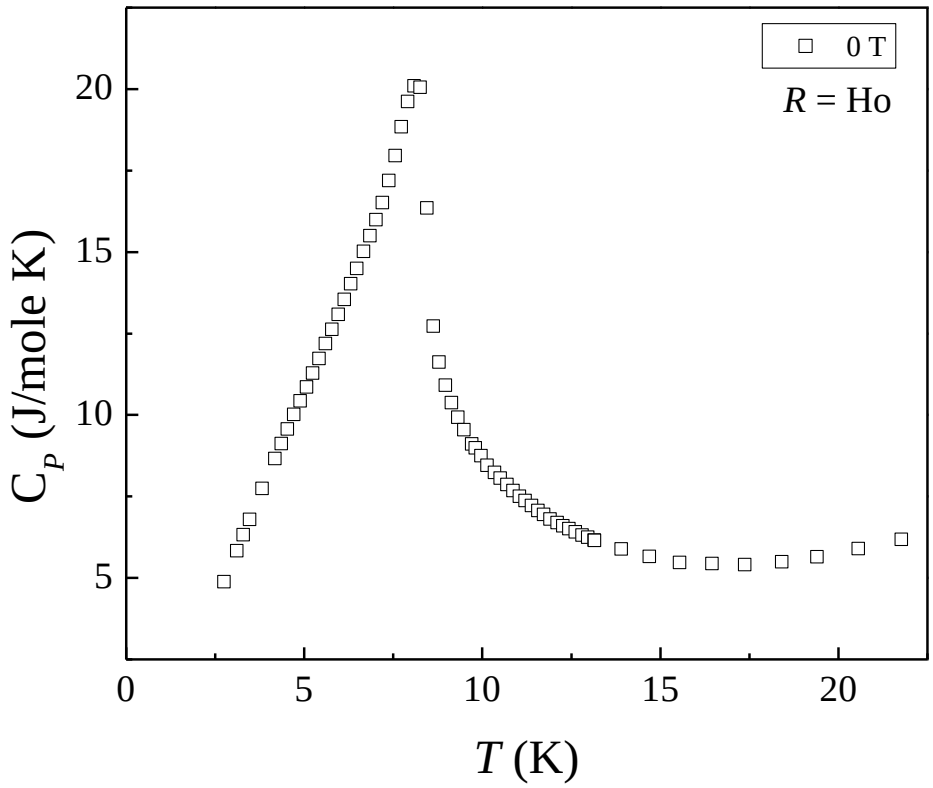

Figure 3.12: The zero-field cooled specific heat measured at zero field for $HoCr(BO_3)_2$.

$HoCr(BO_3)_2$ undergoes an AFM transition at this temperature. No data was taken under magnetic fields for this material.

Again, as the preliminary magnetic measurements have provided some details into the nature of the magnetic transition in $HoCr(BO_3)_2$,a NPD experiment was designed in order to characterize the magnetic ground state. The NPD pattern was first measured at 20 K for $HoCr(BO_3)_2$ with a wavelength of 1.5405 Å in order to study the lattice information as shown in Fig. 3.13. The refinements yielded lattice parameters a = 4.76002(6) Å and c =15.49239(32) Å and also revealed approximately 3% site disorder between the Ho and Cr sites. Moreover, a small amount of $HoBO_3$ impurity ($< 5\%$) was observed. Polycrystalline samples were measured above ($T \sim 20$ K) and below ($T \sim 2$ K) T_N as well as with applied fields up to μ_0H = 4.0 T at T = 1.5 K using a longer wavelength of 2.413 Å in order to study the magnetic structure information. The diffraction patterns and refinements can be seen in Fig. 3.14(a-c), and the results of the refinement are presented in Table 3.2.

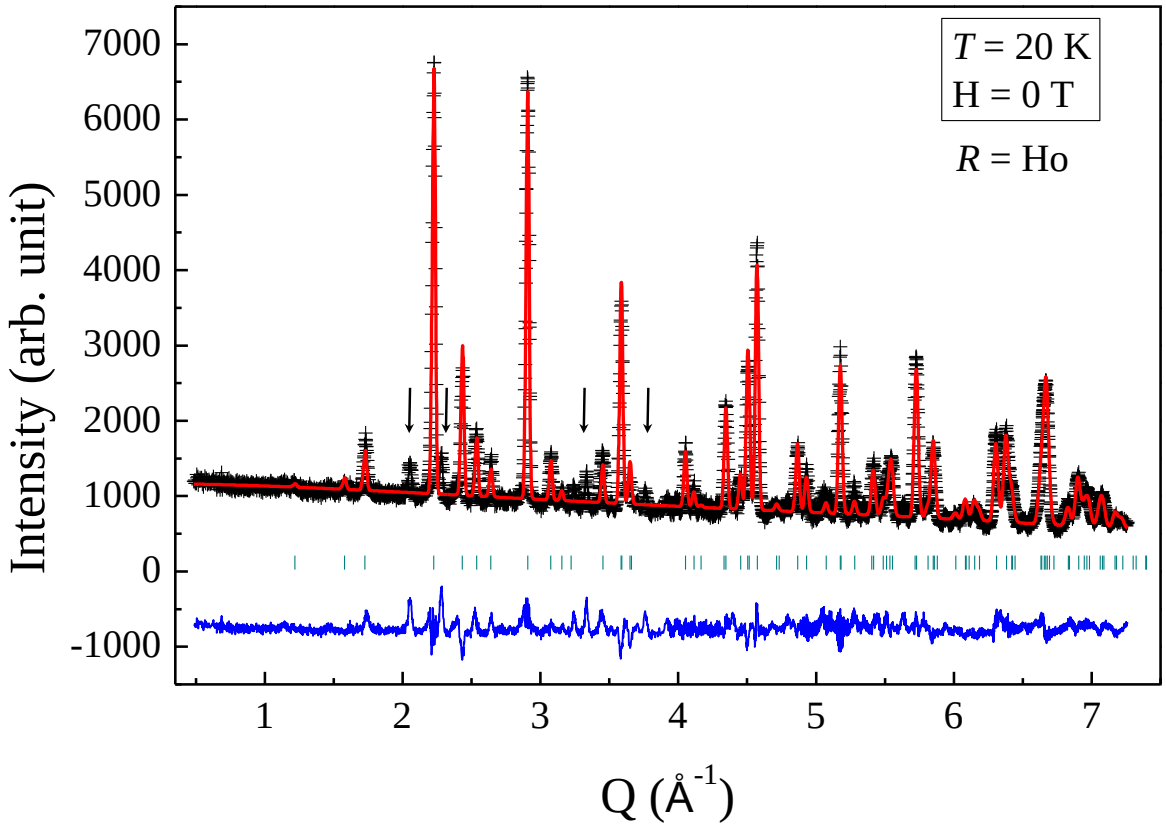

Figure 3.13: The elastic neutron diffraction patterns (crosses) for polycrystalline $HoCr(BO_3)_2$ at room temperature and zero field using a wavelength of 1.5405 Å. The solid curves are the best fits from the Rietveld refinements using *FullProf Suite*. The vertical marks indicate the position of Bragg reflections, and the bottom curves show the difference between the observed and calculated intensities. The arrows denote $HoBO_3$ impurity peaks.

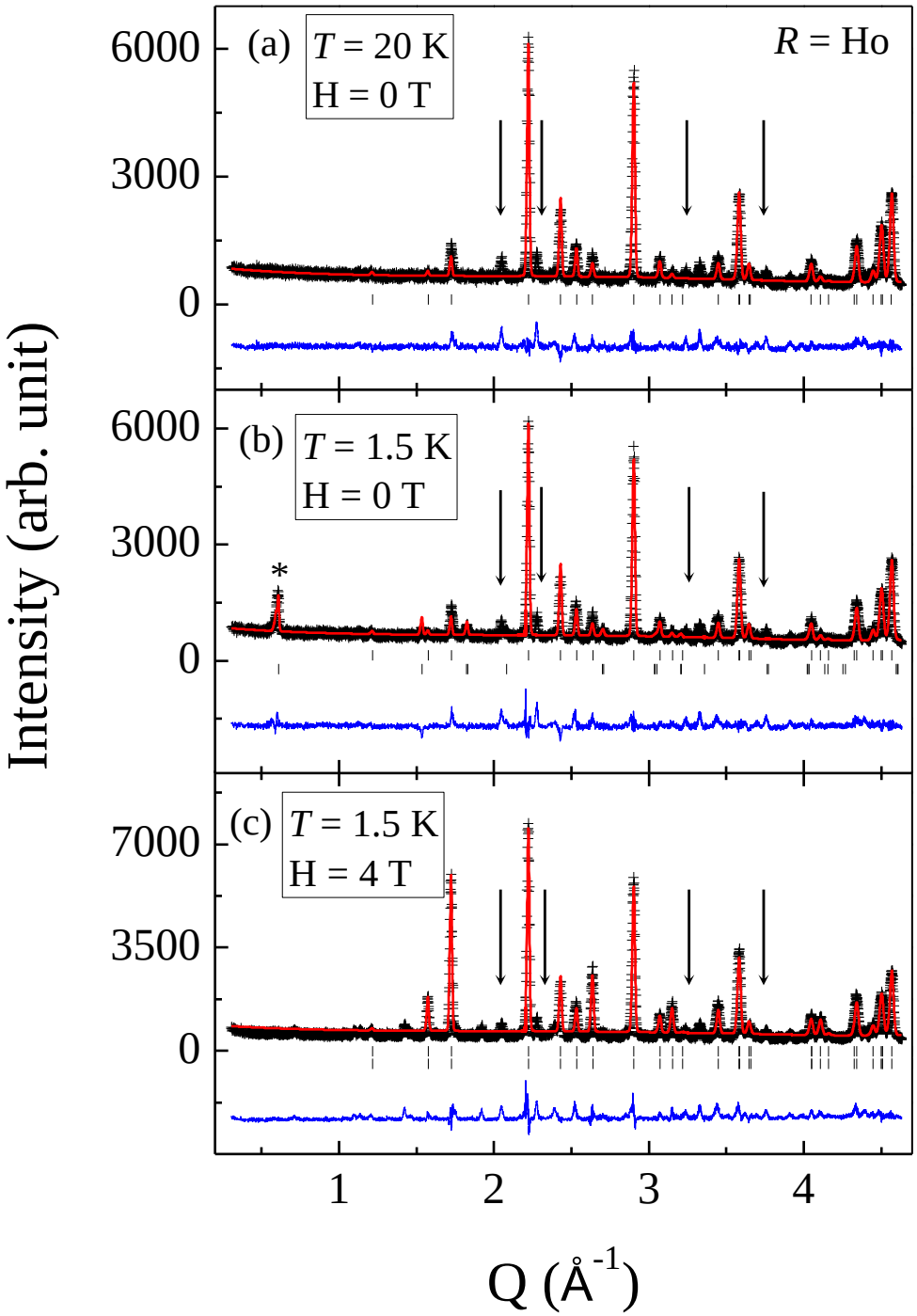

Figure 3.14: The neutron diffraction patterns for polycrystalline $HoCr(BO_3)_2$ (crosses) at (a) $T = 20$ K and $\mu_0 H = 0$ T, (b) $T = 1.5$ K and $\mu_0 H = 0$ T, and (c) $T = 1.5$ K and $\mu_0 H = 4.0$ T using a neutron wavelength of 2.413 Å. The solid curves are the best fits from the Rietveld refinements using *FullProf Suite*. The vertical marks indicate the position of Bragg reflections, and the bottom curves show the difference between the observed and calculated intensities. The * in (b) marks the location of the (0, 0, 3/2) reflection. The arrows denote $HoBO_3$ impurity peaks. This figure can be found in Ref. 115.

While $HoCr(BO_3)_2$ contains two magnetic ions (Cr^{3+}/Ho^{3+}), its magnetic structure at zero field is very similar to that of the Y-compound's. Below T_N with no applied field, the system is again described by a propagation vector of $\vec{k}$ = (0, 0, 3/2) (Fig. 3.14(b)). Analogously to the Y-compound, the refinement shows that for $HoCr(BO_3)_2$, the Cr^{3+} spins arrange ferromagnetically with a canting angle of 37.5° away from the *ab*-plane while the Cr^{3+} layers align antiferromagnetically (Fig. 3.15(c)). This canting angle is slightly larger than that of the Y-compound. Here, no evidence was observed to support the magnetic ordering of the Ho^{3+} spins down to 2 K at zero field. The total refined magnetic moment of μ_{Cr} = 3.07(13) μ_B supports this conclusion as the moment size is close to the theoretical value for Cr^{3+} ions.

Major magnetic Bragg reflections of $HoCr(BO_3)_2$ were also investigated. As shown in Fig. 3.15(a), the intensities of the (0, 0, 3/2) and the (1, 0, -1/2), (1, -1, 1/2), and (0, 1, 1/2) reflections are suppressed above T_N = 9 K. Meanwhile at 2 K, the intensity of the (0, 0, 3/2) reflection is suppressed above H_C = 2.0 T while the intensity of the (1, 0, 1) reflection increases linearly with increasing field. These critical values agree with our previous susceptibility measurements.

From Fig. 3.14(c) we can see that the lattice Bragg peaks and magnetic Bragg peaks align exactly for $HoCr(BO_3)_2$ at 2 K and under 4.0 T. This suggests that the system enters a FM ground state above H_C similar to the Y-compound. However, the refinement of this data reveals that both the Cr^{3+} and the Ho^{3+} spins order now. The obtained spin structure at 2 K and under 4.0 T is shown in Fig. 3.15(d) in which both the Ho^{3+} and Cr^{3+} spins are arranged ferromagnetically in the *ab*-plane, but the Cr^{3+} spins have a canting angle of 69.8° away from the *ab*-plane while the Ho^{3+} ions have a canting angle of 80.8° away from the *ab*-plane. The total refined magnetic moment of 10.35(44) μ_B also supports the fact that now both the Cr^{3+} and the Ho^{3+} spins order and contribute to the value of the total magnetic moment. This value also matches closely with the saturation value determined from the magnetization curve as well as the effective magnetic moment derived from our $1/\chi$ data.

Due to the complexity associated with the addition of a second magnetic ion, no INS data was measured for $HoCr(BO_3)_2$. Because the two magnetic ground states are similar in

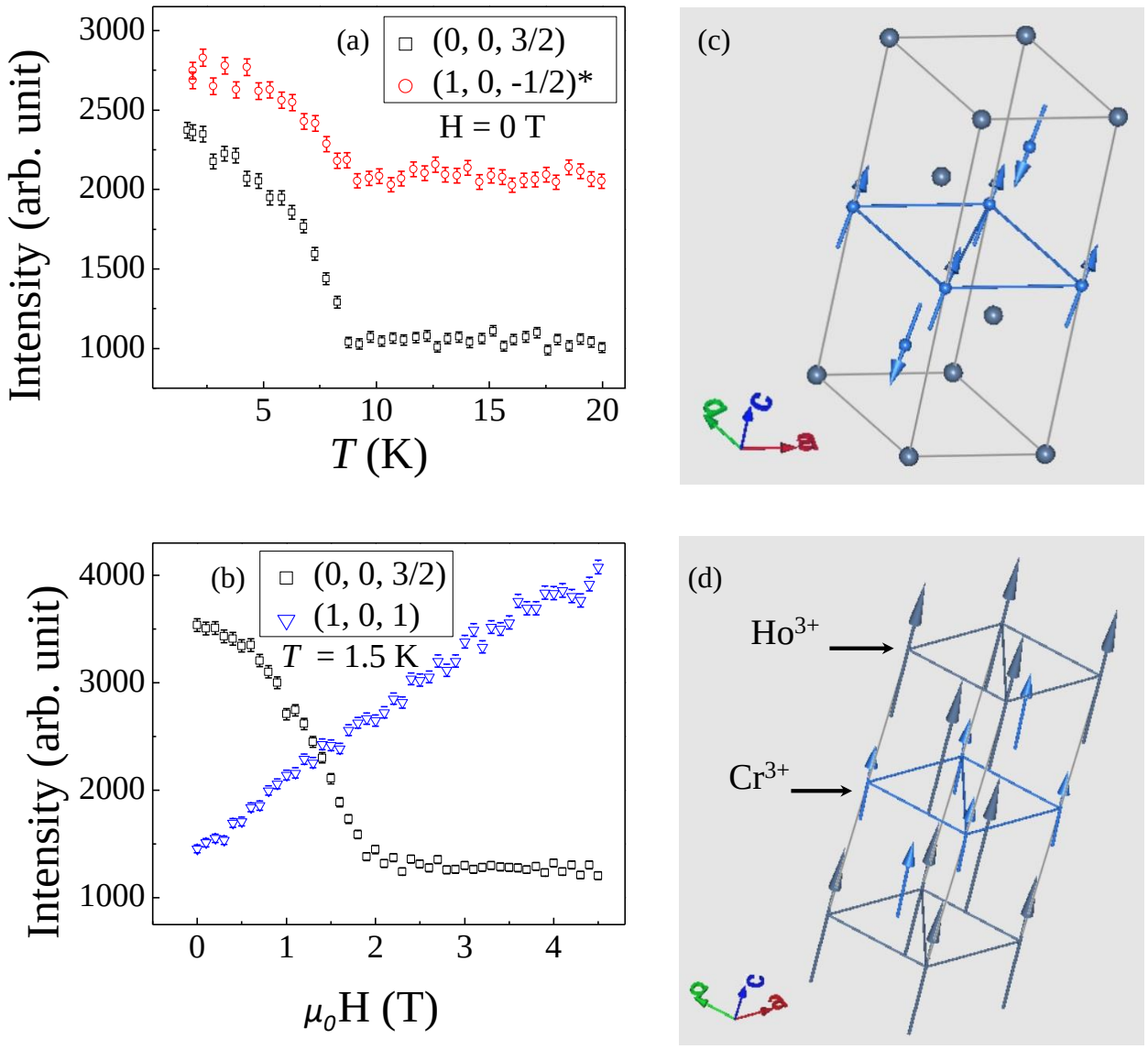

Figure 3.15: For $HoCr(BO_3)_2$, (a) the temperature dependence and (b) the field dependence of certain magnetic and lattice Bragg reflections, and the magnetic ground state at (c) $\mu_0 H = 0$ T and (d) $\mu_0 H = 4.0$ T. *Note that the reflection marked (1, 0, -1/2) in (a) also includes intensity from the (1, -1, 1/2) and (0, 1, 1/2) reflections. This figure can be found in Ref. 115.

nature, it is expected that the exchange interactions found under zero field would be very similar to the Y-compound's.

Finally, possible magnetoelectric phenomena in $HoCr(BO_3)_2$ were investigated using electric polarization and dielectric constant measurements. The capacitance was measured on thin-plate polycrystalline samples with an Andeen-Hagerling AH-2700A commercial capacitance bridge using a frequency of 20 kHz which was analyzed to obtain the dielectric constant data by approximating the sample as an infinite parallel capacitor. The pyroelectric current was measured using a Keithley 6517A electrometer during warming after the sample was cooled in an electric field from above T_N.

The magnetic field dependence of ϵ for $HoCr(BO_3)_2$ is presented in Fig. 3.16(a). At temperatures lower than its T_N, ϵ increases sharply at low fields and then saturates into a broad feature around $\mu_0 H = 1.5$ T. Similar to the Y-compound, above its transition temperature, such behavior disappears. The temperature dependence of ϵ for $HoCr(BO_3)_2$ exhibits a more drastic response as shown in Fig. 3.16(b). First, a broad feature around $T = 4$ K is observed at zero field. As the field increases, this shoulder feature becomes suppressed and vanishes near $\mu_0 H = 1.0$ T. Meanwhile, a sharp peak appears near $T = 7$ K which increases in relation to the field up to $\mu_0 H = 1.0$ T at which point it begins to weaken with increasing field. Furthermore, the critical temperature associated with the sharp peak decreases with increasing field.

The anomalies observed from ϵ for both the Ho-compound and the Y-compound are all observed around their magnetic ordering temperatures or critical fields for spin state transitions; therefore, both systems exhibit some degree of magnetodielectric (MD) coupling. Furthermore, the replacement of the non-magnetic Y^{3+} ion with the magnetic Ho^{3+} ion affects this coupling which leads to stronger MD phenomena as revealed by the sharp peak around T_N in the field induced ϵ data. It is also worth noting that the Ho-compound shows little response at zero field near T_N in stark contrast to the Y-compound. Thus the MD phenomena are likely related to different mechanisms for each sample, such as spin-phonon coupling or magnetostriction.

While $HoCr(BO_3)_2$ was studied via pyroelectric current measurements at different magnetic fields, no electric polarization was observed for bulk polycrystalline samples around

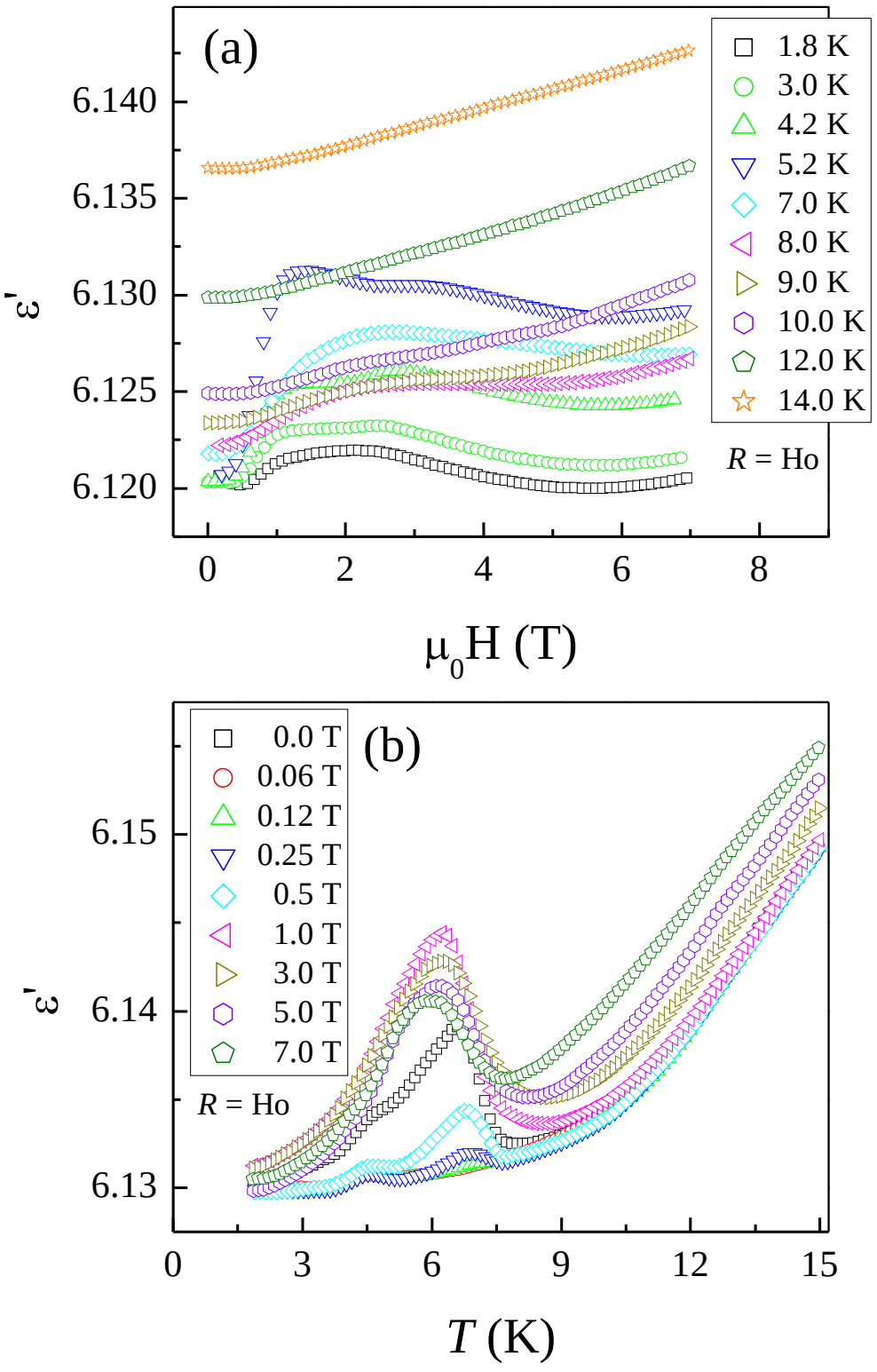

Figure 3.16: For $HoCr(BO_3)_2$, (a) the field dependence of the dielectric constant measured at 20 kHz at varying temperatures, and (b) the temperature dependence of the dielectric constant measured at 20 kHz under applied fields. This figure can be found in Ref. 115.

the transition temperatures. Similar to the Y-compound, it is possible that a single crystal sample could produce an anisotropic polarization which is hidden by the powder averaging of the results or that the system is already ordered in an antiferroelectric state. Again, further experiments may be necessary to elucidate the matter.

3.3 Discussion

After several enlightening characterization experiments, it is clear that $YCr(BO_3)_2$ and $HoCr(BO_3)_2$ share several characteristics of their magnetic properties. The Cr^{3+} spins of both samples enter a canted AFM state below $T_N \sim 9$ K at zero field. With applied field above a critical value of $H_C \sim 2.0$ to 2.5 T, the antiferromagnetic arrangement of the Cr^{3+} spins along the c-axis is flipped to become ferromagnetic for both samples. The major difference here is that for the Ho-compound, both the Ho^{3+} and the Cr^{3+} spins order ferromagnetically when $\mu_0 H > H_C$. This canted AFM state at zero field with spins aligning ferromagnetically in the ab-plane and antiferromagnetically along the c-axis of $YCr(BO_3)_2$ is consistent with the fact that its intralayer interaction is ferromagnetic and its interlayer interaction is antiferromagnetic which was revealed by the spin wave spectrum simulation.

Furthermore, by analyzing the zero field magnetic structure information obtained from the neutron diffraction data combined with the previously determined structural information for both samples, we were able to obtain two possible magnetic space groups, $R_I\bar{3}$ and $P_S\bar{1}$, using the Bilbao Crystallographic Server. [124, 125, 126, 127] While the $P_S\bar{1}$ magnetic space group allows for the magnetic moment to freely align along any direction, $R_I\bar{3}$ completely restricts the magnetic moment to the c-axis. Moreover, the Rietveld refinements of the system reveal that the existence of the intense (0, 0, 3/2) peak depends upon having a magnetic moment in the ab-plane. Therefore, our data strongly suggests that the system is best described by the $P_S\bar{1}$ magnetic space group.

To understand why the intralayer interaction of the Y-compound is ferromagnetic we look into the superexchange interactions involving the Cr^{3+} ions. In order to qualitatively discuss the sign (FM or AFM) of the superexchange interactions, we turn to Kanamori theory. For a magnetic cation on an octahedral site, Kanamari has shown that the superexchange

interaction via nonmagnetic anion is closely connected with the orbital states of the cation and anion.[128] In $YCr(BO_3)_2$, two superexchange pathways for the Cr^{3+} spins in the same layer are available as the CrO_6 octahedrons are connected by YO_6 octahedrons with corner sharing oxygens. As shown in Fig. 3.17(a), the first is Cr^{3+}-O^{2-}-O^{2-}-Cr^{3+} and the second is Cr^{3+}-O^{2-}-Y^{3+}-O^{2-}-Cr^{3+}. As observed from other magnetic oxides, the Cr^{3+}-O^{2-}-O^{2-}- Cr^{3+} pathway's superexchange interaction is often AFM. Meanwhile, one possible situation for the Cr^{3+}-O^{2-}-Y^{3+}-O^{2-}-Cr^{3+} exchange path is shown in Fig. 3.17(b).

Here we consider the superexchange interaction between the spins on the dxy orbitals of the Cr^{3+} ions. In the Cr^{3+} ions' frame of reference, the d_{xy} orbitals are centered 45° from both the x-axis and the y-axis. Through our Rietveld refinements of the neutron diffraction pattern, we determined that the Cr^{3+}-O^{2-}-Y^{3+} bond angle is 123.67(9)° and the O^{2-}-Y^{3+}-O^{2-} bond angle is 88.79(9)°, very close to 90°; therefore, the d_{xy} orbitals are centered $\sim 10^{\circ}$ from the line where the O^{2-} and the Y^{3+} ions are situated which allows for the necessary hybridization to occur between the d_{xy} and the p_x and p_y orbitals. In this configuration, the spin 1 on the left Cr^{3+} ion is transferred to the molecular orbital composed of the p_y orbitals of the O^{2-} $2p$ orbitals and the Y^{3+} $4p$ orbitals (the filled outermost orbitals), and the spin 2 on the right Cr^{3+} ion is transferred to the molecular orbital composed of the p_x orbitals of the O^{2-} and Y^{3+} ions. Due to Hund's rules, these two spins on the p_y and p_x orbitals in the Y^{3+} ions have to be parallel. Then, after these two spins are transferred back to the Cr^{3+} ion, a FM superexchange interaction is built. For $YCr(BO_3)_2$, it is reasonable to assume that this FM interaction overcomes the AFM interaction leading to the FM spin arrangements in the ab-plane.

In several other TLAF systems with layered perovskite structures, similar FM superexchange interactions involving $3d$-$2p$-$4p$ (or $3p$)-$2p$-$3d$ paths have been reported. For example, in $Ba_3CoNb_2O_9$,[129] a weak AFM interaction is the result of the FM Co^{2+}-O^{2-}-Nb^{5+}-O^{2-}-Co^{2+} superexchange interaction involving the Nb^{5+} $4p$ orbitals competing with the AFM Co^{2+}-O^{2-}-O^{2-}-Co^{2+} interaction. Accordingly, this system exhibits a small saturation field and a low AFM transition temperature. In another triangular lattice magnet, $AAg_2M(VO_4)_2$ (A = Ba, Sr; M = Co, Ni),[130] the FM Co^{2+}-O^{2-}-V^{5+}-O^{2-}-Co^{2+} interaction involving the V^{5+} $3p$ orbitals is stronger than the AFM Co^{2+}-O^{2-}-O^{2-}-Co^{2+} interaction resulting in a FM

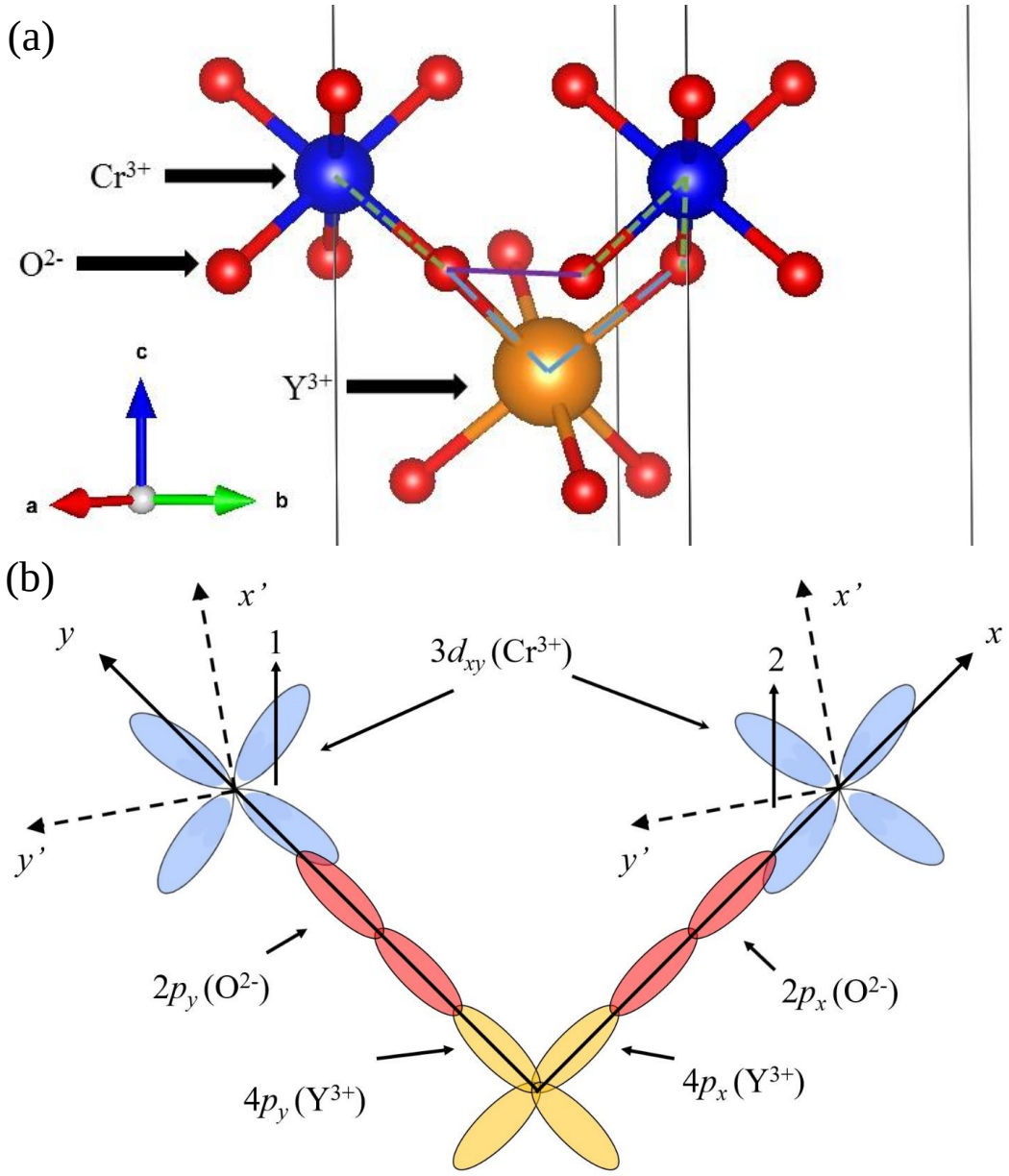

Figure 3.17: (a) The lattice view of the Cr^{3+}-O^{2-}-O^{2-}-Cr^{3+} and the Cr^{3+}-O^{2-}-Y^{3+}-O^{2-}-Cr^{3+} superexchange paths; (b) the orbital configurations related to the Cr^{3+}-O^{2-}-Y^{3+}-O^{2-}-Cr^{3+} superexchange path. The Cr^{3+} ions' frame of reference is denoted with primes. The angle between the unprimed and primed axes is 55°. This figure can be found in Ref. 115.

transition. One important note here for $YCr(BO_3)_2$ is that although the FM interaction overcomes the AFM interaction in the *ab*-plane, the AFM interlayer interaction still leads to an AFM arrangement of spins along the *c*-axis to stabilize the canted AFM spin structure. This interlayer interaction is weaker, but it plays an important role in defining the magnetic ground state.

From a magnetodielectric perspective, both $YCr(BO_3)_2$ and $HoCr(BO_3)_2$ exhibit some MD behaviors. The Y-compound's dielectric constant shows a slope change around T_N and a sharp peak around H_C; on the other hand, the Ho-compound's dielectric constant shows a strong peak around T_N with an applied field and a broad peak around H_C. Apparently, this difference is related to the presence of the second magnetic ion, Ho^{3+}, in $HoCr(BO_3)_2$. It is also worth noting that the MD behavior observed in the R = Y sample occurs near the transition temperature at zero field while the R = Ho sample's MD behavior seems to depend on an applied magnetic field. Therefore, it is likely that the mechanisms behind this behavior in both samples are different.

To explain the MD anomalies, we first examined a possible linear magnetoelectric effect. For our system, both possible magnetic space groups, $R_I\bar{3}$ and $P_S\bar{1}$, contain an inversion center as one of their symmetry elements. Additionally, symmetry operators in both magnetic space groups do not break time reversal symmetry. Therefore, the linear ME effect is excluded by symmetry.

We also observed that the cusp-shape of the Y-compound's MD anomaly is similar to behavior observed in the AFM $EuTiO_3$.[131, 132] In $EuTiO_3$, the pair correlation of the Eu spins to a soft-phonon mode containing Eu-O stretching motions was ascribed to the MD anomaly. Such spin-phonon coupling was also attributed to the MD anomaly observed in a ferrimagnetic spinel Mn_3O_4.[133] On the other hand, it is also possible that the higher order, symmetry independent ME terms can be relevant as in the case for $TeCuO_3$[134] and in $Cr[(H_3N\text{-}(CH_2)_2\text{-}PO_3(Cl)(H_2O)]$.[135, 136]

Another way to understand the differences between the MD effect in both samples is to consider magnetostriction. As the order of magnitude of the effect is fairly large ($\sim 10^{-3}$), we speculate that the differences in the dielectric constant data are more likely due to the magnetostriction caused by the extra exchange interaction between the Cr^{3+} and Ho^{3+} layers

with an applied field rather than due to the change of the lattice parameters which typically produces a much smaller anomaly ($10^{-5} \sim 10^{-6}$). Specifically, (i) at zero field, there is no exchange interaction between the Cr^{3+} and Ho^{3+} spins in $HoCr(BO_3)_2$ since only the Cr^{3+} spins order. Therefore, there is no obvious dielectric anomaly around T_N; (ii) with an applied field $\mu_0 H < H_C$, the short range ordering of Ho^{3+} spins could be induced which can lead to an AFM exchange interaction between the Cr^{3+} and Ho^{3+} layers and results in magnetostriction. Thus, a small magnetic field such as 0.25 T induces a dielectric constant peak around T_N. Moreover, with increasing field this effect is strengthened by involving more short range ordered Ho^{3+} spins, and, consequently, the dielectric constant peak intensity increases; (iii) with even larger applied fields $\mu_0 H > H_C$, the Ho^{3+} spins order ferromagnetically along with the Cr^{3+} spins. This new spin structure possibly leads to weak magnetostriction compared to that of $\mu_0 H < H_C$. Therefore, the dielectric constant peak intensity achieves the highest value with $\mu_0 H = 1.0$ T and then decreases with increasing field as soon as it exceeds H_C, such as 3.0 T.

In any case, more studies are needed to determine the origin of the observed MD anomaly in both compounds. Experimental probes such as infrared and Raman spectroscopy could reveal possible spin-phonon coupling. Furthermore, dielectric constant and polarization (pyroelectric current) measurements on single crystal samples can be helpful not only to identify the ME coefficients for both compounds but also to study the possible magnetostriction effect for the Ho-compound.

3.4 Conclusions

In summary, we report detailed experimental studies of the layered perovskites $R Cr(BO_3)_2$ (R = Y and Ho) with triangular lattices, focusing on their magnetic and electric properties. We observed the presence of a canted AFM state in both samples at zero field for the Cr^{3+} spins as well as a FM state while a critical field was applied. More interestingly, in comparison to the Y-compound, far different MD behaviors were observed in the Ho-compound which should be due to the interplay between the Cr and Ho magnetic layers. Our studies here demonstrate that the combination of layered structures with two different magnetic ions and

triangular lattices can produce intriguing physical properties. This principle of materials engineering can help us to design and explore more complex magnetic materials.

Chapter 4

Mo Cluster Magnets $Li_2In_{1-x}Sc_xMo_3O_8$ and $(Mg,Zn)ScMo_3O_8$

In the previous chapter, the combination of a triangular lattice and multiple magnetic ions was investigated. Now, the focus will shift to triangular lattice cluster magnets. In particular, we studied two Mo cluster families, $Li_2In_{1-x}Sc_xMo_3O_8$ and $(Mg,Zn)ScMo_3O_8$. Both families exhibited intriguing magnetic properties ranging from an ordered FM state to a possible QSL state. Some of the results of this chapter have been published in Ref. 148.

4.1 Introduction

Recently, the years of studying geometrically frustrated materials has inspired pioneering research on so-called cluster magnets, systems composed of several ions with overlapping molecular orbitals. Several cluster magnets exhibiting novel magnetic properties have been investigated previously.[137, 138, 139, 140, 142, 141, 143, 144] It is possible that a system containing both a frustrated lattice and cluster magnets could lead to a new frontier of research regarding frustrated magnetism.

One particularly promising family of compounds which appear to meet the above criteria is composed of triangular lattice Mo cluster compounds. This family includes the compound

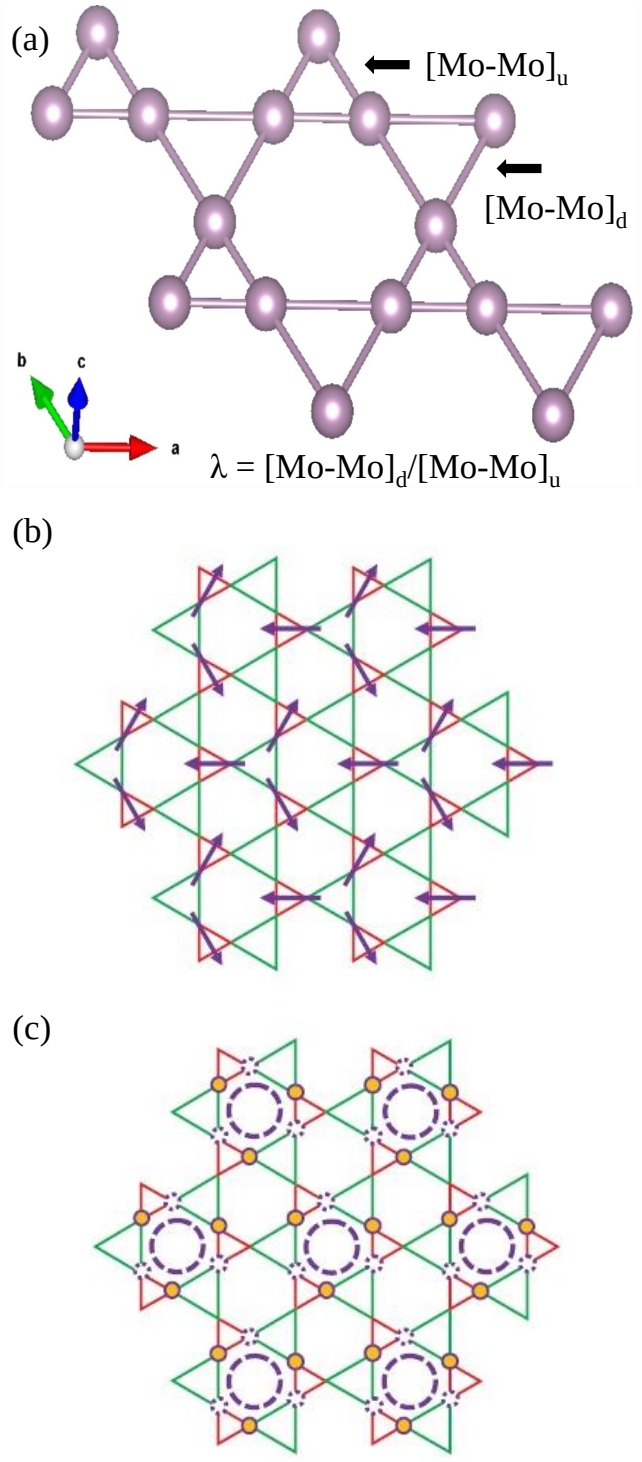

Figure 4.1: (a) The smaller up-triangles and larger down-triangles in the "breathing" Kagome lattice formed by the Mo atoms in the *ab*-plane. The Mo-Mo bond lengths as well as the breathing parameter λ are included. (b) Type-I cluster Mott insulator. (c) Type-II cluster Mott insulator.

$LiZn_2Mo_3O_8$, a well-studied material containing two distinct Curie-Weiss regimes and a possible QSL ground state.[142, 143, 144, 145, 146, 147, 148] This material contains $[Mo_3]^{11+}$ clusters with seven $4d$ electrons which result in one unpaired electron per cluster and is thus an effective $S = 1/2$ system. Moreover, the Mo ions form a "breathing" Kagome lattice[149, 150, 151] in the ab-plane composed of slightly larger down-triangles and slightly smaller up-triangles as shown in Fig. 4.1(a). This asymmetry can be used to define the breathing parameter λ for the system:

$$\lambda = [Mo - Mo]_d / [Mo - Mo]_u, \tag{4.1}$$

where $[Mo - Mo]_d$ and $[Mo - Mo]_u$ are the Mo bond lengths of the down-triangles and up-triangles, respectively.

Currently, there are two hypotheses as to how the electrons behave in these Mo_3O_{13} clusters. First, it has been proposed that each unpaired electron is delocalized over an up-triangle which leads to a $S = 1/2$ triangular lattice as shown in Fig. 4.1(b).[142, 146] This behavior, dubbed the Type-I cluster Mott insulator,[148] is expected to occur when λ is large. Alternatively, due to the large spatial extent of the $4d$ electrons, there is a non-zero probability of tunneling between adjacent clusters, so when λ is small, this gives rise to the long range plaquette charge order (PCO), dubbed the Type-II cluster Mott insulator, as shown in Fig. 4.1(c).[148] In order to test these models, more Mo cluster materials will need to be investigated.

To this end, we studied two separate Mo cluster compounds: $Li_2In_{1-x}Sc_xMo_3O_8$ (x = 0, 0.2, 0.4, 0.6, 0.8, and 1.0) and (Mg,Zn)$ScMo_3O_8$. For $Li_2In_{1-x}Sc_xMo_3O_8$, both ends of the doping study have been previously investigated. It was found that $Li_2InMo_3O_8$ adopts a 120 degree AFM ground state,[152, 153] while $Li_2ScMo_3O_8$ was shown not to order down to 4.2 K according to ^{7}Li nuclear magnetic resonance measurements making it another potential QSL candidate.[153, 154] Thus we probed the tunability of the spin and charge degrees of freedom in the system by doping $Li_2InMo_3O_8$ with Sc ions on the In-site. For (Mg,Zn)$ScMoO_3O_8$, the physical properties of $ZnScMo_3O_8$ have been reported previously,[154] but no in-depth magnetic or electric studies have been performed for

either sample. Therefore, we characterized both compounds using XRD pattern analysis as well as ac and dc magnetic susceptibility, specific heat, and resistivity measurements. Additionally, time-differential and longitudinal-field μSR measurements were performed on the $Li_2In_{1-x}Sc_xMo_3O_8$ samples as discussed in Sec. 2.7.[155] Our results are consistent with the previous reports and suggest many similarities between these materials and the other studied Mo_3 cluster compounds while also introducing new and exciting physics.

4.2 Synthesis and Characterization

4.2.1 $Li_2In_{1-x}Sc_xMo_3O_8$

Polycrystalline samples of $Li_2In_{1-x}Sc_xMo_3O_8$ (x = 0.0, 0.2, 0.4, 0.6, 0.8, and 1.0) were synthesized as described in Ch. 2.1. The purity of the samples as well as the elementary structural properties were then probed via XRD measurements. Every sample crystallized into the $P6_3mc$ space group analogously to the parent compounds. As such, their crystal structures are composed of hexagonal-close-packed Oxygen layers with an abac stacking sequence along [0 0 1]. These are held together by alternating Li-In and Mo layers where the Li^+ and the In^{3+} ions occupy tetrahedral and octahedral sites, respectively, in the ratio 2:1, and the Mo atoms occupy octahedral sites, forming strongly bonded triangular clusters as shown in Figure 4.2(a). Each cluster consists of three MoO_6 octahedra which are shared along two edges to form the Mo_3O_{13} cluster.

The structures were determined using the Rietveld refinement method, and the results for the $x = 0.6$ XRD pattern are shown in Fig. 4.2(b). Additionally, the results for the $x = 0.6$ and $x = 1.0$ samples' XRD fittings are shown in Table 4.1. No obvious impurities appear in the data. Additionally, Fig. 4.2(c) shows the standard linear relationship expected as the larger In^{3+} ions are replaced with smaller Sc^{3+} ions. The preliminary XRD measurements suggest that no macroscopic structural changes are present in any of the doped samples at room temperature.

In Fig. 4.3(a), we show the temperature dependence of the dc magnetic susceptibility measured at μ_0H = 2 T for $Li_2In_{1-x}Sc_xMo_3O_8$. As previously stated, the $x = 0$ sample

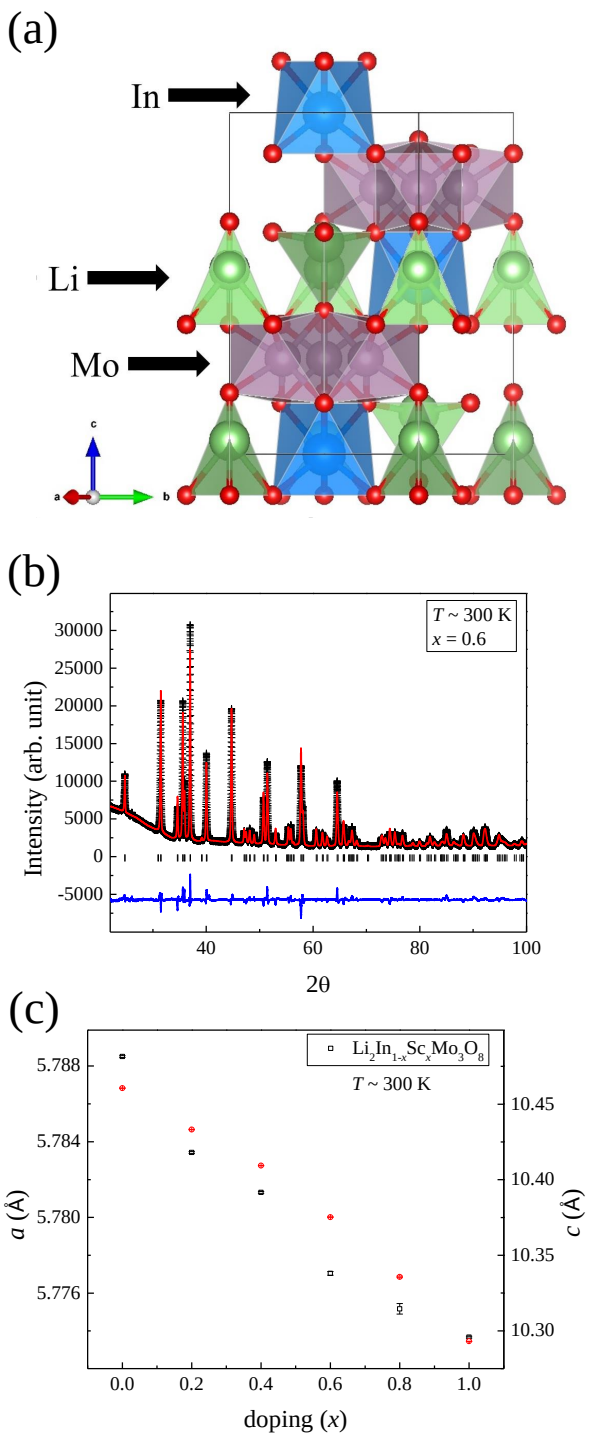

Figure 4.2: (a) The hexagonal $P6_3mc$ crystal structure of $Li_2InMo_3O_8$. (b) The XRD pattern (crosses) for polycrystalline $Li_2In_{0.4}Sc_{0.6}Mo_3O_8$ at room temperature and zero field. The solid curves are the best fits from the Rietveld refinements using *FullProf Suite*. The vertical marks indicate the position of Bragg reflections, and the bottom curves show the difference between the observed and calculated intensities. (c) The Sc doping dependence of the lattice parameters measured at room temperature.

Table 4.1: Structural parameters at room temperature (space group $P6_3mc$) for (a) $Li_2ScMo_3O_8$ and (b) $Li_2In_{0.4}Sc_{0.6}Mo_3O_8$ determined from refined XRD measurements.

Refinement	Atom	Site	x	y	z	Occupancy
(a) $Li_2ScMo_3O_8$ $\chi^2 = 1.29$	Li1	2a	0	0	0.198(27)	0.167
	Li2	2b	1/3	2/3	0.096(27)	0.167
	Sc	2b	1/3	2/3	0.753(27)	0.167
	Mo	6c	0.18644(4)	0.81356(4)	0.468(27)	0.500
	O1	2a	0	0	0.074(27)	0.167
	O2	2b	1/3	2/3	0.316(27)	0.167
	O3	6c	0.51777(33)	0.48223(33)	0.104(27)	0.500
	O4	6c	0.84135(46)	0.15865(46)	0.354(27)	0.500
			$a = b = 5.77116(5)$ Å, $c = 10.28917(15)$ Å			
			Overall B-factor = 1.796(17) Å^2			
(b) $Li_2In_{0.4}Sc_{0.6}Mo_3O_8$ $\chi^2 = 1.77$	Li1	2a	0	0	0.175(45)	0.167
	Li2	2b	1/3	2/3	0.114(45)	0.167
	In	2b	1/3	2/3	0.741(45)	0.0692(26)
	Sc	2b	1/3	2/3	0.741(45)	0.0975(26)
	Mo	6c	0.18595(5)	0.81405(5)	0.458(45)	0.500
	O1	2a	0	0	0.064(45)	0.167
	O2	2b	1/3	2/3	0.303(45)	0.167
	O3	6c	0.51823(37)	0.48177(37)	0.098(45)	0.500
	O4	6c	0.84117(57)	0.15883(57)	0.344(45)	0.500
			$a = b = 5.77034(35)$ Å, $c = 10.35095(63)$ Å			
			Overall B-factor = 1.135(16) Å^2			

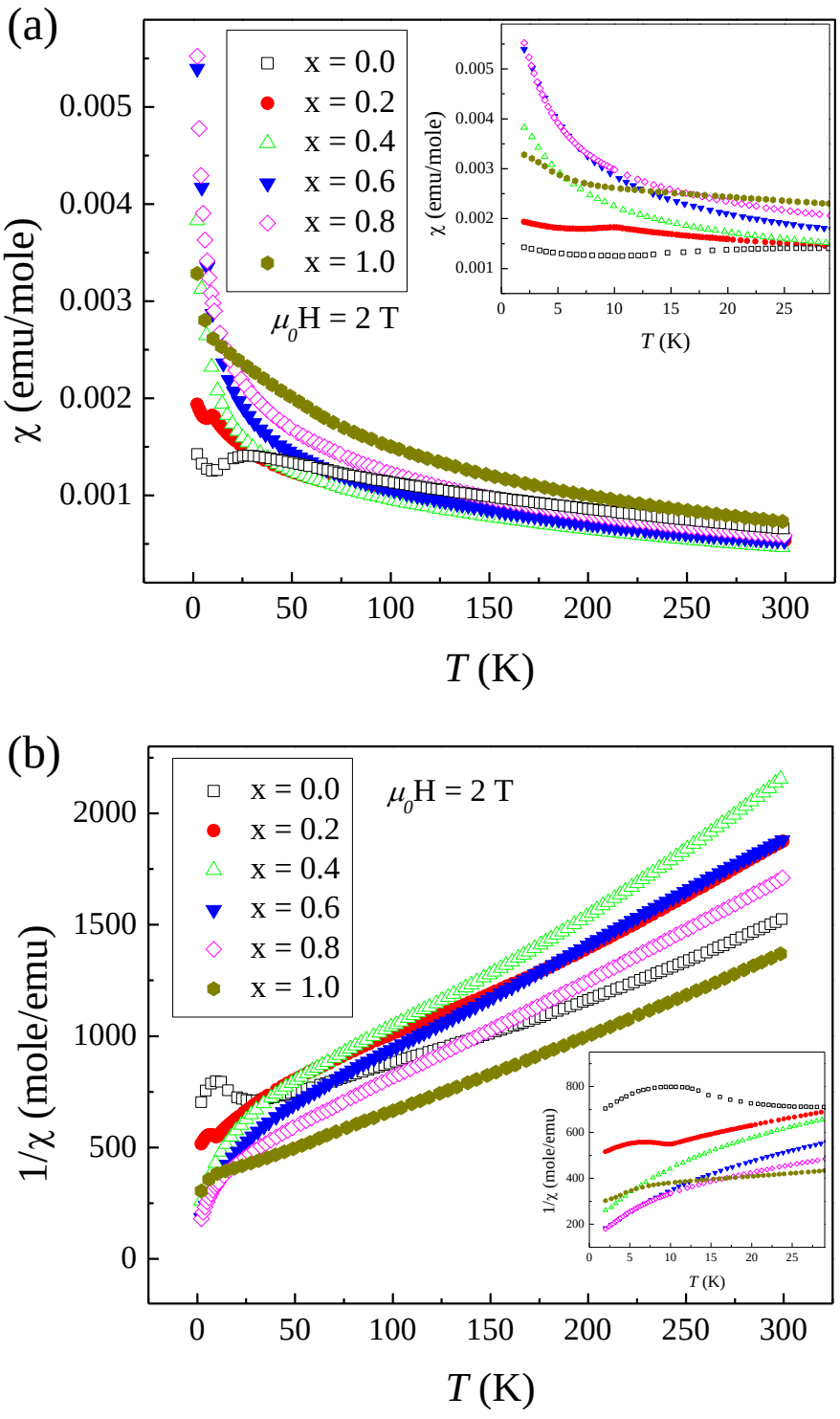

Figure 4.3: For $Li_2In_{1-x}Sc_xMo_3O_8$, (a) the temperature dependence of the dc susceptibility measured at 2 T. The inset shows a zoomed-in region of the dc susceptibility. (b) The temperature dependence of the inverse dc susceptibility measured at 2 T. The inset shows a zoomed-in region of the inverse dc susceptibility.

Table 4.2: Calculated Curie-Weiss constants for $Li_2In_{1-x}Sc_xMo_3O_8$ at varying temperatures.

$Li_2In_{1-x}Sc_xMo_3O_8$	Sc doping (x)	θ_{CW1} (K)	μ_{eff1} (μ_B)	θ_{CW2} (K)	μ_{eff2} (μ_B)	C_2/C_1
CW Fit 1: T = 96 - 300 K	0.0	-166.7	1.58	-	-	-
	0.2	-126.4	1.36	-	-	-
	0.4	-81.8	1.20	-9.27	0.58	0.236551
CW Fit 2: T = 2 - 10 K	0.6	-96.7	1.30	-6.83	0.61	0.236551
	0.8	-80.4	1.34	-8.07	0.65	0.236551
	1.0	-84.8	1.50	-	-	-

shows a feature near 25 K which indicates the samples transition to the 120° structure. The $x = 0.2$ sample exhibits very similar behavior to the $x = 0$ sample. However, by exchanging 40-80% of the In atoms with Sc, the magnetic order is suppressed–one feature we expect a QSL to display. Finally, the $x = 1.0$ sample shows a clear slope change near 10 K which suggests some short-range ordering.

For the samples with suppressed order, the inverse susceptibility, illustrated in Fig. 4.3(b), revealed two separate regions of interest. Thus for these three samples, two temperature regions were analyzed by Curie-Weiss fits as shown in Fig. 4.4(a-f). The results of this analysis are found in Table 4 4.2. For the fits from 96 - 300 K, the values of μ_{eff} vary from roughly 1.2-1.6 μ_B. The deviation from the expected value for a $S = 1/2$ system for the samples in the QSL regime is likely due to spin-orbit coupling effects. Additionally, all of the negative θ_{CW} values suggest that the dominant magnetic interactions are AFM in the Mo clusters. The CW fits from 2 - 10 K show values which are less than half of the high temperature fits for μ_{eff}, indicating a possible placquette charge ordering ground state.[156] This idea is explored further in Section 4.3.

The molar specific heat capacity was measured for each sample under zero field as shown in Fig. 4.5(a). Similar to the dc susceptibility results, the measurements indicate an AFM transition for the $x = 0$ sample, show a small kink for the $x = 0.2$ sample and a broad feature for the $x = 1.0$ sample, but no features associated with a magnetic transition are observed for the $x = 0.4$, 0.6, and 0.8 samples. Additionally, nonmagnetic $Zn_2Mo_3O_8$ was measured in order to investigate the lattice contribution to the specific heat. This contribution, illustrated

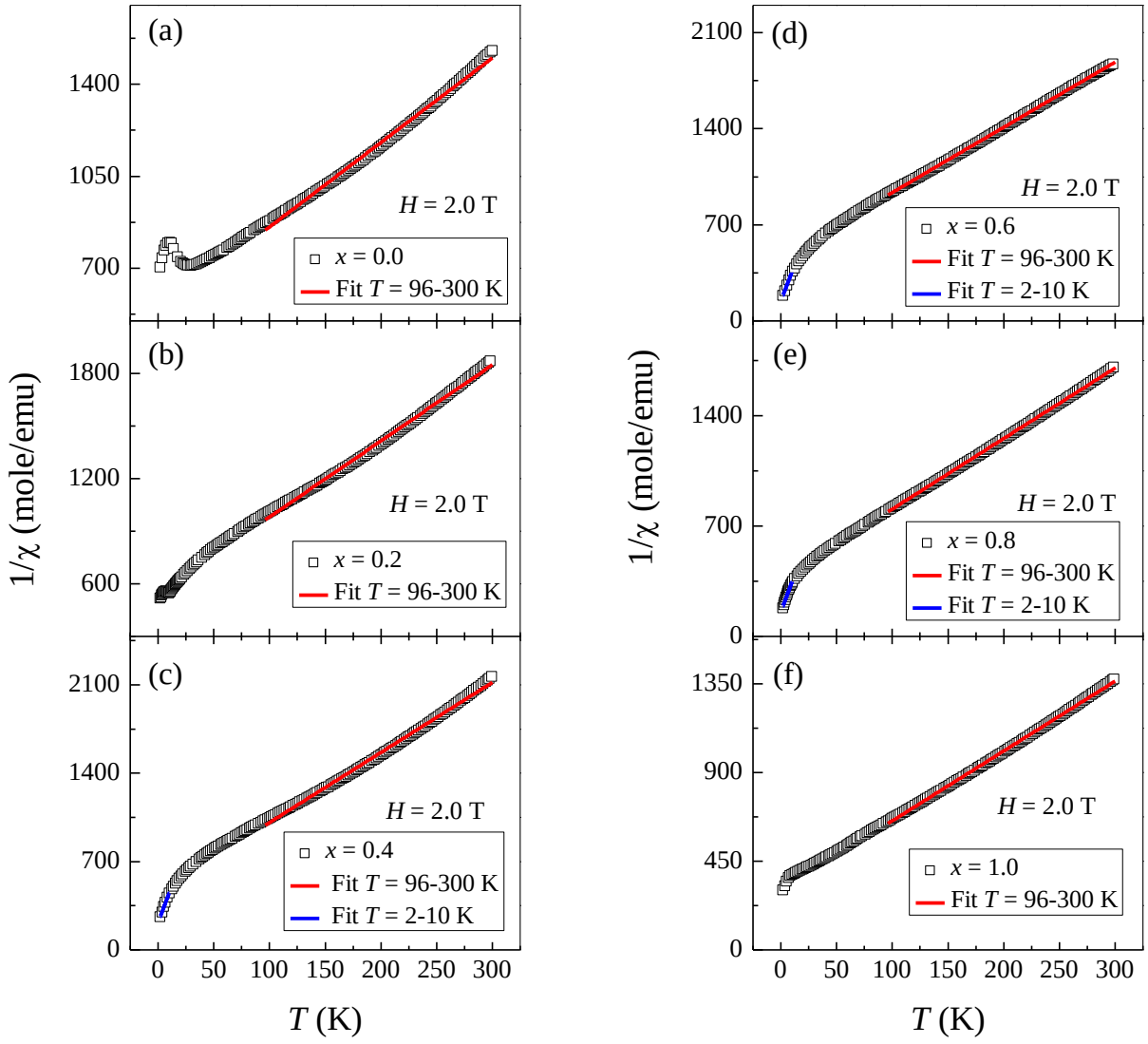

Figure 4.4: The CW fits of the inverse dc susceptibility measured at 2 T for $Li_2In_{1-x}Sc_xMo_3O_8$, x = (a) 0.0, (b) 0.2, (c) 0.4, (d) 0.6, (e) 0.8, and (f) 1.0.

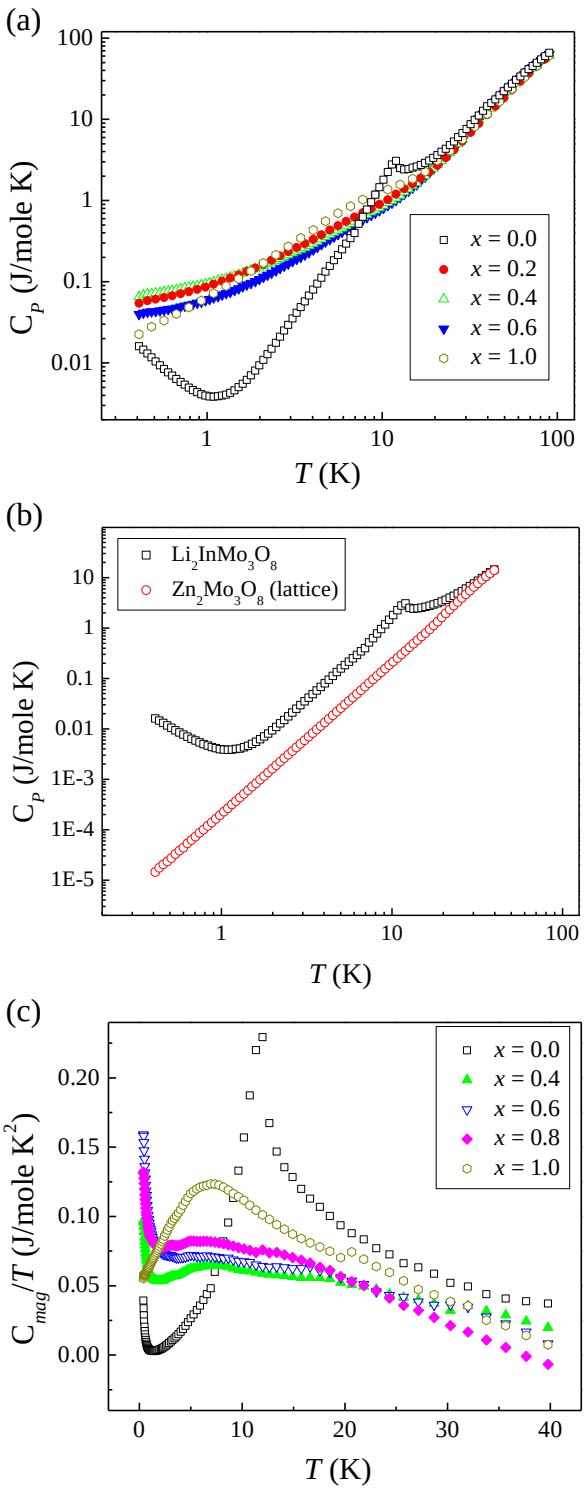

Figure 4.5: (a) The temperature dependence of the specific heat capacity measured at zero field. (b) The specific heat for the $x = 0$ sample as well as the for nonmagnetic $Zn_2Mo_3O_8$ which was used to subtract off the lattice contribution. (c) The magnetic specific heat divided by temperature measured at zero field.

in Fig. 4.5(b), was scaled by molar mass and then subtracted from the molar specific heat data in order to calculate the magnetic specific heat capacity for each sample.

As shown in Fig 4.5(c), the magnetic specific heat capacity divided by the temperature for each sample reveals a nearly linear region from T = 1-10 K for the x = 0.4, 0.6, and 0.8 samples. As a result, the magnetic molar specific heat capacity in these regions should vary linearly with temperature which has been reported as proof of the existence of a QSL state in previously reported organic salts.[157, 158, 159] Figure 4.6(a-f) shows the power law fits for each samples. The data shows that for the x = 0.6 samples, C_{mag} varies as $T^{1.04}$ and thus is approximately linear in the region of interest. Similarly, the x = 0.4 and 0.8 samples vary as $T^{1.1}$ and $T^{1.02}$, respectively. Moreover, below 1 K, the magnetic heat capacity of the x = 0.6 sample can roughly be fit with a $T^{2/3}$ power law which has been theorized to be associated with a U(1) QSL state.[21, 148, 155, 156] Therefore, the samples in this intermediate region are strong potential QSL candidates.

With convincing evidence of a potential QSL state well established, it was time to probe the magnetic ground state directly. Time differential μSR measurements were performed on the x = 0.0, 0.2, 0.4, 0.6, and 1.0 samples, and the results of this study can be found in Ref. 148. The experiments revealed that the x = 0.0 sample demonstrated LRO and corroborated that the $S = 1/2$ magnetic moment is highly distributed over the Mo_3O_{13} cluster, illustrated in Fig. 4.7(a). [155] On the other hand, measurements at 25 mK revealed a weakly relaxing dynamic fraction and an inhomogeneous mix of disordered static magnetism for the x = 0.2, 0.4, and 1.0 samples, and no indication of static fields originating from electron spins for the x = 0.6 sample, illustrated in Fig. 4.7(b).[155]

The inhomogeneous samples were then measured in various longitudinal fields, and the muon polarization for the zero field and field measurements for each sample was fit using a two-component polarization function, $P_{tot} = fP_S(t) + (1-f)P_D(t)$, where $P_S(t)$ is the polarization for the fraction of of muons stopping in a static fraction and $P_D(t)$ is the contribution from regions with dynamic electron spins. The details of the fits can be found in Ref. 148. These fits are shown via black lines in Fig. 4.7 and indicate that the frozen fraction of spins for the inhomogeneous samples are 49%, 25%, and 43% for the x = 0.2, 0.4, and 1.0 samples, respectively. The consistency between the

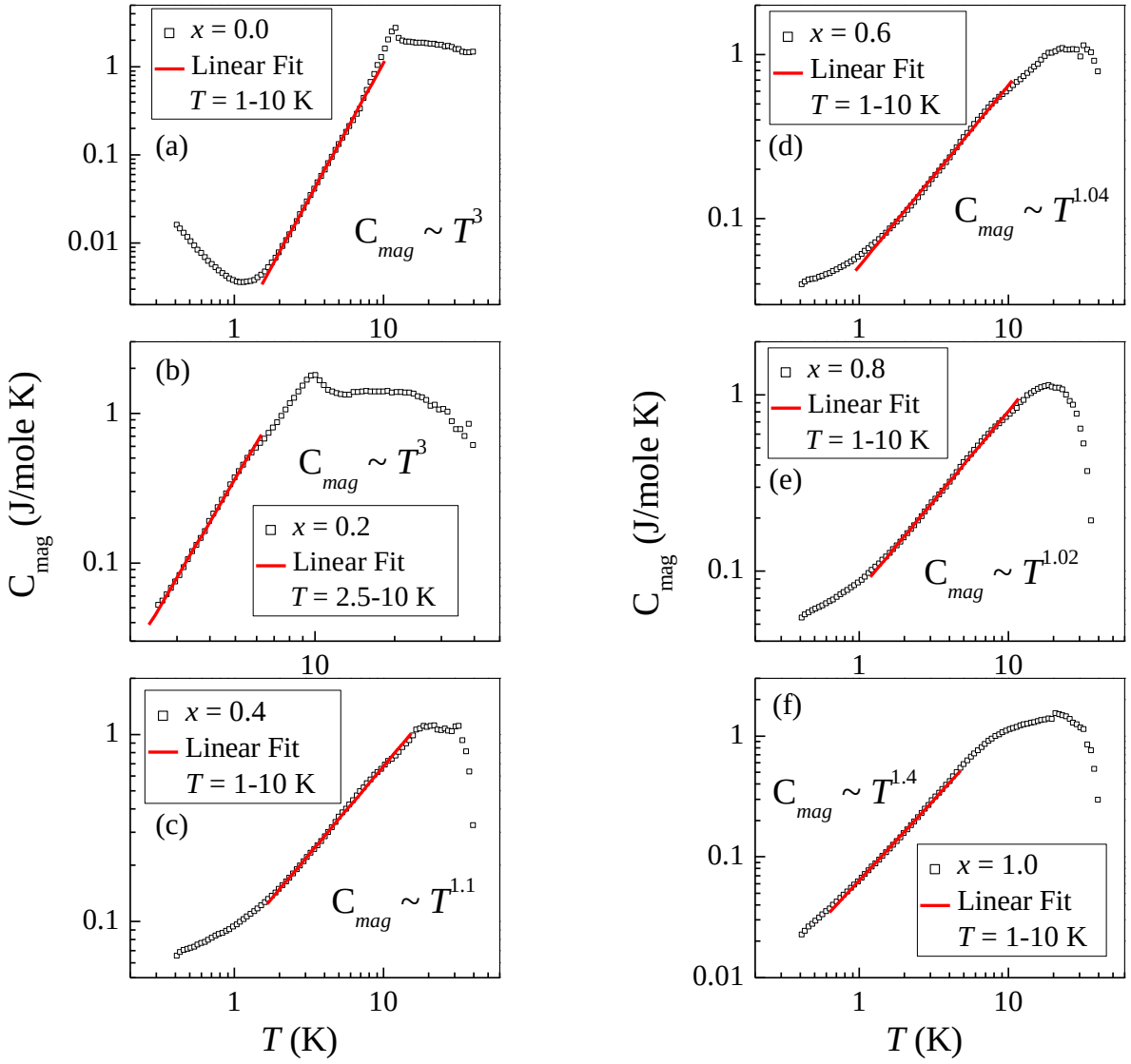

Figure 4.6: The power law fit of the magnetic specific heat for $Li_2In_{1-x}Sc_xMo_3O_8$, x = (a) 0.0, (b) 0.2, (c) 0.4, (d) 0.6, (e) 0.8, and (f) 1.0.

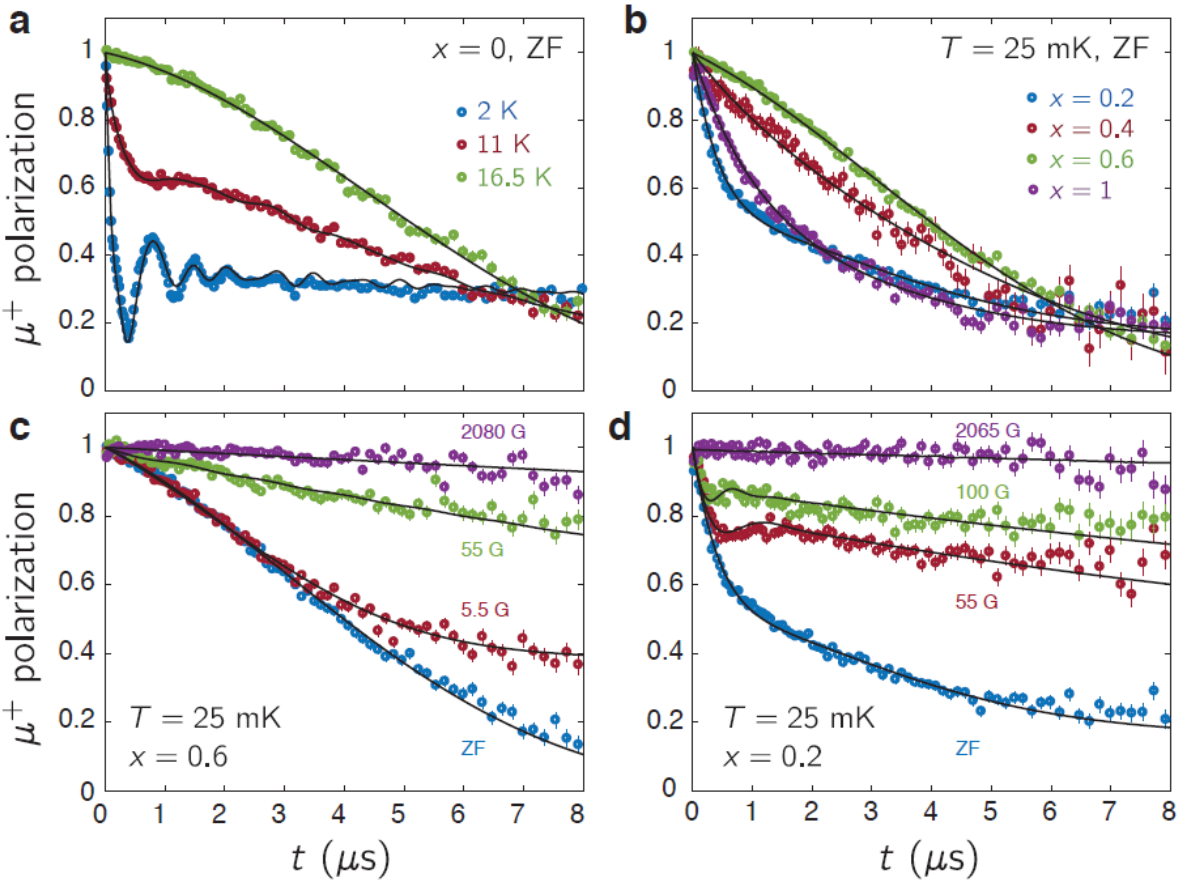

Figure 4.7: (a) For $Li_2InMo_3O_8$, the zero-field muon spin polarization $P(t)$ measured at various temperatures. (b) For $Li_2In_{1-x}Sc_xMo_3O_8$, the zero-field $P(t)$ measured at 25 mK. For (c) $x = 0.6$ and (d) $x = 0.2$, the polarization in various longitudinal fields. The black lines are fits which are described in the text. This figure was taken directly from Ref. C4-Akbari-Sharif1.

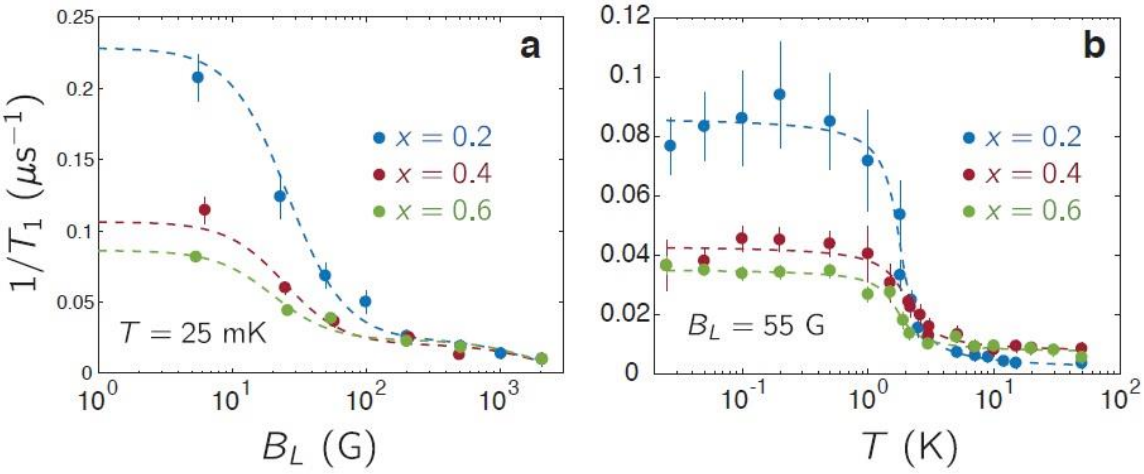

Figure 4.8: (a) The longitudinal-field dependence of the spin-lattice relaxation rate at base temperature with fits given by Redfield theory with two different fluctuation frequencies. (b) The temperature dependence of the relaxation rate in a longitudinal field of 55 G. This figure was taken directly from Ref. 148.

calculations and the measurements for the $x = 0.6$ and 0.2 samples shown in Fig. 4.7(c) and (d), respectively, provide strong evidence that the frozen and dynamic fractions of spins calculated for each sample are accurate.[155] Moreover, as shown in Fig. 4.8(a), the frozen fractions are also fit via the $1/T_1(B_L)$ data with Redfield Theory using a sum of two characteristic fluctuation frequencies,[160] and relaxation plateaus are revealed in the temperature dependence of $1/T_1$ which is a common yet still crudely understood feature of potential QSL materials.[161, 162, 163, 164, 155] A magnetic phase diagram constructed from these μSR results was taken from Ref. 148 and is shown in Fig. 4.9

4.2.2 (Mg,Zn)$ScMo_3O_8$

While the Mo cluster compounds $Li_2In_{1-x}Sc_xMo_3O_8$ exhibited several different magnetic ground states, (Mg,Zn)$ScMo_3O_8$ introduces another layer of diversity. Polycrystalline samples of (Mg,Zn)$Sc_xMo_3O_8$ were synthesized as described in Ch. 2.1. In order to ensure the quality of each sample, they were first studied via XRD at room temperature. The compounds crystallize into the hexagonal space group $P6_3mc$, as seen in Fig. 4.10(a), and the Mo atoms form a "breathing" Kagome lattice in the ab-plane similar to other systems

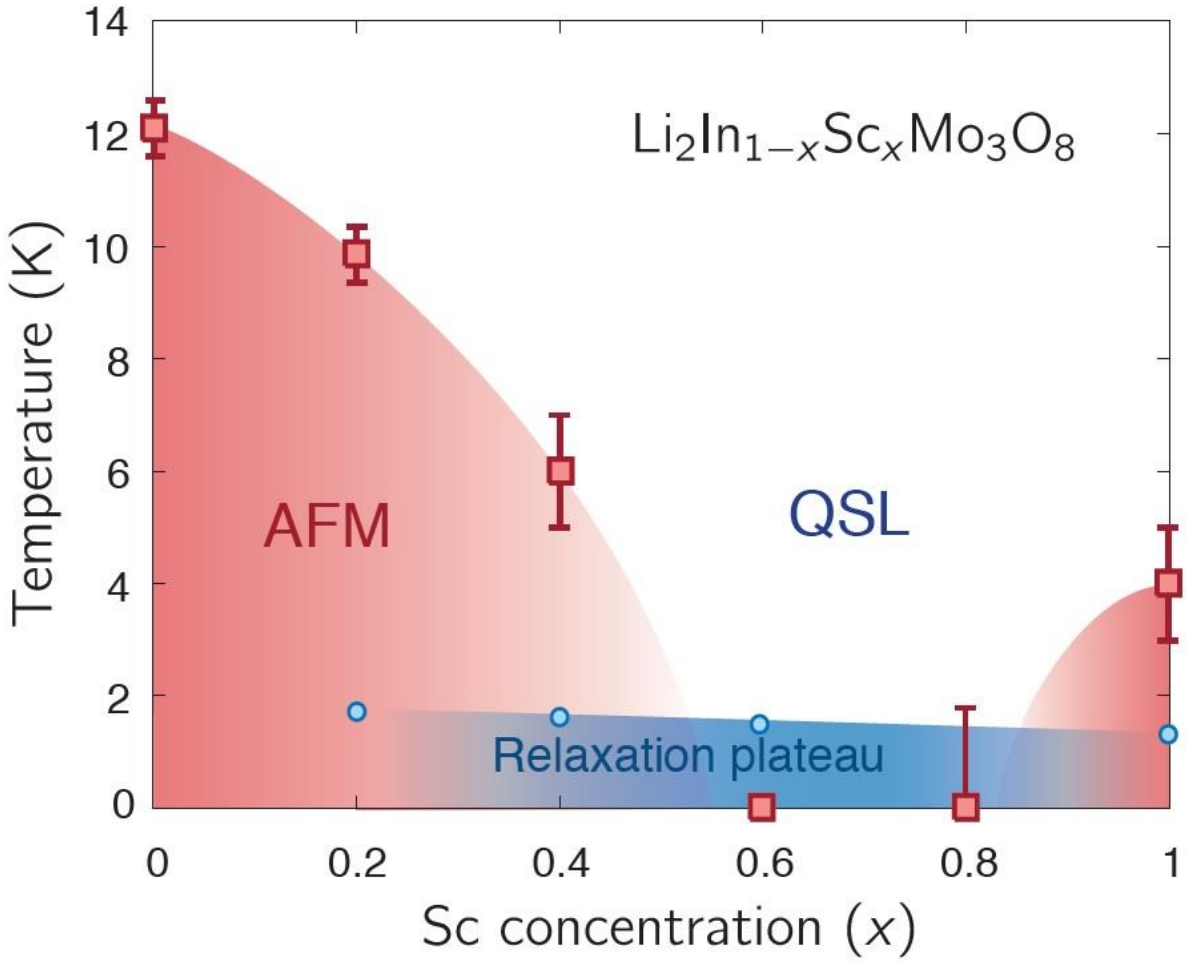

Figure 4.9: The magnetic phase diagram determined by μSR. This figure was taken directly from Ref. 148.

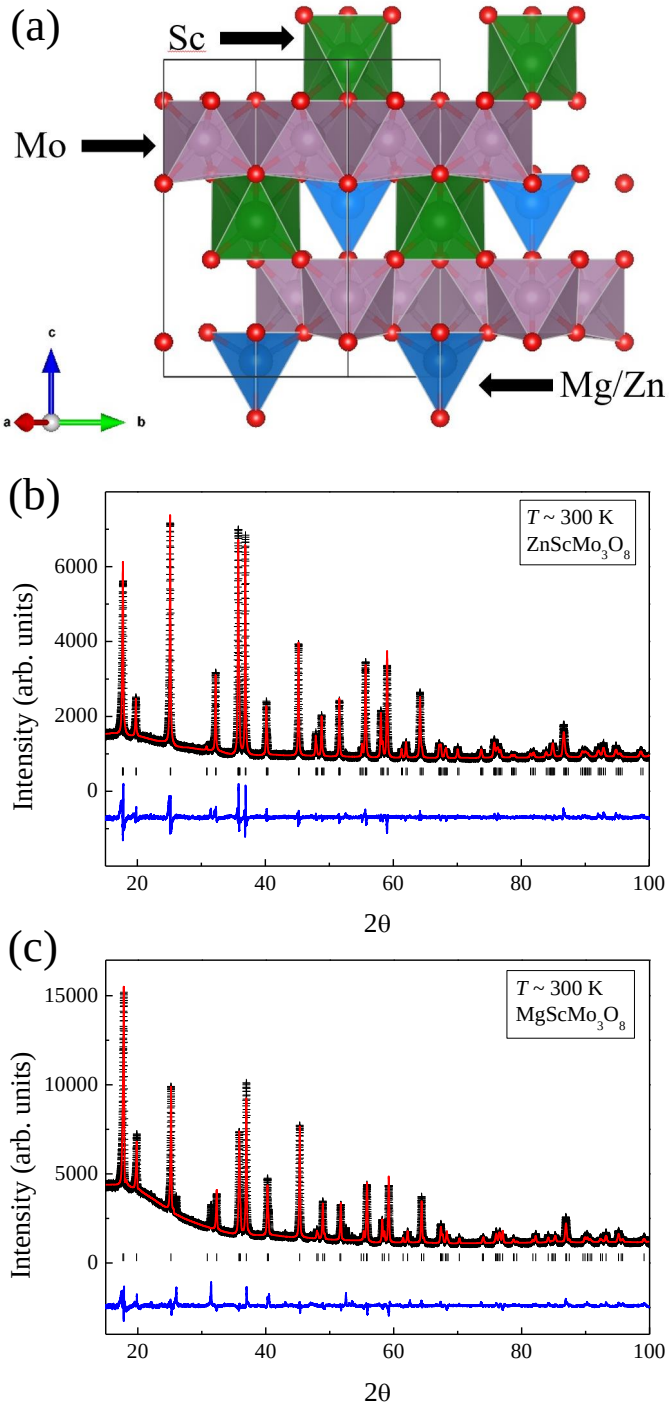

Figure 4.10: (a) The hexagonal $P6_3mc$ crystal structure of (Mg,Zn)$ScMo_3O_8$; the XRD pattern (crosses) for polycrystalline (b) $ZnScMo_3O_8$ and (c) $MgScMo_3O_8$ at room temperature and zero field. The solid curves are the best fits from the Rietveld refinements using *FullProf Suite*. The vertical marks indicate the position of Bragg reflections, and the bottom curves show the difference between the observed and calculated intensities.

Table 4.3: Structural parameters at room temperature (space group $P6_3mc$) for (a) $ZnScMo_3O_8$ and (b) $MgScMo_3O_8$ determined from refined XRD measurements.

Refinement	Atom	Site	x	y	z	Occupancy
	Zn	2b	1/3	2/3	0.554(27)	0.16667
	Sc	2b	1/3	2/3	0.996(27)	0.16667
(a)	Mo	6c	0.14458(7)	0.85543(7)	0.255(27)	0.50
$ZnScMo_3O_8$	O1	2a	0	0	0.116(27)	0.16667
$\chi^2 = 1.88$	O2	2b	1/3	2/3	0.370(27)	0.16667
	O3	6c	0.49225(59)	0.50774(59)	0.138(27)	0.50
	O4	6c	0.83591(73)	0.16409(73)	0.373(27)	0.50
			$a = b = 5.80017(8)$ Å, $c = 9.99115(16)$ Å			
			Overall B-factor = 2.141(33) Å^2			
	Mg	2b	1/3	2/3	0.580(35)	.16667
	Sc	2b	1/3	2/3	0.999(35)	.16667
(b)	Mo	6c	0.14507(6)	0.85493(6)	0.254(35)	.50
$MgScMo_3O_8$	O1	2a	0	0	0.112(35)	.16667
$\chi^2 = 2.66$	O2	2b	1/3	2/3	0.363(35)	.16667
	O3	6c	0.49143(39)	0.50857(39)	0.138(35)	.50
	O4	6c	0.82392(72)	0.17608(72)	0.371(35)	.50
			$a = b = 5.78507(8)$ Å, $c = 9.95680(16)$ Å			
			Overall B-factor = 2.450(29) Å^2			

containing the Mo_3O_{13} cluster. The Rietveld refinement of the XRD patterns are shown in Fig. 4.10(b-c), and the results of the XRD fittings are shown in Table 4.3. The site positions and lattice parameters are consistent with previously reported results for $ZnScMo_3O_8$.[154] The XRD refinement also provided the Mo-Mo bond lengths necessary to define $\lambda_{Mg} = 1.2977(4)$ and $\lambda_{Zn} = 1.3056(3)$, significantly larger than the values obtained for the QSL states previously discussed.

The bulk magnetization properties were then probed using ac and dc susceptibility as well as isothermal magnetization measurements. From the temperature dependence of the dc magnetic susceptibility measured at various applied fields shown in Fig. 4.11(a), a slope change at low fields near $T_C = 8$ K is observed which represents a magnetic transition. As the applied field is increased, the value of T_C increases. Additionally, T_C displays a similar relationship with the applied field for the temperature dependence of the derivative of χ. Such temperature dependence observed for T_C is indicative of a FM transition. The CW analysis of the $1/\chi$ data above 50 K shown in Fig. 4.11(b) yields an effective magnetic moment of $\mu_{eff} = 1.28\ \mu_B$ and a Curie temperature of $\theta_{CW} = 18.5$ K which are in good agreement with the previously reported values.[154] Additionally, the value of μ_{eff} is slightly smaller than that of a spin-1/2 system.

Figure 4.11(c) shows the dc magnetization measured at various temperatures. While a clear hysteresis loop is visible in the data measured below T_C, further corroborating the existence of a FM transition, the magnetization up to 14 T saturates at 0.55 μ_B/f.u., only half of the expected value for a spin-1/2 system; although, it is possible that the full moment could be recovered using a higher applied field.

The temperature dependence of the ac magnetic susceptibility measured at 0.055 T using various frequencies for $ZnScMo_3O_8$ is shown in Fig. 4.11(d). Again, a slope change is evident near $T_C = 8$ K indicating a magnetic transition, but no frequency dependence was observed in χ'_{AC} or $d\chi'_{AC}/dT$. No ac magnetic susceptibility was measured for $MgScMo_3O_8$.

The results for $MgScMo_3O_8$ are very similar. As shown in Fig. 4.12(a), the temperature dependence of the dc magnetic susceptibility measured at various applied fields again shows a slope change at low fields near $T_C = 8$ K. As the applied field is increased, the value of T_C increases. Additionally, T_C displays a similar relationship with the applied field for the

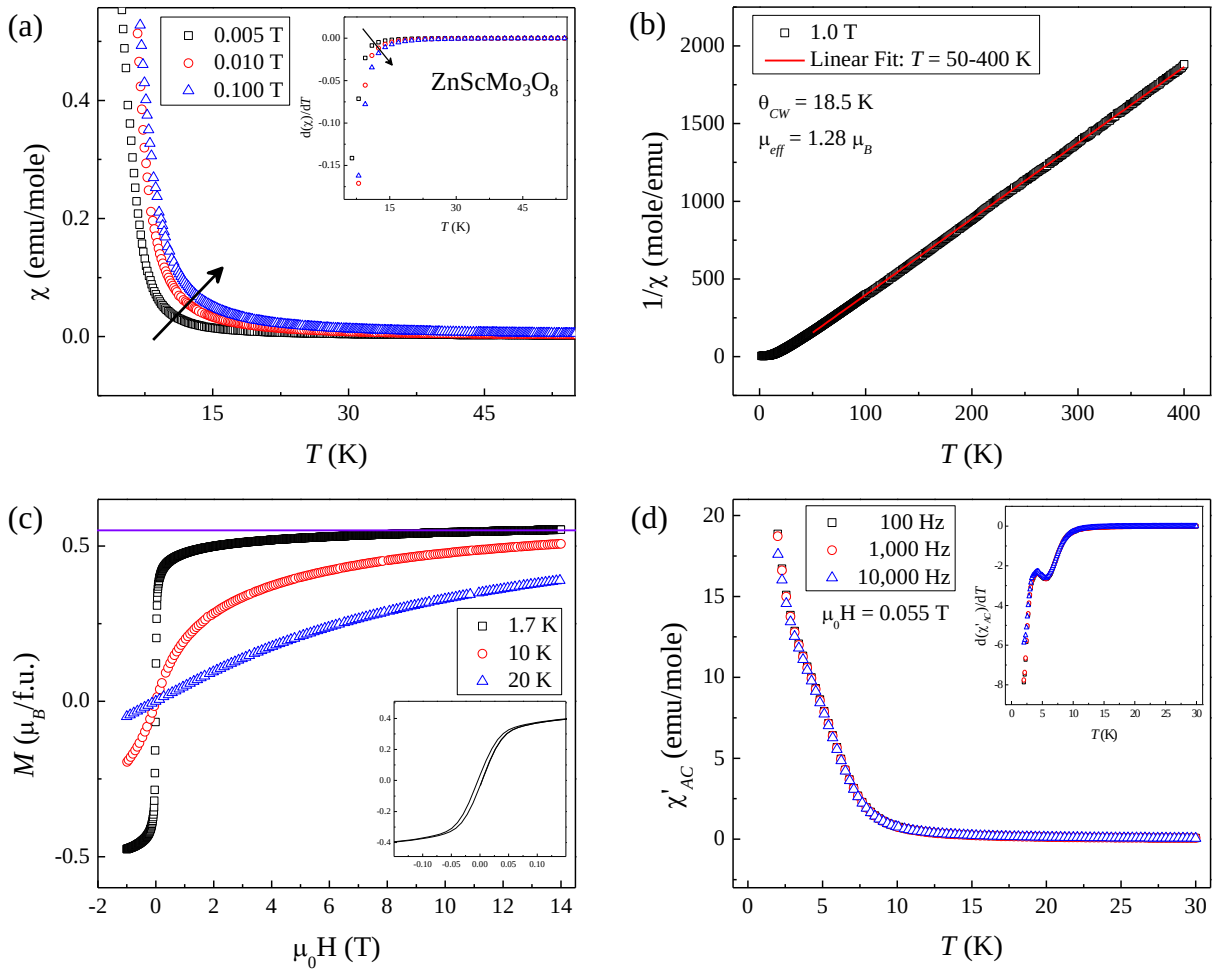

Figure 4.11: For $ZnScMo_3O_8$, (a) the temperature dependence of the dc susceptibility at various magnetic field strengths. The inset shows the temperature dependence of the derivative of the dc susceptibility; (b) the inverse dc susceptibility at 1.0 T as well as the Curie-Weiss fit of the data from 50-400 K; (c) the magnetization curve at various temperatures. The solid violet line marks the maximum moment size of 0.55 μ_B. The inset shows the zoomed-in hysteresis loop; (d) the temperature dependence of the ac susceptibility at 0.055 T using various frequencies. The inset shows the temperature dependence of the derivative of the ac susceptibility.

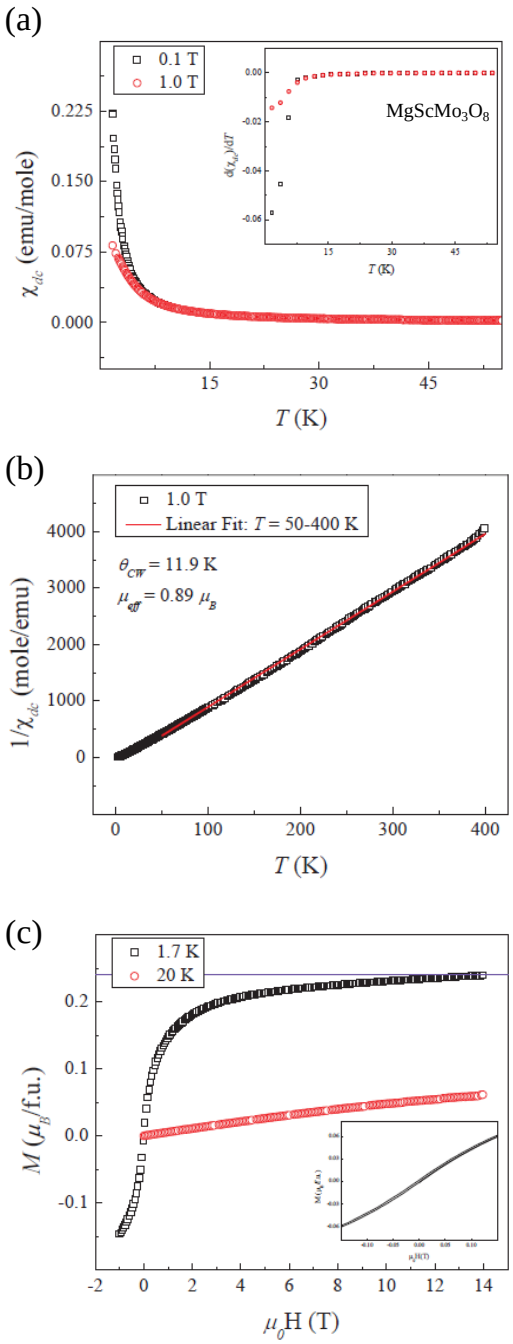

Figure 4.12: For $MgScMo_3O_8$, (a) the temperature dependence of the dc susceptibility at various magnetic field strengths. The inset shows the temperature dependence of the derivative of the dc susceptibility; (b) the inverse dc susceptibility at 1.0 T as well as the Curie-Weiss fit of the data from 50-400 K; (c) the magnetization curve at various temperatures. The solid violet line marks the maximum moment size of 0.24 μ_B. The inset shows the zoomed-in hysteresis loop.

temperature dependence of the derivative of χ. Such temperature dependence observed for T_C is indicative of a FM transition. The CW analysis of the $1/\chi$ data above 50 K shown in Fig. 4.12(b) yields an effective magnetic moment of $\mu_{eff} = 0.89\ \mu_B$ and a Curie temperature of $\theta_{CW} = 11.9$ K. Here, the value of μ_{eff} is clearly suppressed as it lower than that of a spin-1/2 system.

Figure 4.12(c) shows the dc magnetization measured at various temperatures. The hysteresis loop in this compound is noticeably smaller, indicating a shorter-ranged transition, and the magnetization up to 14 T saturates at 0.24 μ_B/f.u., a quarter of the value expected for a spin-1/2 system. Like before, it is possible that the full moment could be recovered using a higher applied field.

In order to further investigate the nature of the magnetic transition, specific heat measurements were obtained at various magnetic field strengths. At zero field, the data for $ZnScMo_3O_8$ shows a cusp near $T_C = 8$ K as shown in Fig. 4.13(a). As the field strength is increased, T_C increases and the feature broadens. This behavior further suggests that a FM transition occurs near T_C.

In order to analyze the magnetic specific heat, a non-magnetic isostructural compound $Zn_2Mo_3O_8$ was measured to obtain the lattice component of the specific heat. The lattice component was scaled by the molar mass, illustrated in Fig. 4.13(b) and Fig. 4.14(b) for $ZnScMo_3O_8$ and $MgScMo_3O_8$, respectively, and then subtracted from the specific heat data. At zero field, a peak in the magnetic specific heat appears near 6 K for $ZnScMo_3O_8$ as illustrated in Fig. 4.13(c), and the location of the peak increases with increasing magnetic field strength as one would expect for a FM transition.

The magnetic specific heat data was integrated against temperature in order to calculate the magnetic entropy of the system. As observed in Fig. 4.13(d), the entropy for $ZnScMo_3O_8$ saturates at increasingly larger values as the magnetic field strength increases. For a spin 1/2 system, we expect this saturation to occur near $R\ln 2$; however, the measurements here only reach close to half of $R\ln 2$. This relationship is similar to the saturation that occurs in the dc magnetization.

The results for $MgScMo_3O_8$ were very similar. Depicted in Fig. 4.14(a), the zero field specific heat data revealed no major features; however, when a small magnetic field is applied,

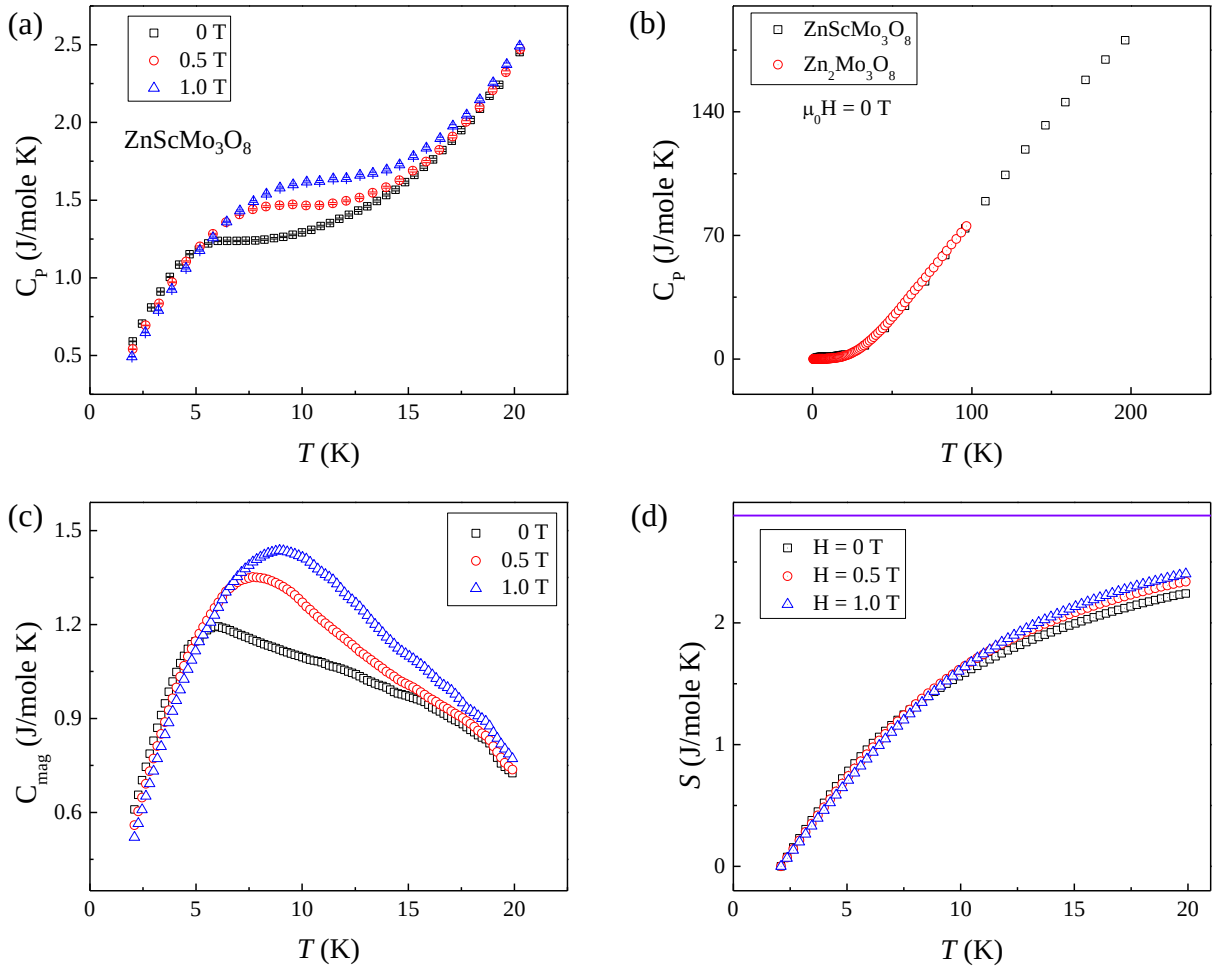

Figure 4.13: For $ZnScMo_3O_8$, (a) the temperature dependence of the specific heat at various magnetic field strengths; (b) the temperature dependence at zero field of the specific heat of $ZnScMo_3O_8$ and the non-magnetic isostructural compound $Zn_2Mo_3O_8$; (c) the temperature dependence of the magnetic specific heat at various magnetic field strengths; (d) the temperature dependence of the total entropy of the system at various magnetic field strengths. The solid violet line lies at $(R\ln 2)/2$.

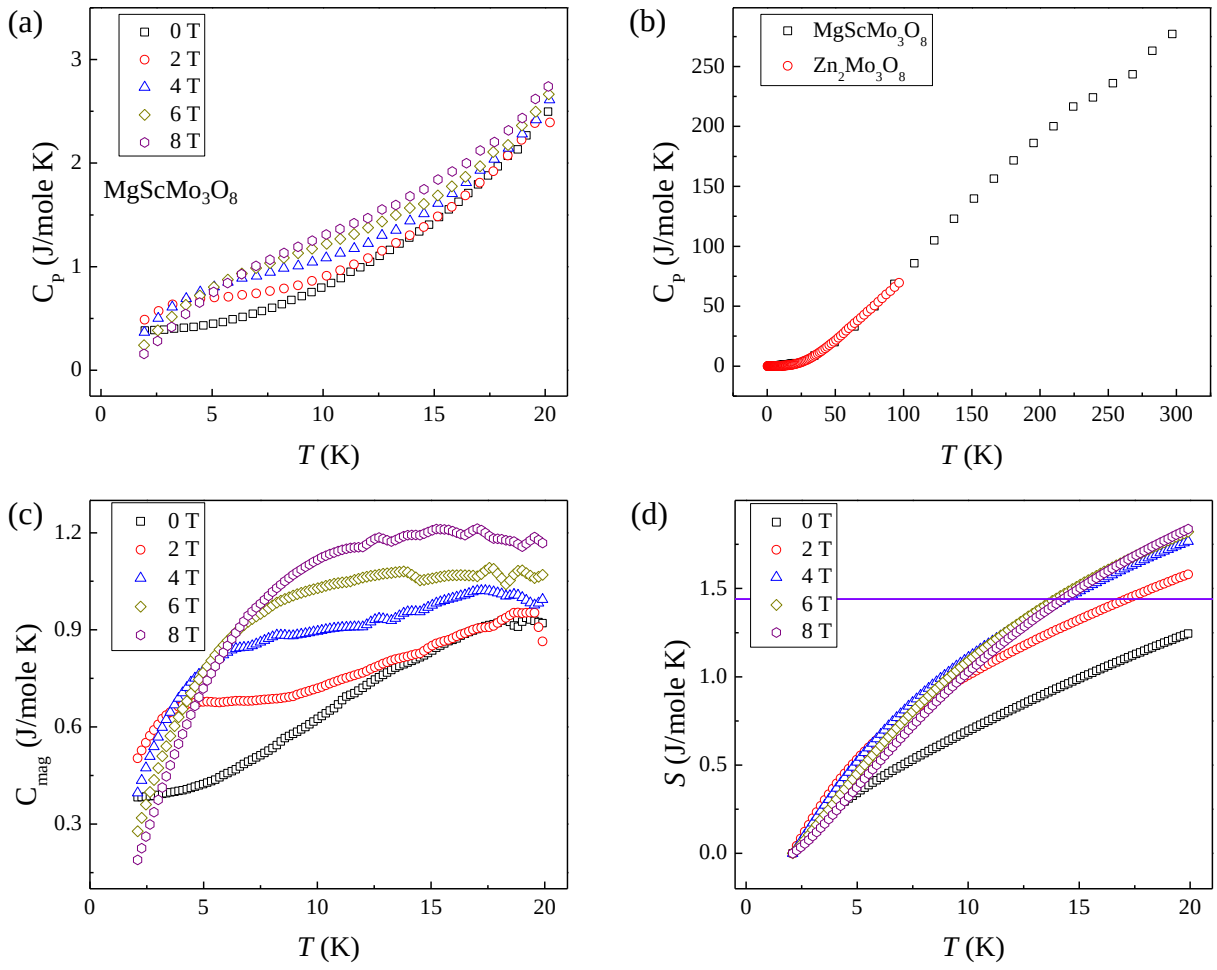

Figure 4.14: For $MgScMo_3O_8$, (a) the temperature dependence of the specific heat at various magnetic field strengths; (b) the temperature dependence at zero field of the specific heat of $MgScMo_3O_8$ and the non-magnetic isostructural compound $Zn_2Mo_3O_8$; (c) the temperature dependence of the magnetic specific heat at various magnetic field strengths; (d) the temperature dependence of the total entropy of the system at various magnetic field strengths. The solid violet line lies at $(R\ln 2)/4$.

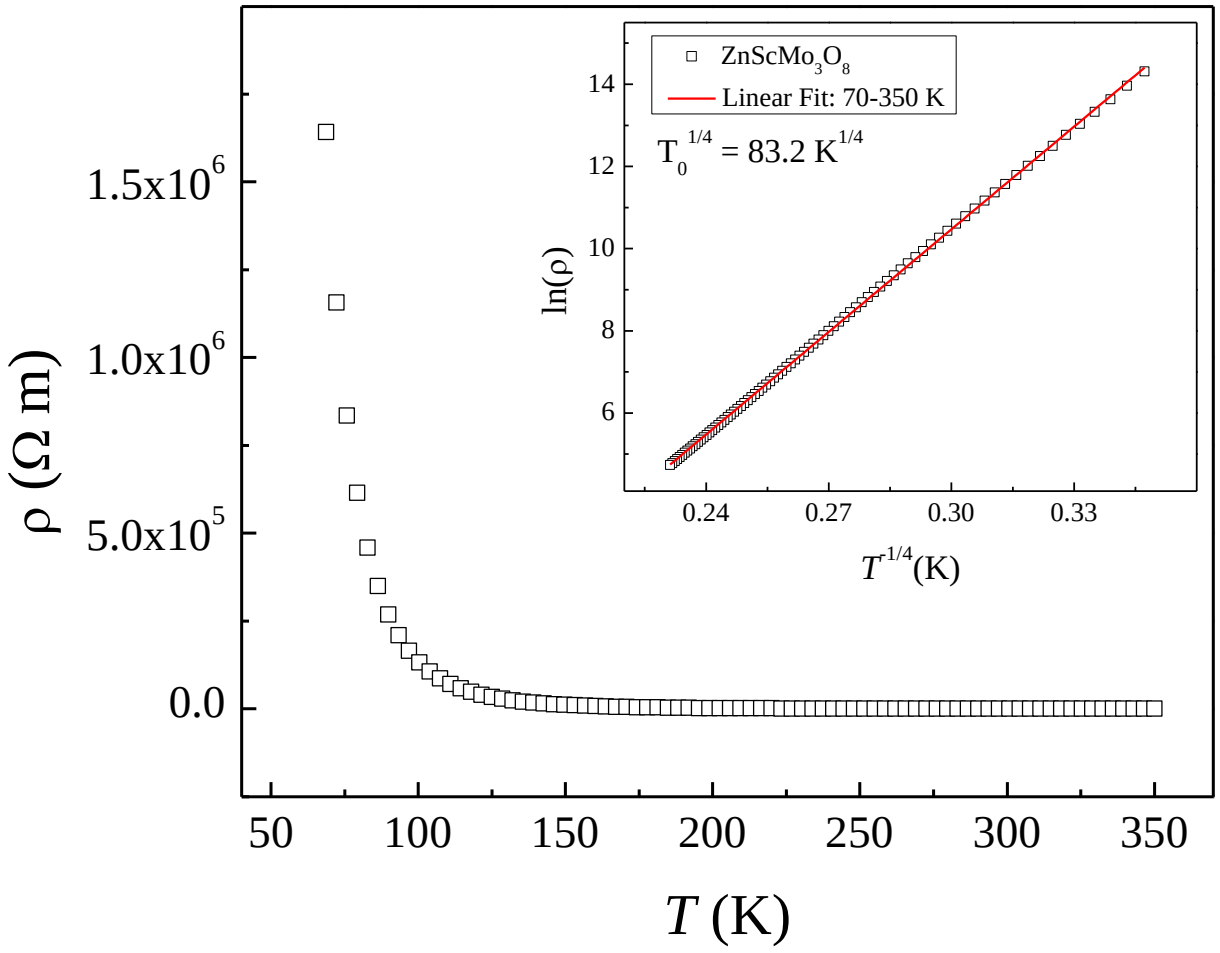

Figure 4.15: For $ZnScMo_3O_8$, the temperature dependence of the resistivity at zero field. The inset shows the calculated linear fit in the Mott-VRH model of $\ln(\rho)$ vs. $T^{-1/4}$.

a similar cusp to that of the $ZnScMo_3O_8$ data appears near $T_C = 8$ K, and T_C increases with increasing field strength. The magnetic specific heat capacity reveals nearly the same behavior as shown in Fig. 4.14(c). This behavior also suggests that a FM transition occurs near T_C. Furthermore, the entropy depicted in Fig. 4.14(d) only reaches close to a quarter of $R\ln 2$. This relationship is again similar to the saturation that occurs in the dc magnetization.

Finally, the zero field temperature dependence of the resistivity for $ZnScMo_3O_8$ can be seen in Figure 4.15. Clearly, $ZnScMo_3O_8$ behaves as an insulator in this temperature regime. The data was analyzed using Mott's variable range hopping (Mott-VRH) model. In this model, hopping electrons attempt to find the lowest activation energy ΔE as well

as the shortest hopping distance, and the hopping probability is maximized by an optimum hopping distance r. Under zero bias, the hopping probability is

$$P \sim exp(-2r/a - \Delta E/k_B T), \tag{4.2}$$

where a is the localization length, k_B is the Boltzmann constant, and ΔE is the activation energy. Assuming a constant density of states, g_0, at the Fermi level, Mott used this equation with $\Delta \mathrm{E} \sim 1/g_0 r^3$ to derive a relation between conductance, G, and temperature, T, which states:

$$G \propto exp(-B/T^{\nu}) \tag{4.3}$$

where $\nu = 1/4$ for 3D systems. [165] As our data was taken between 2 and 300 K, it is reasonable to believe that the behavior will be well-described by this model. [166] Thus we plotted $\ln(\rho)$ vs. $T^{-1/4}$ which was then linearly fit to obtain a characteristic temperature of $T_M^{-1/4} = 83.2\ \mathrm{K}^{-1/4}$.

The zero field temperature dependence of the resistivity was not measured for $MgScMo_3O_8$, but similar 3D insulator behavior is expected due to the similarities between the compound's bulk magnetic and structural properties.

4.3 Discussion

Clearly, the Mo cluster compounds investigated in this Chapter have exhibited several exotic magnetic properties. The results of our $Li_2In_{1-x}Sc_xMo_3O_8$ measurements agree with the previous reports on the $x = 0.0$ and $x = 1.0$ samples and strengthen the arguments that those conclusions are based on. Additionally, we discovered that the ground state of the $x = 0.2$ and 0.4 samples consist of both static and dynamic spins. While no μSR measurements were performed on the $x = 0.8$ sample, it is assumed that the ground state is similar based on the similar bulk magnetic and thermal properties. We also have identified a prime U(1) QSL candidate in $Li_2In_{0.4}Sc_{0.6}Mo_3O_8$. Moreover, we have identified two FM

Mo cluster compounds, (Mg,Zn)$ScMo_3O_8$, which exhibit characteristics associated with quenched magnetic moments.

Several measurements including the linear T dependence of the magnetic specific heat from 1-10 K as well as the roughly $T^{2/3}$ power law dependence of the low temperature ($T < 1$ K) magnetic specific heat indicate that $Li_2In_{0.4}Sc_{0.6}Mo_3O_8$ may be described by a U(1) QSL state. Furthermore, the μSR experiments indicated that the $x = 0.2$, 0.4, and 1.0 samples also contain frozen spin moments at low temperatures while simultaneously revealing no indication of static fields originating from electron spins. The mechanisms responsible for the QSL states in $Li_2In_{1-x}Sc_xMo_3O_8$ are likely similar to those responsible for the QSL state in $LiZn_2Mo_3O_8$. Currently, $LiZn_2Mo_3O_8$ is believed to be a Mott insulator where the charge degrees of freedom are localized in cluster units, known as a cluster Mott insulator (CMI).[142, 145, 148] The ground state of Mott insulators with an odd number of electrons per unit cell may exhibit a QSL state if there is no spontaneous symmetry breaking.[167] These QSLs arise from strong charge fluctuations in the weak Mott regime which can generate sizable long range spin exchanges or spin ring exchanges and suppress possible magnetic orderings.[21, 168]

A characteristic feature of $LiZn_2Mo_3O_8$ is the existence of two CW regimes. At 96 K, the Curie constant is reduced to 1/3 of its high temperature value.[142] It has been shown that a cluster Mott insulator with the PCO previously described will result in two CW regimes.[156] Our data also shows a high temperature and a low temperature CW regime for the intermediate doped samples, and the ratio of the Curie constants in these regions has been provided in Table 4.2. Our samples appear to show $C_2/C_1 \sim 0.25$ as opposed to the 1/3 value found in $LiZn_2Mo_3O_8$. This was originally attributed to two-thirds of the spins condensating into singlet states.[142, 147]. A separate explanation was later proposed explaining the anomaly in terms of a long range PCO which reconstructs the spinon bands, creating a filled sub-band with 2/3 of the spins and a partially filled upper sub-band with the remaining 1/3 of the spins.[148, 156] In this model, above 96 K the full spin degrees of freedom are recovered as the PCO is destroyed. However, such spontaneous breaking of symmetry would normally be observable in the specific heat data. It is believed that disorder plays a role in the absence of such a feature.[156]

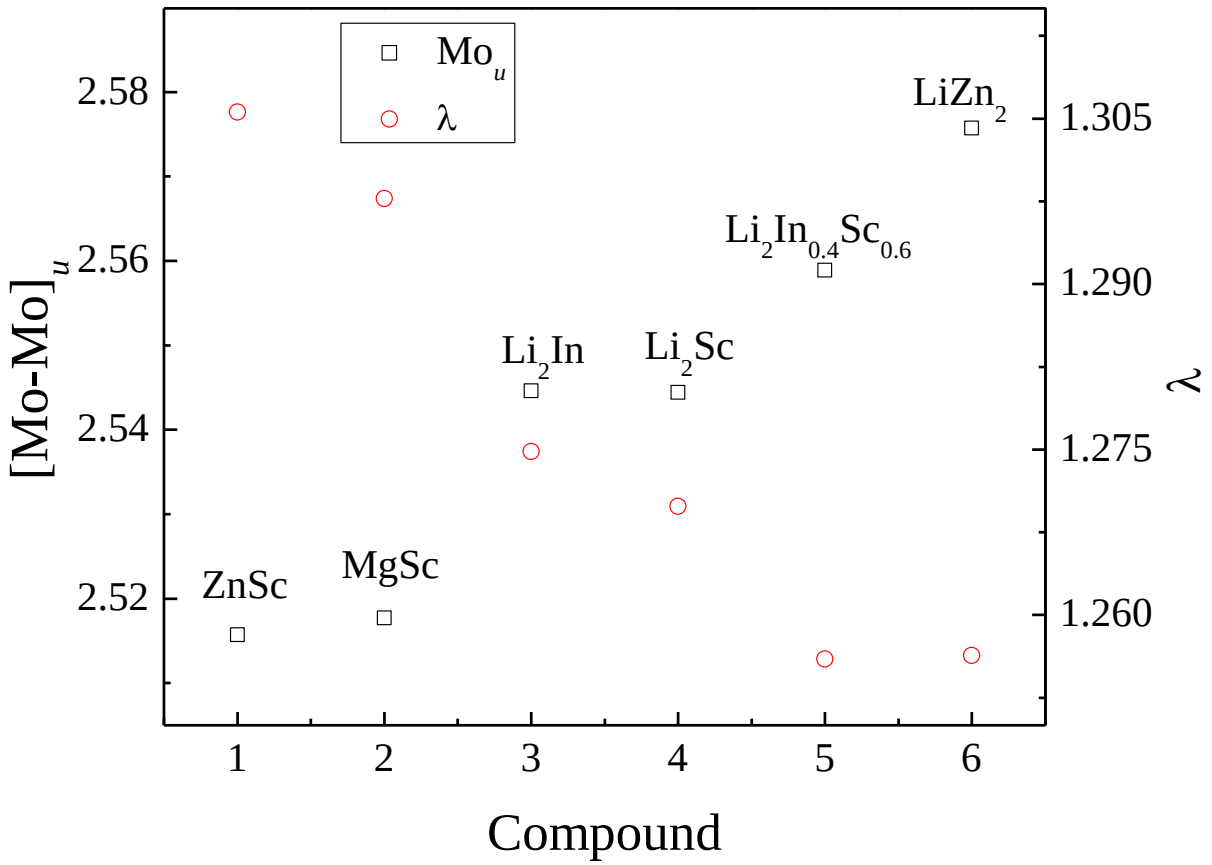

Figure 4.16: The $[\text{Mo-Mo}]_u$ bond lengths and the λ values for various $[Mo_3O_{13}]$ cluster compounds.

A third explanation for this behavior has recently been proposed which explains that the energy scale required to break the PCO could be much larger than the energy gap between the filled and partially filled spinon sub-bands. This would allow the spinons to be thermally excited across the gap while preserving the PCO.[155] Locally, each resonating hexagon in the PCO phase is composed of three coupled spins with a $S = 1/2$ ground state and a $S = 3/2$ excited state. The magnetic susceptibility was calculated for non-interacting resonating hexagons, and the susceptibility for both the $x = 0.6$ sample and for $LiZn_2Mo_3O_8$ was successfully fit using this model.[155] While our measurements seem to support this model, more experimental and theoretical work still needs to be done in order to determine which, if any, of the available theories accurately describes the ground state of these Mo cluster compounds.

Another possible mechanism for the QSL state lies in the level of asymmetry in the Kagome lattice. As explained in Sec. 4.1, the breathing Kagome lattice formed by the Mo atoms forms larger down-triangles and smaller up-triangles which can be used to define the asymmetry parameter λ. For these breathing Kagome systems, λ describes how much the lattice is distorted from a perfect Kagome lattice, where a large λ implies a large amount of distortion. We compared the values of λ at room temperature for several of the Mo cluster compounds that were studied. The results shown in Fig. 4.16 reveal that larger λ values are associated with the compounds which exhibit LRO, while the smallest λ values belong to the materials with a QSL ground state. Similarly, this behavior may also correlate to the size of the up-triangles, illustrated in Fig. 4.16 using size of the $[\text{Mo-Mo}]_u$ bond lengths, where the smaller triangles are associated with LRO and the largest triangles are associated with the QSL states. As the amount of asymmetry and the size of the triangles influence the potential localization of the electrons in the cluster, it is certainly possible that there is a critial value where LRO is no longer possible. Further experiments are necessary to elucidate the matter.

While the mechanism behind the FM transition in the (Mg,Zn)$ScMo_3O_8$ family has not yet been identified, it is noteworthy that the values of λ for these samples are particularly large and the size of the up-triangles are particularly small. It appears likely that the difference between a possible FM LRO versus an AFM LRO may be influenced by these factors as well. Additionally, the dc magnetization measurements and the entropy calculations for the FM samples indicate potentially quenched moments. As more Mo cluster samples are characterized, the importance of these properties should become clearer.

4.4 Conclusions

In summary, we report detailed experimental studies of the Mo cluster compounds $Li_2In_{1-x}Sc_xMo_3O_8$ and (Mg,Zn)$ScMo_3O_8$, focusing on their magnetic and thermal properties. We observed several different magnetic ground states ranging from LRO AFM and FM ground states to a pure QSL state. By comparing the different Mo cluster compounds, we identified a asymmetry in the Kagome lattice as a possible mechanism for these differences.

Furthermore, the QSL states were examined in the context of three separate charge ordering models. Our studies here demonstrate that the combination of triangular lattice compounds with cluster magnets can produce intriguing physical properties. Additional studies on these materials will surely increase our knowledge regarding the fundamental principles of magnetism.

Chapter 5

Conclusion and Outlook

This dissertation focused on the synthesis and characterization of new triangular lattice compounds. Specifically, the properties of the layered perovskites $R\mathrm{Cr}(\mathrm{BO}_3)_2$ (R = Y and Ho) as well as the Mo cluster compounds $\mathrm{Li}_2\mathrm{In}_{1-x}\mathrm{Sc}_x\mathrm{Mo}_3\mathrm{O}_8$ and (Mg,Zn)$\mathrm{ScMo}_3\mathrm{O}_8$ were investigated using several experimental techniques such as XRD and NPD as well as ac and dc susceptibility, specific heat, resistivity, and μSR measurements which revealed many fascinating physical phenomena. It was possible to explain many of the observed behaviors, but there is still work to be done in order to fully understand these materials.

A comprehensive study of the layered perovskites $R\mathrm{Cr}(\mathrm{BO}_3)_2$ (R = Y and Ho) contained in this dissertation examined both the magnetic and electrical properties of the system as well as the interplay between the two. An AFM ground state below $T_N = 8$ K was discovered for both compounds with only the Cr^{3+} ions ordering at zero field. Upon adding a critical magnetic field of $\mathrm{H}_C = 2$ T, the materials adopt a FM ordering which now involves the Cr^{3+} ions and the Ho^{3+} ions. Furthermore, both samples exhibit strong features in their respective dielectric constant measurements around these critical temperature and field values. Therefore, both materials are magnetodielectric. As the addition of the second magnetic ion greatly affects this exchange, it is likely the affect of magnetostriction which occurs as the Ho^{3+} ions begin to order in the presence of an external magnetic field. Moreover, comparing these results to behaviors witnessed in EuTiO_3 indicated that the features observed in the R = Y compound may be related to spin-phonon coupling. A spin wave spectrum for a limited E$-Q$ space was constructed, and a simulation of the spectrum

provided information regarding the NN and NNN interaction strengths. These results were further analyzed via superexchange pathways.

In order to fully understand this system, there is still much experimental and theoretical work to do. Able to probe possible spin-phonon coupling in the R = Y sample, infrared and Raman spectroscopy experiments should be performed on polycrystalline samples. Additionally, it would be very fruitful to pursue the growth of single crystal samples in order to study possible anisotropic effects including additional dielectric constant and polarization (pyroelectric current) measurements. Synthesizing samples with different magnetically active ions would also provide useful comparisons that could lead to a more fundamental understanding of the physics involved. Additionally, more INS measurements would allow the system to be studied in a broader E$-Q$ range which could then be modeled with a more complex Hamiltonian and could include possible spin-orbital coupling terms.

This dissertation also includes an extensive study on the Mo cluster compounds $Li_2In_{1-x}Sc_xMo_3O_8$ (x = 0.0, 0.2, 0.4, 0.6, 0.8, and 1.0) and (Mg,Zn)$ScMo_3O_8$ focusing primarily on the structural and magnetic properties of the system. The measurements confirmed an AFM LRO magnetic ground state for the $x = 0.0$ as well as an inhomogeneous mixture of mix of disordered static magnetism for the x = 0.2, 0.4, and 1.0 samples which is also predicted for the $x = 0.8$ sample, and no indication of static fields originating from electron spins for the $x = 0.6$ sample, indicating a probable QSL ground state; moreover, the (Mg,Zn)$ScMo_3O_8$ compounds were shown to have a FM ground state with potentially quenched magnetic moments. Two CW regimes were observed for the intermediate doping samples similar to the behavior observed in $LiZn_2Mo_3O_8$. This behavior was examined via charge condensation, a long range PCO model, and a non-interacting resonating hexagon model, but more work is needed to exactly explain this phenomenon. The differences in the observed ground states were also examined as a function of the asymmetry of the Kagome lattice. The samples with the largest amount of disorder exhibited LRO while the samples closer to a perfect Kagome lattice showed QSL ground states.

While many interesting physical properties of these Mo cluster compounds were examined, there are still many theoretical and experimental avenues to explore. Single crystal samples should be attempted in order to probe possible anisotropic behavior. Polarized

neutron studies should be undertaken in order to examine the nature of the FM transition in the (Mg,Zn)$ScMo_3O_8$ compounds. Additionally, INS measurements should be performed on all of the samples in order to probe the spin wave dynamics and the exchange interaction strengths of the system. High pressure studies which could be used to tune the asymmetry parameter could also help to determine the importance that asymmetry has on the system. Moreover, synthesizing and characterizing additional Mo cluster compounds is essential to expanding and fine-tuning the current models used to describe not only the QSL states observed but also the other anomalous behavior such as the quenched magnetic moments associated with the FM compounds. It is our hope that expanding upon this research will reveal productive advancements in the field of condensed matter physics.

Bibliography

[1] L. Balents, Nature **464**, 199 (2010). 1, 3, 5, 6

[2] C. Wannier, Phys. Rev. **79**, 357 (1950). 2

[3] e.g. P. -W. Anderson, Mater. Res. Bull. **8**, 153 (1973). 3, 7, 12

[4] S. Liang, B. Doucot, and P. W. Anderson, Phys. Rev. Lett. **61**, 365 (1988). 3

[5] X.-G. Wen, Phys. Rev. B **65**, 165113 (2002). 3

[6] X.-G. Wen, Condens. Matt. Phys. **2013**, 198710 (2013). 5

[7] G. Misguich and C. Lhuillier, in *FrustratedSpinSystems*, edited by H. T. Diep (World Scientific, Singapore, 2005). 5

[8] F. D. M. Haldane, Phys. Rev. Lett. **66**, 1529 (1991). 5

[9] A. P. Ramirez, Annu. Rev. Mater. Sci. **24**, 453 (1994). 5

[10] M. F. Collins and O. A. Petrenko, Can. J. Phys. **75**, 605 (1997). 5, 6

[11] J. Iida, M. Tanaka, Y. Nakagawa, S. Funahashi, N. Kimizuka, and S. Takekawa, J. Phys. Soc. Jpn. **62**, 1723 (1993). 6

[12] S. Mitsuda, M. Mase, K. Prokes, H. Kitazawa, and H. A. Katori, J. Phys. Soc. Jpn. **69**, 3513 (2000). 6

[13] R. Coldea, D. A. Tennant, and Z. Tylczynski, Phys. Rev. B. **68**, 134424 (2003). 6

[14] Y. Shimizu, K. Miyagawa, K. Kanoda, M. Maesato, and G. Saito, Phys. Rev. Lett. **91**, 107001 (2003). 7

[15] T. Itou, A. Oyamada, S. Maegawa, M. Tamura, and R. Kato, Phys. Rev. B **77**, 104413 (2008). 7

[16] P. Khuntia, R. Kumar, A. V. Mahajan, M. Baenitz, and Y. Furukawa, Phys. Rev. B **93** 140408(R) (2016). 7

[17] Y. Zhou, K. Kanoda, and T.-K. Ng, Rev. Mod. Phys. **89**, 025003 (2017). 7

[18] R. J. Cava, A. P. Ramirez, Q. Huang, and J. J. Krajewski, J. Solid State Chem. **140**, 337 (1998). 7

[19] Y. Li, H. Liao, Z. Zhang, S. Li, F. Jin, L. Ling, L. Zhang, Y. Zou, L. Pi, Z. Yang, J. Wang, Z. Wu, and Q. Zhang, Sci. Rep. **5**, 16419 (2105). 7

[20] T. Moriya, Phys. Rev. Lett. **4**, 228 (1960). 7

[21] O. Motrunich, Phys. Rev. B **72**, 045105 (2005). 7, 72, 87

[22] Y. Li, G. Chen, W. Tong, L. Pi, J. Liu, Z. Yang, X. Wang, and Q. Zhang, Phys. Rev. Lett. **115**, 167203 (2015). 8

[23] Y. Li, D. Adroja, P. K. Biswas, P. J. Baker, Q. Zhang, J. Liu, A. A. Tsirlin, P. Gegenwart, and Q. Zhang, Phys. Rev. Lett. **117**, 097201 (2016). 8

[24] J. A. M. Paddison, M. Daum, Z.L. Dun, G. Ehlers, Y. Liu, M. B. Stone, H.D. Zhou, and M. Mourigal, Nat. Phys. **13**, 117 (2017). 8

[25] Y. Shen, Y.-D. Li, H. Wo, Y. Li, S. Shen, B. Pan, Q. Wang, H. C. Walker, P. Steffens, M. Boehm, Y. Hao, D. L. Quintero-Castro, L. W. Harriger, M. D. Frontzek, L. Hao, S. Meng, Q. Zhang, G. Chen, and J. Zhao, Nature (London) **540**, 559 (2016). 8

[26] Y. Li, D. Adroja, R. I. Bewley, D. Voneshen, A. A. Tsirlin, P. Gegenwart, and Q. Zhang, Phys. Rev. Lett. **118**, 107202 (2017). 8

[27] Y. Li, D. Adroja, D. Voneshen, R. I. Bewley, Q. Zhang, A. A. Tsirlin, and P. Gegenwart, Nature Commun. **8**, 15814 (2017). 8

[28] Y. Xu, J. Zhang, Y.S. Li, Y.J. Yu, X. C. Hong, Q.M. Zhang, and S. Y. Li, Phys. Rev. Lett. **117**, 267202 (2016). 8

[29] Q. Luo, S. Hu, B. Xi, J. Zhao, and X. Wang, Phys. Rev. B **95**, 165110 (2017). 8

[30] Z. Zhu, P. A. Maksimov, S. R. White, and A. L. Chernyshev, Phys. Rev. Lett. **119**, 157201 (2017). 8

[31] S. Nakatsuji, Y. Nambu, H. Tonomura, O. Sakai, S. Jonas, C. Broholm, H. Tsunetsugu, Y. Qiu, and Y. Maeno, Science **309**, 1697 (2005). 8, 10

[32] Y. Nambu, S. Nakatsuji, and Y. Maeno, J. Phys. Soc. Jpn. **75**, 043711 (2006). 10

[33] S. Nakatsuji, Y. Nambu, K. Onuma, S. Jonas, C. Broholm, and Y. Maeno, J. Phys.: Condens. Matter **19**, 145232 (2007). 10

[34] S. Nakatsuji, Y. Nambu, and S. Onoda, J. Phys. Soc. Jpn. **79**, 011003 (2010). 10

[35] D.E. Maclaughlin, R.H. Heffner, S. Nakatsuji, Y. Nambu, K. Onuma, Y. Maeno, K. Ishida, O.O. bernal, and L. Shu, J. of Mag. and Mag. Mat. **310**, 1300 (2007). 10

[36] A. Yaouanc, P. Dalmas de Réotier, Y. Chapuis, C. Marin, G. Lapertot, A. Cervellino, and A. Amato, Phys. Rev. B. **77**, 092403 (2008). 10

[37] D. E. Maclaughlin, Y. Nambu, S. Nakatsuji, R. H. Heffner, L. Shu, O. O. Bernal, and K. Ishida, Phys. Rev. B **78**, 220403(R) (2008). 10

[38] H. Takeya, K. Ishida, K. Kitagawa, Y. Ihara, K. Onuma, Y. Maeno, Y. Nambu, S. Nakatsuji, D. E. Maclaughlin, A. Koda, and R. Kadono, Phys. Rev. B **77**, 054429 (2008). 10

[39] H. Yamaguchi, S. Kimura, M. Hagiwara, Y. Nambu, S. Nakatsuji, Y. Maeno, and K. Kindo, Phys. Rev. B **78**, 180404(R) (2008). 10

[40] H. Yamaguchi, S. Kimura, M. Hagiwara, Y. Nambu, S. Nakatsuji, Y. Maeno, A. Matsuo, and K. Kindo, J. Phys. Soc. Jpn. **79**, 054710 (2010). 10

[41] C. Stock, S. Jonas, C. Broholm, S. Nakatsuji, Y. Nambu, K. Onuma, Y. Maeno, and J.-H. Chung, Phys. Rev. Lett. **105**, 037402 (2010). 10

[42] Y. Nambu, R. T. Macaluso, T. Higo, K. Ishida, and S. Nakatsuji, Phys. Rev. B **79**, 214108 (2009). 10

[43] Y. Nambu and S. Nakatsuji, J. Phys.: Condens. Matter **23**, 164202 (2011). 10

[44] Y. Nambu, S. Nakatsuji, Y. Maeno, E. K. Okudzeto, and J. Y. Chan, Phys. Rev. Lett. **101**, 207204 (2008). 10

[45] H. Tsunetsugu and M. Arikawa, J. Phys.: Soc. Jpn. **75**, 083701 (2006). 10

[46] S. Bhattacharjee, V. B. Shenoy, and T. Senthil, Phys. Rev. B **74**, 092406 (2006). 10

[47] H. Kawamura and S. Miyashita, J. Phys. Soc. Jpn. **53**, 4138 (1984). 10

[48] H. Kawamura and A. Yamamoto, J. Phys. Soc. Jpn. **76**, 073704 (2007). 10

[49] P. Dalmas de Réotier, A. Yaouanc, Y. Chapuis, C. Marin, G. Lapertot, A. Cervellino, and A. Amato, J. Phys.: Conf. Ser. **145**, 012045 (2009). 10

[50] C.-H. Chern, Phys. Rev. B **78**, 020403(R) (2008). 10

[51] E. M. Stoudenmire, S. Trebst, and L. Balents, Phys. Rev. B **79**, 214436 (2009). 10

[52] D. A. Huse and V. Elser, Phys. Rev. Lett. **60**, 2531 (1988). 12

[53] B. Bernu, C. Lhuillier, and L. Pierre, Phys. Rev. Lett. **69**, 2590 (1992). 12

[54] P. Sindzingre, P. Lecheminant, and C. Lhuillier, Phys. Rev. B **50**, 3108 (1994). 12

[55] L. Capriotti, A. E. Trumper, and s. Sorella, Phys. Rev. Lett. **82**, 3899 (1999). 12

[56] G. Blasse, J. Inorg. Nucl. Chem. **27**, 993 (1965). 12

[57] S.Ya. Istomin, V.A. Koutcenko, E.V. Antipov, F. Lindberg, and G. Svensson, Mater. Res. Bull. **39**, 1013 (2004). 12

[58] Y. Doi, Y. Hinatsu, and K. Ohoyama, J. Phys.: Condens. Matt. **16**, 8923 (2004). 12

[59] Y. Shirata, H. Tanaka, A. Matsuo, and K. Kindo, Phys. Rev. Lett. **108**, 057205 (2012). 12

[60] H.D. Zhou, C. Xu, A.M. Hallas, H.J. Silverstein, C.R. Wiebe, I. Umegaki, J.Q. Yan, T.P. Murphy, J.-H. Park, Y. Qiu, J.R.D Copley, J.S. Gardner, and Y. Takano, Phys. Rev. Lett. **109**, 267206 (2012). 12

[61] T. Susuki, N. Kurita, T. Tanaka, H. Nojiri, A. Matsuo, K. Kondo, and H. Tanaka, Phys. Rev. Lett. **110**, 267201 (2013). 12

[62] G. Koutroulakis, T. Zhou, Y. Kamiya, J. D. Thompson, H. D. Zhou, C. D. Batista, and S. E. Brown, Phys. Rev. B **91**, 024410 (2015). 12

[63] G. Quirion, M. Lapointe-Major, M. Poirier, J. A. Quilliam, Z. L. Dun, and H. D. Zhou, Phys. Rev. B **92**, 014414 (2015). 12

[64] D. Yamamoto, G. Marmorini, and I. Danshita, Phys. Rev. Lett. **114**, 027201 (2015). 12

[65] E. A. Ghioldi, A. Mezio, L. O. Manuel, R. R. P. Singh, J. Oitmaa, and A. E. Trumper, Phys. Rev. B **91**, 134423 (2015). 12

[66] D. Yamamoto, G. Marmorini, and I. Danshita, J. Phys. Soc. Jpn. **85**, 024706 (2016). 12

[67] G. Marmorini, D. Yamamoto, and I. Danshita, Phys. Rev. B **93**, 224402 (2016). 12

[68] P. A. Maksimov, M. E. Zhitomirsky, and A. L. Chernyshev, Phys. Rev. B **94**, 140407(R) (2016). 12

[69] J. Ma, Y. Kamiya, Tao Hong, H.B. Cao, G. Ehlers, W. Tian, C.D. Batista, Z.L. Dun, H.D. Zhou, and M. Matsuda, Phys. Rev. Lett. **116**, 087201 (2016). 12

[70] S. Ito, N. Kurita, H. Tanaka, S. Ohira-Kawamura, K. Nakajima, S. Itoh, K. Kuwahara, and K. Kakurai, Nature Commun. **8**, 235 (2017). 12

[71] D. Khomskii, Physics **2**, 20 (2009). 13

[72] U. Treiber and S. Kemmler-Sack, J. Solid State Chem. **43**, 51 (1982). 13

[73] Y. Liu, R. L. Withers, A.P. Whichello, L. Norén, V. Ting, F. Brink, and J. D. Fitz Gerald, J. Sol. Stat. Chem. **178**, 3389 (2005). 13

[74] Y. Liu, R. L. Withers, V. Ting, J. D. Fitz Gerald, and L. Norén, Phys. B: Condens. Matter **385-386**, 564 (2006). 14

[75] Z. Tian, Q. Guo, Z. Ouyang, G. Du, W. Tong, J. Wang, and S. Yuan, Sol. State Comm. **191**, 66 (2014). 14

[76] M. Lee, E.S. Choi, X. Huang, J. Ma, C.R. dela Cruz, M. Matsuda, W. Tian, Z.L. Dun, S. Dong, and H.D. Zhou, Phys. Rev. B **90**, 224402 (2014). 14

[77] J. Hwang, E. -S. Choi, F. Ye, C. R. dela Cruz, Y. Xin, H. -D. Zhou, and P. Schlottmann, Phys. Rev. Lett. **109**, 257205 (2012). 14

[78] M. Lee, J. Hwang, E.S. Choi, J. Ma, C.R. dela Cruz, M. Zhu, X. Ke, Z.L. Dun, and H.D. Zhou, Phys. Rev. B **89**, 104420 (2014). 14

[79] J. Ma, V. O. Garlea, A. Rondinone, A. A. Aczel, S. Calder, C. dela Cruz, R. Sinclair, W. Tian, S. Chi, A. Kiswandhi, J. S. Brooks, H. D. Zhou, and M. Matsuda, Phys. Rev. B **89**, 134106 (2014). 18

[80] A. Samarakoon, T. J. Sato, T. Chen, G.-W. Chern, J. Yang, I. Kilch, R. Sinclair, H. D. Zhou, and S.-H. Lee, PNAS **42**, 11806 (2016). 18

[81] M. Lee, E. S. Choi, J. Ma, R. Sinclair, C. R. dela Cruz, and H. D. Zhou, J. Phys.: Condens. Matter **28**, 476004 (2016). 18

[82] M. Lee, E.S. Choi, J. Ma, R. Sinclair, C.R. dela Cruz, and H.D. Zhou, Mat. Res. Bull. **88**, 308 (2017). 18

[83] D. Ziat, A. A. Aczel, R. Sinclair, Q. Chen, H. D. Zhou, T. J. Williams, M. B. Stone, A. Verrier, and J. A. Quilliam, Phys. Rev. B **95**, 184424 (2017). 18

[84] A. M. Samarakoon, M. Takahashi, D. Zhang, J. Yang, N. Katayama, R. Sinclair, H. D. Zhou, S. O. Diallo, G. Ehlers, D. A. Tennant, S. Wakimoto, K. Yamada, G.-W. Chern, T. J. Sato, and S.-H. Lee, Sci. Rep. **7**, 12053 (2017). 18

[85] R. Yu, S. Banerjee, H. C. Lei, R. Sinclair, M. Abeykoon, H. D. Zhou, C. Petrovic, Z. Guguchia, and E. S. Bozin, Absence of Local Fluctuating Dimers in Superconducting $Ir_{1-x}(Pt,Rh)_xTe_2$, arXiv:1801.0050v1 (2017). 18

[86] E. D. Mun, G.-W. Chern, V. Pardo, F. Rivadulla, R. Sinclair, H. D. Zhou, V. S. Zapf, and C. D. Batista, Phys. Rev. Lett. **112**, 017207 (2014). 18

[87] R. Sinclair, J. Ma, H. B. Cao, T. Hong, M. Matsuda, Z. L. Dun, and H. D. Zhou, Phys. Rev. B **92**, 134410 (2015). 18

[88] R. Sinclair, H. B. Cao, V. O. Garlea, M. Lee, E. S. Choi, Z. L. Dun, S. Dong, E. Dagotto, and H. D. Zhou, J. Phys.: Condens. Matter **29**, 065802 (2017). 18

[89] J. Feng, A. Juhin, R. Delaunay, R. Jarrier, N. Jaouen, A. Nicolaou, R. Sinclair, H. D. Zhou, J.-M. Mariot, and S. G. Chiuzbaian, J. of Appl. Phys. **122**, 194101 (2017). 18

[90] D. Bansal, J. L. Niedziela, R. Sinclair, V. O. Garlea, D. L. Abernathy, S. Chi, Y. Ren, H. D. Zhou, and O. Delaire, Nature Comm. **9**, 15 (2018). 18

[91] J. Rodriguez-Carvajal, Phys. B (Amsterdam, Neth.) **192**, 55 (1993). 18

[92] S. J. Blundell and K. M. Blundell, *Concepts in thermal physics*, Oxford [etc.]: Oxford University Press (2016). 19

[93] Z.L. Dun, X. Li, R. S. Freitas, E. Arrighi, C. R. dela Cruz, M. Lee, E. S. Choi, H. B. Cao, H. J. Silverstein, C. R. Wiebe, J. G. Cheng, and H. D. Zhou, Phys. Rev. B **92**, 140407(R) (2015). 23

[94] L. W. Finger, D. E. Cox, and A. P. Jephcoat, J. Appl. Cryst. **27**, 892 (1994). 29

[95] A. S. Wills, Physica B: Condens. Matter (Amsterdam, Neth.) **276-278**, 680 (2000). 29

[96] S. Toth and B. Lake, J. Phys.: Condens. Matter **27**, 166002 (2015). 30

[97] D. I. Khomskii, J. of Mag. and Mag. Mat. **306**, 1 (2006). 31

[98] W. Eerenstein, N. D. Mathur, and J. F. Scott, Nature (London) **442**, 17 (2006).

[99] S. -W. Cheong and M. Mostovoy, Nat. Mater. **6**, 13 (2007). 31

[100] J. Hwang, E. S. Choi, H. D. Zhou, Y. Xin, J. Lu, and P. Schlottmann, Phys. Rev. B **85**, 224429 (2012). 31

[101] S. Oyama, M. Wakeshima, Y. Hinatsu, and K. Ohoyama, J. Phys.:Condens. Matter **16**, 1823 (2004). 31

[102] J. Hwang, E. S. Choi, H. D. Zhou, J. Lu, and P. Schlottmann, Phys. Rev. B. **85**, 024415 (2012). 31

[103] M. Greenblatt, R.M. Hornreich, and B. Sharon, J. Sol. Stat. Chem. **10**, 371 (1974). 31

[104] J. Saha, G. Sharma, S. Patnaik, J. of Mag. and Mag. Mat. **360**, 34 (2014). 32

[105] H. M. Kriz and P. J. Bray, J. Chem. Phys. **51**, 3624 (1969). 32

[106] J. H. Dennings and S. D. Ross, Spectrochim. Acta Sect. A **28**, 1775 (1972). 32

[107] D. Boyer, G. Bertrand-Chadeyron, R. Mahiou, C. Caperaa, and J.-C. Cousseins, J. Mater. Chem. **9**, 211 (1999). 32

[108] Z. Wei, L. Sun, C. Liao, J. Yin, X. Jiang, and C. Yan, J. Phys. Chem. B **106**, 10610 (2002). 32

[109] J. Liu, D. Sheptyakov, Y. Wang, and P. Allenspach, Chem. Mater. **16**, 2418 (2004). 32

[110] J. Zhang and J. Lin, J. Cryst. Growth **271**, 207 (2004). 32

[111] L. Li, S. Zhou, and S. Zhang, Sol. Stat. Sci. **10**, 1173 (2008). 32

[112] R. E. Newnham, M. J. Redman, and R. P. Santoro, J. Amer. Cer. Soc. **46**, 253 (1963). 32

[113] W. F. Bradley, D. L. Graf, and R. S. Roth, Acta. Cryst. **20**, 283 (1966). 32

[114] G. Chadeyron, M. El-Ghozzi, R. Mahiou, A. Arbus, and J. C. Cousseins, J. Sol. Stat. Chem. **128**, 261 (1997). 32

[115] N. C. Tombs, W. J. Croft, and H. C. Mattraw, Inorg. Chem. **2**, 872 (1963). 32

[116] T.A. Bither, C.G. Frederick, T.E. Gier, J.F. Weiher, and H.S. Young, Sol. Stat. Comm. **8**, 109 (1970). 32

[117] A. D. Balaev, N. B. Ivanova, N. V. Kazak, S. G. Ovchinnikov, V. V. Rudenko, and V. M. Sosnin, Phys. Sol. Stat. **45**, 287 (2003). 32

[118] Ö. F. Öztürk, B. Zümreoglu-Karan, M. M. Can, and S. Ozcan, Z. Anorg. Allg. Chem. **634**, 1127 (2008). 32

[119] Y. Laureiro, M. L. Veiga, F. Fernandez, R. Saez Puche, A. Jerez, and C. Pico, J. Less-Common Met. **157**, 335 (1990). 32

[120] P. Mukherjee, Y. Wu, G.I. Lampronti, and S.E. Dutton, Mat. Res. Bull. **98**, 173 (2018). 32

[121] Y. Doi, T. Satou, and Y. Hinatsu, J. Sol. Stat. Chem. **206**, 151 (2013). 32

[122] R. Sinclair, H. D. Zhou, M. Lee, E. S. Choi, G. Li, T. Hong, and S. Calder, Phys. Rev. B **95**, 174410 (2017). 32, 33, 34, 35, 47

[123] S. Toth and B. Lake, J. Phys.: Condens. Matter **27**, 166002 (2015). 33

[124] M. I. Aroyo, J. M. Perez-Mato, D. Orobengoa, E. Tasci, G. de la Flor, and A. Kirov, Bulg. Chem. Commun. **43(2)**, 183 (2011). 43

[125] M. I. Aroyo, J. M. Perez-Mato, C. Capillas, E. Kroumova, S. Ivantchev, G. Madariaga, A. Kirov, and H. Wondratschek, Z. Krist. **221**, 15 (2006). 56

[126] M. I. Aroyo, A. Kirov, C. Capillas, J. M. Perez-Mato, and H. Wondratschek, Acta Cryst. **A62**, 115 (2006). 56

[127] J.M. Perez-Mato, S.V. Gallego, E.S. Tasci, L. Elcoro, G. de la Flor, and M.I. Aroyo, Annu. Rev. Mater. Res. **45**, 13.1-13.32 (2015). 56

[128] J. Kanamori, J. Phys. Chem. Solids **10**, 87 (1959). 56

[129] K. Yokota, N. Kurita, and H. Tanaka, Phys. Rev. B **90**, 014403 (2014). 57

[130] A. Möller, N. E. Amuneke, P. Daniel, B. Lorenz, C.R. dela Cruz, M. Gooch, and P.C.W. Chu, Phys. Rev. B **85**, 214422 (2012). 57

[131] T. Katsufuji and H. Takagi, Phys. Rev. B **64**, 054415 (2001). 57

[132] V. V. Shvartsman, P. Borisov, W. Kleemann, S. Kamba, and T. Katsufuji, Phys. Rev. B. **81**, 064426 (2010). 59

[133] R. Tackett, G. Lawes, B. C. Melot, M. Grossman, E. S. Toberer, and R. Seshadri, Phys. Rev. B **76**, 024409 (2007). 59

[134] G. Lawes, T. Kimura, C.M. Varma, M.A. Subramanian, N. Rogado, R.J. Cava, and A.P. Ramirez, Prog. solid State Chem. **37**, 40 (2009). 59

[135] G. Nénert, U. Adem, E. M. Bauer, C. Bellitto, G. Righini, and T. T. M. Palstra, Phys. Rev. B **78**, 054443 (2008). 59

[136] G. Nénert, H.-J. Koo, C. V. Colin, E. M. Bauer, C. Bellitto, C. Ritter, G. Righini, and M.-H. Whangbo, Inorg. Chem. **52**, 753 (2013). 59
59

[137] R. Pocha and D. Johrendt, Chem. Mater. **12**, 2882 (2000). 62

[138] E. V. Anokhina, C. S. Day, and A. Lachgar, Inorg. Chem. **40**, 5072 (2001). 62

[139] M. M. Abd-Elmeguid, B. Ni, D. I. Khomskii, R. Pocha, D. Johrendt, X. Wang, and K. Syassen, Phys. Rev. Lett. **93**, 126403 (2004). 62

[140] H. Nakamura, H. Chudo, and M. Shiga, J. Phys.: Condens. Matter **17**, 6015 (2005). 62

[141] Y. Haraguchi, C. Michioka, H. Ueda, and K. Yoshimura, Phys. Rev. B **90**, 064403 (2014). 62

[142] J. P. Sheckelton, J. R. Neilson, D. G. Soltan, and T. M. McQueen, Nat. Mater. **11**, 493 (2012). 62, 64, 87

[143] J. P. Sheckelton, J. R. Neilson, and T. M. McQueen, Mater. Horiz. **2**, 76 (2015). 62, 64

[144] J. P. Sheckelton, K. W. Plumb, B. A. Trump, C. L. Broholm, and T. M. McQueen, Inorg. Chem. Front. **4**, 481 (2017). 62, 64

[145] R. Flint and P. A. Lee, Phys. Rev. Lett. **111** 217201 (2013). 64, 87

[146] M. Mourigal, W. T. Fuhrman, J. P. Sheckelton, A. Wartelle, J. A. Rodriguez-Rivera, D. L. Abernathy, T. M. McQueen, and C. L. Broholm, Phys. Rev. Lett. **112**, 027202 (2014). 64

[147] J. P. Sheckelton, F. R. Foronda, L.D. Pan, C. Moir, R. D. McDonald, T. Lancaster, P. J. Baker, N. P. Armitage, T. Imai, S. J. Blundell, and T. M. McQueen, Phys. Rev. B **89**, 064407 (2014). 64, 87

[148] G. Chen, H.-Y. Kee, and Y. B. Kim, arXiv:1408.1963v2 (2014). 64, 72, 87

[149] L. Clark, J. C. Orain, F. Bert, M. A. De Vries, F. H. Aidoudi, R. E. Morris, P. Lightfoor, J. S. Lord, M. T. F. Telling, P. Bonville, J. P. Attfield, P. Mendels, and A. Harrison, Phys. Rev. Lett. **110**, 207208 (2013). 64

[150] R. Schaffer, Y. Huh, K. Hwang, and Y. B. Kim, Phys. Rev. B **95** 054410 (2017). 64

[151] J.-C. Orain, B. Bernu, P. Mendels, L. Clark, F. H. Aidoudi, P. Lightfoot, R. E. Morris, and F. Bert, Phys. Rev. Lett. **118** 237203 (2017). 64

[152] P. Gall, R. A. R. A. Orabi, T. Guizouarn, and P. Gougeon, J. Solid State Chem. **208**, 99 (2013). 64

[153] Y. Haraguchi, C. Michioka, M. Imai, H. Ueda, and K. Yoshimura, Phys. Rev. B **92**, 014409 (2015). 64

[154] C. C. Torardi and R. E. McCarley, Inorg. Chem. **24**, 476 (1985). 64, 79

[155] A. Akbari-Sharbaf1, R. Sinclair, A. Verrier, D. Ziat, H. D. Zhou, X. F. Sun, and J. A. Quilliam, arXiv:1709.01904v2 (2017). 65, 72, 75, 88

[156] G. Chen, H.-Y. Kee, and Y. B. Kim, Phys. Rev. B **93**, 245134 (2016). 69, 72, 87

[157] P. W. Anderson, G. Baskaran, Z. Zou, and T. Hsu, Phys. Rev. Lett. **58**, 2790 (1987). 72

[158] S. Yamashita, Y. Nakazawa, M. Oguni, Y. Oshima, H. Nojiri, Y. Shimizu, K. Miyagawa, and K. Kanoda, Nature Physics **4**, 459 (2008). 72

[159] S. Yamashita, T. Yamamoto, Y. Nakazawa, M. Tamura, and R. Kato, Nature Comm. **10**, 1038 (2011). 72

[160] C. P. Slichter, *Principles of Magnetic Resonance, Third Enlarged and Updated Edition* (Springer, 1989). 75

[161] P. Mendels, F. Bert, M. A. de Vries, A. Olariu, A. Harrison, F. Duc, J. C. Trombe, J. S. Lord, A. Amato, and C. Baines, Phys. Rev. Lett. **98**, 077204 (2007). 75

[162] E. Kermarrec. P. Mendels, F. Bert, R. H. Colman, A. S. Wills, P. Strobel, P. Bonville, A. Hillier, and A. Amato, Phys. Rev. B **84**, 100401(R) (2011). 75

[163] J. A. Quilliam, F. Bert, E. Kermarrec, C. Payen, C. Guillot-Deudon, P. Bonville, C. Baines, H. Luetkens, and P. Mendels, Phys. Rev. Lett. **109**, 117203 (2012). 75

[164] J. A. Quilliam, F. Bert, A. Manseau, C. Darie, C. Guillot-Deudon, C. Payen, C. Baines, A. Amato, and P. Mendels, Phys. Rev. B **93**, 214432 (2016). 75

[165] N. F. Mott, Philosophical Magazine **19:160**, 835 (1969). 86

[166] M. Mostefa, S. Boutiche, and M. Khodja, Sol. State Comm. **82**, 697 (1992). 86

[167] M. B. Hastings, Phys. Rev. B **69**, 104431 (2004). 87

[168] O. I. Motrunich, Phys. Rev. B **73**, 155115 (2006). 87

Vita

Ryan Sinclair was born on April 18th, 1991, in Terre Haute, Indiana. After high-school, he joined the physics department at the University of Tennessee in 2009 and received a B.S. in physics and mathematics in 2013. Afterwards, he chose to stay at the University of Tennessee to purse a Ph.D in condensed matter physics. He officially joined the group of Dr. Haidong Zhou in 2014 and worked four years as a research assistant before receiving his Ph.D in 2018.